Simplified fabrication of complex multilayer microfluidics: enabling sophisticated Lab-on-a-chip and point-of-care platforms

A thesis submitted in fulfilment of the requirements for the degree of Doctor of Philosophy

Crispin Szydzik

B. Eng (Electronic communications engineering), RMIT University

School of Engineering

College of Science Engineering and Health

RMIT University

October 2018

Declaration

I certify that except where due acknowledgement has been made, the work is that of the author alone; the work has not been submitted previously, in whole or in part, to qualify for any other academic award; the content of the thesis is the result of work which has been carried out since the official commencement date of the approved research program; any editorial work, paid or unpaid, carried out by a third party is acknowledged; and, ethics procedures and guidelines have been followed.

Crispin Szydzik

October 2018

Acknowledgements

Abstract

Complex multilayer microfluidics have generated a lot of interest in recent years. Early research introduced elastomer microvalves and postulated they would bring about a revolution for microfluidic systems, similar in scale to introduction of the transistor for electronic systems. In the following years, many researchers have been active in the use of complex multilayer microfluidic systems, with numerous high impact research outcomes using these systems as precise and active control components, providing fluidic isolation, switching or fluidic actuation, and allowing unprecedented sophistication and precise control and automation of experimental conditions. While application of complex multilayer microfluidic platforms has been demonstrated in numerous research settings, there is little evidence that the technology has become ubiquitously accepted, with a lack of evidence for point-of-care application, or widespread acceptance within the research community. While the advantages that the technology offers have been well documented, the field seems to have failed to gain traction, or facilitate the revolution that was predicted on its introduction.

There are various possible explanations for this lack of acceptance, as with any technology, there are caveats to the application of complex multilayer microfluidic systems, however given the broad range of demonstrated applications, it is unlikely that the bottleneck in their application is related to a fundamental application related limitation. In contrast, fabrication technology utilised in realisation of complex multilayer microfluidic systems, has not advanced at the same rate to the multitude of application-based publications in the past decade.

This thesis explores the hypothesis that one of the fundamental limiting factors in widespread application of complex multilayer microfluidic systems, is related to the challenges associated with fabrication of these systems. To explore this hypothesis, firstly, a new fabrication approach is introduced which aims to eliminate many of the challenges associated with traditional multilayer fabrication methods, this technique is demonstrated in a proof of concept capacity, fabricating common multilayer microfluidic structures and doing so with surprising ease.

Having developed method with simpler fabrication, it is possible to explore whether overcoming the multilayer fabrication bottleneck would allow the advantages inherent to complex multilayer microfluidic systems to be applied to fields which would otherwise be considered prohibitively

i

difficult, if reliant on traditional fabrication methods. This hypothesis is investigated through harnessing the new, simplified fabrication technique to advance point-of-care photonic biosensor research through short term collaborative engagements. It is found that the use of modular building blocks and the simple, rapid fabrication enables sophisticated microfluidic chip prototypes to be developed in a very short period of time achieving multiple iterations over a matter of weeks and even facilitating collaboration on these integrated platforms remotely. The outcomes of these short-term collaborations have produced publications automating the fluid handling of highly sensitive interferometric waveguide biosensors and environmental control for a single cell analysis platform utilising integrated plasmonic biosensors.

Having demonstrated that simplifying complex microfluidic fabrication can accelerate the development and deployment of these systems to enhance research platforms, the next step was to explore whether this simplified system could also lower the barrier to deployment in a clinical setting. The ability for the fluidic system to handle whole blood was chosen as a deliberately challenging target with great sensitivity to fluid dynamics and large variability in patient samples and environmental factors, requiring large number of replicate devices to determine statistical significance. Here the fabrication technique is applied to enable a study investigating the hemocompatibility of common multilayer control components, paving the way for point of care blood handling devices. It is shown that not only can the technique be used to rapidly develop platforms that can be used with blood, but the same technique can produce even hundreds of replicates required for limited clinical trials, leading the collaborating clinicians to seriously consider these complex microfluidics for future point of care diagnostics.

In Summary, it has been demonstrated that access to complex multilayer microfluidic systems without the fabrication overheads generally associated with these systems can allow their application to areas that would otherwise be prohibitively difficult. The fabrication method presented can allow rapid development, and rapid and reliable deployment to various research applications, while allowing the consistency and throughput required enabling large volume fabrication required for clinical investigations. The fact that such a large advancement toward real world application within the scope of a single PhD is possible, supports the hypothesis that lowering the barrier to fabricating complex microfluidic devices has the potential to significantly increase their scope of application.

ii

Table of Contents

CHAPTER 1: Introduction

As a facilitating multidisciplinary technology, the field of microfluidics generates impact across a broad range of fields [1-3] with diverse applications ranging from micro-propulsion systems for spacecraft [4], chemical synthesis [5] environmental monitoring [6] and food safety applications [7]. Perhaps most notably, microfluidic technologies have had significant impact within the biomedical field in recent years [8]. While complex multilayer microfluidic systems have been evident in the literature for decades [9], the accessibility, low cost, and relative ease of fabrication introduced with elastomer based complex multilayer systems, has seen the field flourish [10]. in following years, complex multilayer microfluidic lab-on-a-chip applications have achieved extraordinary levels of sophistication [11-13]. Microfluidic logic circuitry, developed to mirror the functionality offered by digital logic [14-17], has demonstrated the potential for new levels of reconfigurable automation for lab on a chip devices. Programmable fluidic processors have been coupled with biosensors, working toward point of care diagnostics [18-20], and 3-Dimensional multilayer organ-on-a-chip research platforms have been developed reproducing in-vivo conditions with unprecedented accuracy [21].

Introduction of elastomer microvalves valve nearly two decades ago, brought with it the promise of breakthroughs for multilayer microfluidic lab-on-a-chip application. Elastomer microvalve enabled systems were heralded as a catalyst to microfluidics, as the integrated circuit was to the electronics industry. Enabling more complex and precise automated biochemical systems, the potential for nearly arbitrary scalability of on chip complexity, promised a revolution like that seen in information processing brought by complex electronic integration [22].

In following years, multilayer microfluidic systems have advanced and broadened in application, with success marked by numerous high impact research outcomes. Some success has been seen toward the goal of arbitrarily complex and reconfigurable microfluidic systems[19, 23], however these advances have generally not seen translation to point of care application, nor have they become a widely accepted mainstay within research applications, despite the numerous advantages they offer over simpler systems [11].

1

It is not immediately apparent why complex multilayer microfluidic systems have not gained more traction. One potential factor is the 'chip-in-a-lab' conundrum [24], this refers to the problem that a large number of on-chip control elements generally require similarly large numbers of external control systems, and that the cost and complexity of external support equipment tends to scale along with on-chip complexity. Various solutions to this problem have been proposed, including reducing the number of necessary control lines using parallelisation [25], simple fluid rout multiplexing systems [22], or more complex microfluidic logic based multiplexer solutions [11]. While solutions to this problem have been proposed, little evidence suggests their potential has been fully realised, with a lack of development toward widespread acceptance or point of care application within complex multilayer microfluidic systems.

Other potential issues that may stand in the way of widespread acceptance of complex multilayer microfluidic systems could be related to device variability and operational robustness. Alignment of multiple thin PDMS layers can pose a significant challenge [26], while bonding of these layers can be difficult [27], leading to imperfections or defects, impacting reliability. Alignment is particularly important in the case of encapsulation of components of different materials, as commonly used in cell culture systems that make use of integrated commercial membranes [28] and it is exactly these complex biological systems that require large numbers of identical and reliable replicates.

Perhaps the most plausible bottleneck for widespread acceptance of complex multilayer microfluidic systems, are challenges associated with fabrication of these devices. There are numerous examples in the literature of application of these systems, including solutions to some of the practical issues inherent to their application, but they are generally limited to high value research platforms. The fact that it is difficult to scale existing fabrication methods, makes them unsuited to the mass fabrication that would be required for commercial applications, as would be required for point of care implementation

This thesis will explore the hypothesis that one of the fundamental limiting factors in widespread application of complex multilayer microfluidic systems, is related to the challenges associated with fabrication of these systems.

Chapter 2 postulates that it is possible to develop a fabrication method minimising the overheads generally associated with fabrication of these devices. This is motivated by the hypothesis of this thesis that such a simplified fabrication approach would allow the application of complex microfluidics to real world problems, allowing application in areas that would be prohibitively difficult to engage when reliant on traditional fabrication methods. This chapter introduces a fabrication method that mitigates several major challenges associated with multilayer microfluidic fabrication, allowing scaling of on chip complexity without significant impact on fabrication complexity. The fabrication method is validated in a proof of concept capacity, through application to two common representative fabrication challenges. These applications demonstrate the techniques capacity to fabricate a range of different multilayer structures, and handle both simple fluids in the form of a droplet generation system, and more complex biological sample fluids, in the context of a cell culture platform.

The level of interest in complex multilayer microfluidic systems over the last decade has resulted in a large reservoir of knowledge surrounding multilayer microfluidic components and subsystems. Numerous applications of multilayer microfluidic systems have been validated and characterised in various settings, with design considerations and detailed performance data available on fluidic automation, precise fluid manipulation and environmental control systems.

Chapter 3 of this thesis investigates the hypothesis that given a simplified fabrication method, it should be possible to utilise the reservoir of available literature as plug-and-play adaptable modular subsystems. With a sufficiently simplified fabrication method, it should be possible to rapidly develop solutions to various real-world problems, with short fabrication turnarounds allowing iterative improvements, building on well characterised components that have been demonstrated in the literature. In short, it should be possible to engage in short term collaborations with end-users unfamiliar with the field, and rapidly develop solutions to their research problems through deployment of the numerous advantages inherent to complex multilayer microfluidic systems, in a manner not previously practical with traditional fabrication methods. As an additional benefit, working with researchers in complementary fields, in deployment of this technology, should allow additional insight into other factors that may be holding back widespread acceptance of complex multilayer microfluidic systems. This chapter

investigates the practicalities of the fabrication technique outlined in chapter 2, when applied to real world photonic biosensor applications, specifically in the context of a point-of-care application, and a sophisticated lab on a chip research platform, and was carried out in collaboration with researchers in leading groups working with these devices.

Finally, in chapter 4, the simplified fabrication technique is applied to clinical biological studies demanding complex sample fluid handling and requiring large numbers of uniform replicates. Manipulation of blood within artificial microsystems is challenging due to its complex and reactive nature, generally rendering re-use of devices impractical. Residues from previous samples can contaminate subsequent assays, and for this reason, large numbers of consistent replicate devices are generally required for blood-based research applications. Due to the single requirements and large number of required replicate devices, application of complex multilayer fluidic systems to blood handling is challenging when restricted to traditional fabrication methods. This chapter assesses the scalability of the fabrication technique outlined in chapter 2, investigating the practicality of fabricating the large quantities of single use disposable devices required for replicate bioassays. This work facilitates the implementation of a biological study, investigating the hemocompatibility of common on-chip control components, lifting gate pneumatic microvalves, paving the way for point of care blood handling devices. This work demonstrates that biological research applications utilising complex multilayer microfluidic structures are practically possible, given removal of their usual fabrication overheads.

The aim of this thesis is work toward facilitating realisation of the full potential complex multilayer microfluidic systems have been predicted to achieve. To this end, this thesis investigates a fabrication method intended to facilitate practical realisation of complex multilayer microfluidic structures. Application of this fabrication method is explored in the context of real-world problems, assessing the practicality, adaptability and scalability of the method. Finally, the method is used to fabricate complex multilayer microfluidic systems in volumes required to enable biological studies, facilitating insights into the use of common multilayer control components for handling complex biological samples. This thesis demonstrates that overcoming the fabrication overheads generally associated with complex multilayer microfluidics does significantly improve accessibility to the advantages they offer. It is possible that removal of the fabrication roadblock,

4

and the associated increase in accessibility will enable more widespread acceptance of complex multilayer microfluidics. however, insights gained in the course of this work have identified other potential factors limiting complex multilayer microfluidics from reaching their full potential, with future work suggesting possible avenues towards their resolution

1.1 Research outputs

Below is a list of the authors scientific contributions during this candidature. Not all research outputs are covered by the scope of this thesis. Publications relevant to this thesis are numbered and appear in the order of appearance in the thesis, as listed below.

1. Szydzik, C., Niego, B., Dalzell, G., Knoerzer, M., Ball, F., Nesbitt, W.S., Medcalf, R.L., Khoshmanesh, K. and Mitchell, A., 2016. Fabrication of complex PDMS microfluidic structures and embedded functional substrates by one-step injection moulding. *RSC Advances*, *6*(91), pp.87988-87994.
   [29] Impact factor: 2.936

2. Szydzik, C., Gavela, A.F., Herranz, S., Roccisano, J., Knoerzer, M., Thurgood, P., Khoshmanesh, K., Mitchell, A. and Lechuga, L.M., 2017. An automated optofluidic biosensor platform combining interferometric sensors and injection moulded microfluidics. *Lab on a Chip*, *17*(16), pp.2793-2804.
   [30] Impact factor: 5.995

3. Li, X., Soler, M., Szydzik, C., Khoshmanesh, K., Schmidt, J., Coukos, G., Mitchell, A. and Altug, H., 2018. Label-Free Optofluidic Nanobiosensor Enables Real-Time Analysis of Single-Cell Cytokine Secretion. *Small*, p.1800698.
   [31] Impact factor: 9.598

4. Szydzik, C., Brazilek, R.J., Khoshmanesh, K., Akbaridoust, F., Knoerzer, M., Thurgood, P., Muir, I., Marusic, I., Nandurkar, H., Mitchell, A. and Nesbitt, W.S., 2018. Elastomeric microvalve geometry affects haemocompatibility. *Lab on a Chip*, *18*(12), pp.1778-1792.
   [32] Impact factor: 5.995

- Szydzik, C., Khoshmanesh, K., Mitchell, A. and Karnutsch, C., 2015. Microfluidic platform for separation and extraction of plasma from whole blood using dielectrophoresis. *Biomicrofluidics*, *9*(6), p.064120.

  [33] Impact factor: 2.571

- Thurgood, P., Baratchi, S., Szydzik, C., Mitchell, A. and Khoshmanesh, K., 2017. Porous PDMS structures for the storage and release of aqueous solutions into fluidic environments. *Lab on a Chip*, *17*(14), pp.2517-2527.

  [34] Impact factor: 5.995

- Knoerzer, M., Szydzik, C., Tovar-Lopez, F.J., Tang, X., Mitchell, A. and Khoshmanesh, K., 2016. Dynamic drag force based on iterative density mapping: A new numerical tool for three-dimensional analysis of particle trajectories in a dielectrophoretic system. *Electrophoresis*, *37*(4), pp.645-657.

  [35] Impact factor: 2.569 (Co-1st author)

- Thurgood, P., Baratchi, S., Szydzik, C., Zhu, J.Y., Nahavandi, S., Mitchell, A. and Khoshmanesh, K., 2018. A self-sufficient micro-droplet generation system using highly porous elastomeric sponges: A versatile tool for conducting cellular assays. *Sensors and Actuators B: Chemical*, *274*, pp.645-653.

  [36] Impact factor: 5.667

- Szydzik, C., Gavela, A.F., Roccisano, J., de Andrés, S.H., Mitchell, A. and Lechuga, L.M., 2016, December. Towards an integrated optofluidic system for highly sensitive detection of antibiotics in seawater incorporating bimodal waveguide photonic biosensors and complex, active microfluidics. In *SPIE BioPhotonics Australasia* (Vol. 10013, p. 100132C). International Society for Optics and Photonics.

  [37] (Conference paper)

CHAPTER 2: Fabrication of complex PDMS microfluidic structures and embedded functional substrates by one-step injection moulding

Chapter 1 identified the various advantages associated with complex multilayer microfluidic structures, but identified that the full potential predicted for complex multilayer microfluidics has yet to be realised, with little evidence of their widespread application outside niche lab environments. The hypothesis being pursued in this thesis is that a major barrier to widespread uptake and advancement of complex multilayer microfluidic systems is that the techniques required in their fabrication tend to be complex, labour intensive and generally don't scale well. While numerous advances have been made in application of multilayer complex microfluidics systems in recent years, the fabrication techniques employed in realisation of these systems have not advanced along with their application. Multilayer device fabrication often requires specialised and somewhat limiting mould fabrication techniques [40], alignment and bonding of multiple layers [40, 41], or sacrificial structures that require mould removal [42]. In addition, challenges associated with fabrication of these devices sometimes scale along with device complexity, as effects such as thermal expansion and alignment of multiple layers of soft elastomer scale with both overall device, and minimum feature size [26]. Due to the difficulty inherent to these kinds of fabrication techniques, complex multi-layer microfluidic systems are generally limited to applications suited to low-volume production, such as high-investment research platforms, or re-usable devices.

This chapter investigates whether it is possible to develop a technique which can utilise the advantages of multilayer complex microfluidic devices, while minimising the negative aspects associated with fabrication of these systems. In this chapter, I introduce a fabrication process that allows simplified fabrication of microfluidic structures containing complex multilayer geometry. This work is intended to allow integration of complex control components, such as pneumatic microvalves, as well as allowing integration of functional components, such as permeable membranes and electrochemical sensors used in cell culture platforms.

The majority of this chapter is in the form of a published journal article, which outlines a fabrication method that can achieve these requirements, allowing fabrication of complex multilayer microfluidic structures using a simple and robust fabrication process. This method is validated in a proof of concept capacity with fabrication of normally closed lifting gate pneumatic microvalves for metered flow control, as well as a 3D cell culture platform, culturing two distinct cell types on either side of an integrated permeable membrane. Moulds used in this work are fabricated using standard photolithographic processes, or stereolithography based 3D-pinting techniques. Alignment structures can be included in the design, reducing the fabrication complexity to a single step for valve-based designs, or a two-step process if integration of functional components is required.

The outcome of this work highlights that fabrication of complex multilayer microfluidics can be greatly simplified, overcoming numerous challenges associated with traditional methods used to fabricate microvalves [43], or multilayer membrane structures [28]. A fabrication method is outlined, allowing rapid and reliable fabrication of common complex multilayer microfluidic structures, and demonstrating this in a proof of concept capacity.

It is anticipated the level of simplification offered by this fabrication method will allow routine fabrication of complex multilayer microfluidic structures, allowing their application, and thus the advantages that they allow, to be applied to numerous applications that would otherwise be impractical when dependant on traditional fabrication techniques.

The proof of concept applications demonstrated in this chapter only contain a subset of complex multilayer components that may be required. Coming chapters will explore the practicality of this fabrication technique when applied to real world problems, investigating integration of more complex fluidic control components, active biosensor devices, and processing of complex biological samples, validating the benefits of the technique. In addition, the scalability of the fabrication technique will be explored, validating practicality of fabricating large quantities of replicate devices, as required for meaningful biological experiments.

As further work beyond the scope of this doctorate, I would suggest further exploration of the scalability of this fabrication technique in the context of commercial injection moulding approaches. Additionally, as PDMS is often not considered a favourable material for commercial application [44], There are various injection mouldable elastomer materials [45] that may be suited to fabrication with using method, allowing the mass production capacity that is required to realise practical point-of-care commercial application.

This work was the result of a collaborative project with the Australian centre for blood diseases in Melbourne, the work related to this chapter has been peer-reviewed and published in: ***RSC Advances***

The paper can be obtained via the DOI: 10.1039/C6RA20688C [29]

My role in this work was to conceptualise, design and iteratively improve the fabrication technique, fabricate microfluidic systems, run characterisation and cell culture experiments, and write the manuscript. Others assisted with manufacture of the support equipment, assisted with experimental design, and directed the biology. My leading role in this research is reflected in my being listed as first author.

Fabrication of complex PDMS microfluidic structures and embedded functional substrates by one-step injection moulding†

C. Szydzik,[a] B. Niego,[b] G. Dalzell,[a] M. Knoerzer,[a] F. Ball,[ac] W. S. Nesbitt,[ab] R. L. Medcalf,[b] K. Khoshmanesh[a] and A. Mitchell*[a]

We report a novel injection moulding technique for fabrication of complex multi-layer microfluidic structures, allowing one-step robust integration of functional components with microfluidic channels, and fabrication of elastomeric microfluidic valves. This technique simplifies multi-layer microfluidic device fabrication, while significantly increasing device functionality. We demonstrate functional component integration through robust encapsulation of porous polyester membranes, in the context of an *in vitro* research platform intended to facilitate Blood Brain Barrier (BBB) research. We also demonstrate the fabrication of normally-closed, pneumatically actuated elastomer valves, integrated using the same one-step process. These valves are demonstrated in the context of variable flow resistors used to modulate flow in a pressure driven system.

Introduction

Microfluidics has flourished in recent years as an emerging technology for addressing a wide range of research applications.[1–5] Perhaps most notably, microfluidics has shown significant promise in revolutionising the biomedical field.[6–9] Hybrid microfluidic devices have been reported incorporating integrated structures such as electrode arrays,[10] permeable membranes,[11] micro-valves[12,13] and other functional structures, enabling complex lab-on-a-chip research platforms and point-of-care devices. Numerous microfabrication techniques have been reported for the realisation of microfluidic devices. These commonly use the material polydimethylsiloxane (PDMS) due to its favourable chemical, mechanical, and optical properties, as well as its inherent biocompatibility.[4,14,15]

Methods for effective and reliable fabrication of complex multi-layer PDMS microfluidic structures incorporating functional structures such as valves, pumps, mixers, membranes and electrodes are crucial for further development of point-of-care and lab-on-a-chip devices. One key challenge is to achieve multiple microfluidic channels on different vertical planes as well as vertical interfaces between those channels without prohibitive fabrication complexity.

[a]School of Engineering, RMIT University, Melbourne, VIC 3001, Australia. E-mail: arnan.mitchell@rmit.edu.au

[b]Australian Centre for Blood Diseases, Monash University, Melbourne, Australia

[c]Institute for Optofluidics and Nanophotonics (IONAS), University of Applied Sciences Karlsruhe, Karlsruhe 76133, Germany

† Electronic supplementary information (ESI) available. See DOI: 10.1039/c6ra20688c

Reported fabrication techniques for realising such complex structures can be divided into three primary categories. The first category relies on sequential traditional 2D microfabrication to achieve multi-layer systems.[14,16–19] This approach has been the mainstay for realisation of complex microfluidics for over a decade, however while the devices have steadily increased in complexity, this fabrication technique has not evolved significantly in the passing years.[4,11,13,20,21] While layering of 2D microfabricated structures is appealing due to its maturity, complex systems often require multiple manual alignment and bonding processes, which require great skill, making them unsuitable for high volume fabrication.

The second category of fabrication that can achieve multi-layer structures is casting of PDMS around a 3D sacrificial structure, which is later removed or dissolved.[22–25] This approach eliminates the alignment and bonding issues of layered approaches, however these methods often require complex protocols involving removal of the sacrificial structure, which can limit the geometry, impact yield, or again, require skilled manual processing. The third category that has shown particular promise is the mould based 'membrane sandwich' approach, first presented by the Whitesides research group.[26] This fabrication technique simplifies the fabrication of layered channel structures by sandwiching PDMS pre-polymer between a patterned wafer based mould and a passivated PDMS mould. This approach has the advantage of simplifying processing and offers simple mould removal. However, while fabrication techniques have been developed along similar lines,[27] there are few reports of complex microfluidic devices realised using this approach, and it would appear that this technique has not been widely adopted and developed by the community.

In this paper, we present an enhanced membrane sandwich based microfluidic fabrication technique, which enables accessible monolithic integration of complex microfluidic structures such as valves, as well as hybrid integration of various functional elements, such as commercial porous membranes used as interfaces between microfluidic channels on different vertical planes. This one step process realises multi-layer microfluidic structures utilising reusable moulds fabricated with high-resolution photolithography as well as rapid and flexible direct 3D printing. We demonstrate the utility of our approach through realisation of an *in vitro* platform simulating the brain blood barrier, and also pneumatic valves, which can regulate pressurised fluid flow.

Concept

Consider the situation illustrated in Fig. 1. If two complementary moulds are placed in contact and PDMS pre-polymer is injected between them, then small voids between the moulds will be filled with PDMS, allowing two independent channels to be formed, which are isolated vertically by a PDMS membrane of controlled thickness. Sufficiently thin membranes could be realised to allow pneumatic distortion in order to achieve valves. If the two moulds are designed to make contact and are pressed together firmly while injecting and curing the PDMS, it should be possible to exclude the PDMS from between the two moulds that are in contact, creating vertical interfaces between the microfluidic channels on different layers, allowing

controlled interconnects or isolated overpasses as required. Functional structures could also be embedded within the PDMS block and interfaced to the microfluidic channels from both sides.

Fig. 1 conceptually illustrates the fabrication technique with Fig. 1A–F, illustrating the two mould halves being automatically aligned by peg and hole structures in the mould. The moulds are brought into contact, PDMS is injected to fill voids and create a PDMS slab, followed by mould release and final chip assembly.

Fig. 2A–D illustrate how prefabricated functional structures can be integrated into microfluidic systems using this fabrication technique. Complementary mould structures are positioned to sandwich an aligned prefabricated functional device, in this case a porous membrane, to achieve a fluidic channel co-culture chip.[11] The complementary mould structures are brought into contact, applying pressure to both sides of the sandwiched device. PDMS is then injected into the mould structure to fill the voids, fully encapsulating the device with the exception of the area excluded by pressure with the raised channel structures within the mould. This approach allows for robust integration of the prefabricated device, interfaced to the microfluidic channels within the PDMS slab.

This fabrication technique can also be applied to realise robust monolithic double-layer functional structures, including pneumatic valves and pumps. Fig. 3A–D illustrate the concept used to fabricate normally-closed, pneumatically actuated valves[28,29] The complementary mould halves are initially self-
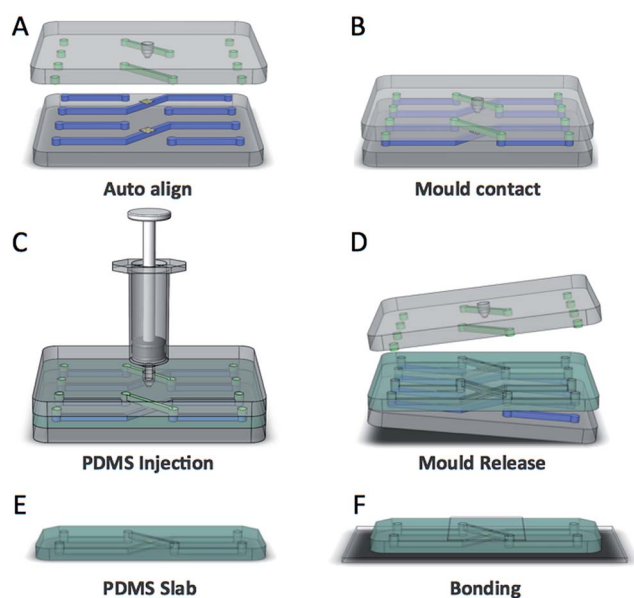
Fig. 1 Conceptual illustration of PDMS injection moulding fabrication technique. (A) Complementary mould halves are initially loaded with a functional substrate for integration, (B) the moulds are then brought into contact and clamped, (C) degassed PDMS is injected through an opening and fills voids between the mould structures. The mould assembly is then placed in an oven at 70 °C for one hour until cured (D and E) upon removal of the mould structure the resultant double sided PDMS slab is cut to size, and channels on either side of the slab are sealed with glass slides.
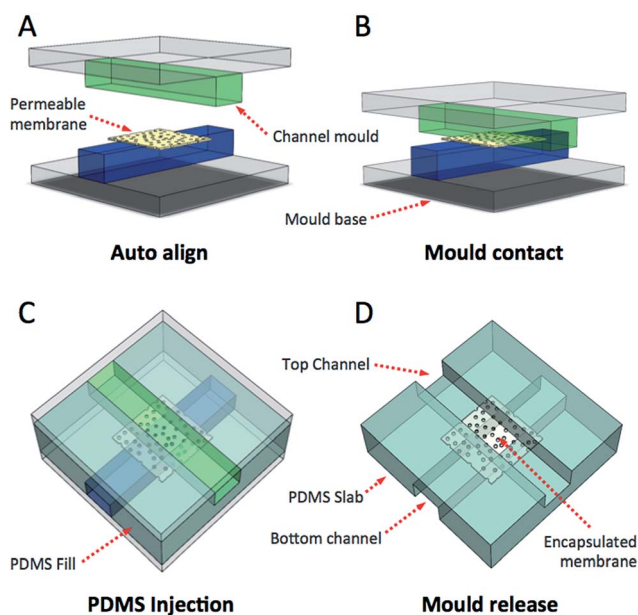
Fig. 2 Concept for integration and encapsulation of prefabricated functional components. (A) Transwell permeable support membrane is placed on a point of intersection of the microfluidic mould structures, (B) the complimentary mould structures are then brought into intimate contact and clamped, (C) PDMS is then injected through an opening and fills the voids between moulds, (D) during this process PDMS infiltrates all areas of the membrane not mechanically compressed, resulting in clear areas at the channel intersection and mechanically encapsulated areas without.
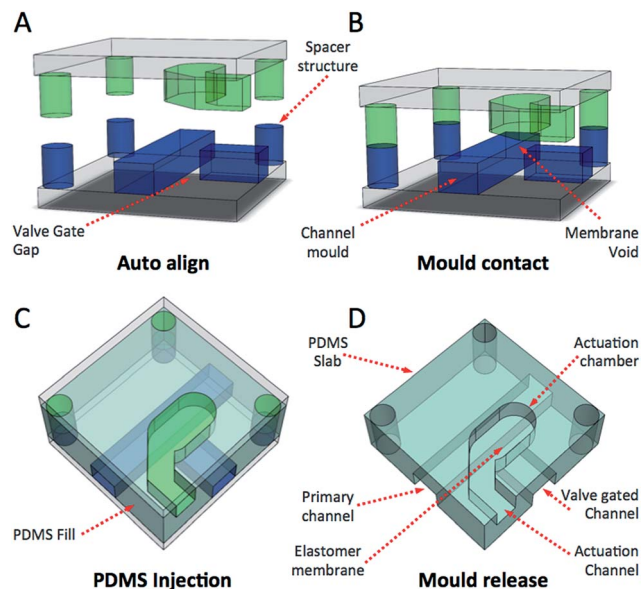
Fig. 3   Concept for fabrication of active elastomer structures. (A) The mould halves are designed so as to not quite contact at the location of the valve. (B) The mould halves are again brought into contact leaving a narrow void in the region of the valve, (C) PDMS is injected forming a membrane between the two channels, (D) the valve gate can be actuated through application of negative pressure in the actuation chamber.

aligned and brought into contact. A spacer structure, either directly integrated into the mould or added during moulding depending on the mould fabrication technique used, keeps the moulds separated. The top and bottom moulds are thereby defined such that a certain gap is maintained between the top and bottom channels, allowing injected PDMS to fill the void and form a membrane between them.

Mould fabrication

In this work, moulds have been realised utilising various microfabrication methods. Standard photolithography microfabrication techniques have been used to create wafer-based moulds for high-resolution applications, while larger structures for low-resolution rapid prototyping applications have been fabricated using 3D printing.

In the case of photolithographically defined moulds, at least one of the mould halves must be optically transparent to allow manual alignment of complementary channels. For this reason, one mould half was patterned onto a 3-inch 2 mm thick borosilicate glass substrate, with the corresponding half patterned on a 4-inch silicon wafer substrate. A borosilicate substrate was used as the top mould as it is optically transparent, allowing for manual alignment. A thickness of 2 mm was used to ensure structural integrity and facilitate the drilling of a 4 mm Luerconnector interface hole for PDMS injection. A 4-inch, 500 µm thick silicon wafer was used as the bottom substrate as silicon has better photoresist adhesion properties than glass. SU-8 3050 series photoresist (MicroChem Corp) was used to produce

channel mould structures with a height of 200 µm. The silicon mould half is coated with a 20 nm titanium adhesion layer, followed by a 200 nm gold layer applied using sputter coating. This provides a non-reactive, passivated surface, which facilitates ease of mould release. Upon completion, the two substrates are sandwiched, as outlined in Fig. 1. The 4 mm hole in the top mould half allows coupling with lure type syringe connectors, highly degassed PDMS is introduced through this opening, and the entire structure is clamped and placed in an oven at 70–80 °C to cure. After curing, the two mould halves are carefully opened. The cast PDMS structure begins to separate from the mould spontaneously due to differential thermal contraction of the mould and PDMS, releasing from the passivated mould half first. The slab can then be cut to size and peeled from the unpassivated mould half and the de-moulded PDMS part can then be permanently bonded using oxygen plasma treatment to sealing glass slides. For further information on injection moulding protocol see ESI S1.† The use of standard photolithographic microfabrication techniques allows for fabrication of high-resolution structures, however the fabrication process is labour-intensive and requires cleanroom facilities.

In contrast, 3D printing can be used to directly print complementary mould structures.[25,30] This was achieved using a Projet 7000 HD 3D Printer (3DSystems Rock Hill, South Carolina) using the photo curable polymer VisiJet® SL Clear (3DSystems Rock Hill, South Carolina). Structures printed using this material require a post print processing step[25] in order to successfully mould PDMS. This approach allows rapid prototyping when very high-resolution structures are not required, with minimum dimensions defined by the resolution of the 3D printer. In the case of the Projet 7000 3D Printer, 100 µm structures can be fabricated in a reproducible manner. Use of 3D printing, while only applicable for low-resolution structures, greatly simplifies the fabrication process. 3D printing allows for fabrication of vertically tapered structures of varied height,[31] such as the otherwise drilled 4 mm Luer-connector interface hole as well as alignment pins and matched wells. These alignment structures can be fabricated directly into the mould structure, and can be used to self-align the mould structures, eliminating the requirement for manual alignment, and similarly the requirement for optically transparent substrates. Demoulding of the PDMS from the 3D printed moulds was not spontaneous and required manual removal of the PDMS part, this could be due to various factors, such as the different thermal characteristics of the material, as well as lower curing temperature required to avoid mould damage, the absence of a passivated surface, or due to the slightly textured surfaces that result from the 3D printing process. However, manual demoulding was relatively straightforward due to the larger feature sizes of the 3D print moulded parts.

Results

The technique presented in this paper produces monolithic double-layer PDMS structures, and robust integration of functional structures, fabricated using a one-step process, allowing

PDMS to form as a singular slab. Being a single block of PDMS, this monolithic structure is capable of withstanding high pressure and mechanical forces when compared with bonded multi-layer structures. Utility of this technique was verified through realisation of an *in vitro* microfluidic co-culture platform with integrated Transwell permeable support cell culture scaffold structures (Corning Inc.) useful for various organ-on-a-chip research platforms[11,32–35] and also normally-closed pneumatically actuated valves, similar to previous examples from the literature.[28,29]

Encapsulation of Transwell permeable supports

Application of this technique results in robust integration of Transwell membranes, similar in function to those integrated into other microfluidic systems using standard lamination techniques,[36] however embedded in a more robust structure.

Fig. 4 shows a microfluidic research platform fabricated using our novel technique, similar in concept to the *in vitro* blood brain barrier (BBB) microfluidic model demonstrated by

Fig. 4 Shows a Transwell permeable support fully encapsulated in PDMS, in the context of an *in vitro* model of the blood brain barrier. (A) A tissue culture research platform fabricated using the elastomer injection moulding technique. (B and C) Schematic and cross sectional illustration of the membrane area, illustrating the membrane location within the device. (D and E) The point at which the two channels intersect, allowing access to both sides of the permeable support, images obtained using scanning electron microscopy. (F) Representative image of a confocal microscope, demonstrating a monoculture of human endothelial cells cultured within the device; filamentous actin in red, nuclei in blue. (G and H) Phase contrast images of endothelial cells and astrocytes cultured within the micro-channels, as part of a co-culture system.

Booth and Kim 2012.[36] We established a contact model of the BBB in our device through co-culture of primary human brain microvascular endothelial cells (ACBRI 376, Cell-Systems Corporation, Kirkland, USA) together with human transformed foetal astrocytes (a cell-line termed SVG,[37] Burnet Institute, Melbourne, Australia), on opposite faces of the embedded membrane. Co-culture was achieved using processes outlined in our previous work[38] adapted for culture within a microfluidic flow based environment, similar to the process outlined in ref. 36. In brief, endothelial cells are seeded into a fibronectin-treated (Cat. # F1141, Sigma-Aldrich, Australia) channel and allowed to adhere for 2–4 h. The device is then flipped and astrocytes are introduced into the channel interfacing the opposite side of the membrane. Cells are subsequently grown to confluence for 24–48 h under shear stress of 1 dyn cm^{-2} prior to experimentation. A detailed culture protocol is specified in ESI S2.† As a major improvement to similar flow devices[36] or to static BBB models,[38,39] our platform is designed to allow high-resolution microscopic access to both sides of the integrated membrane, enabling real-time monitoring of either cell type within the co-culture; since the chip is symmetrical and horizontally opposed, a simple rotation over a microscope objective becomes possible.

Fig. 4 shows a 3 μm pore Transwell permeable support integrated with microfluidic channels and encapsulated within PMDS. Fig. 4C illustrates a cross section of the membrane area; the flat area has been compressed by contact between the two moulds, while areas of membrane not compressed during moulding extend into the PDMS slab and are fully encapsulated. Scanning electron microscope images, Fig. 4D and E further demonstrate how the channels cross at this intersection point with the membrane, forming a permeable barrier between channels. PDMS pre-polymer fluid has a low surface tension and can easily infiltrate very thin gaps. This assists the encapsulation process by fully infiltrating the individual pore structures of the Transwell support in areas of the membrane that are not pressed against the mould during injection moulding, as seen in the lower right of Fig. 4E. This process however does not occur in areas of the membrane which are pressed against the mould structures, as can be seen in the flat region on the top left of Fig. 4E, demonstrating that with this technique, it is possible to choose where the PDMS will infiltrate and where it will be excluded. Gas bubbles trapped at feature edges or small void features (such as membrane pores) can be avoided by degassing PDMS pre-polymer under high vacuum conditions prior to injection. Once thoroughly degassed, the pre-polymer is able to absorb small bubbles prior to cure, resulting in defect free casting.

Finally, as shown in Fig. 4F–H, our channels are fully compatible with cell growth and micro-imaging. Fluorescence confocal microscopy (Fig. 4F; Nikon A1r+ confocal microscope) demonstrates actin filaments and nuclei of endothelial cells cultured on the porous membrane embedded within our device. Furthermore, as shown by phase contrast microscopy (Fig. 4H), both endothelial cells and astrocytes reach confluence within the micro-channels and cover the entire channel and membrane areas. Hence, our model is well-suited for biological
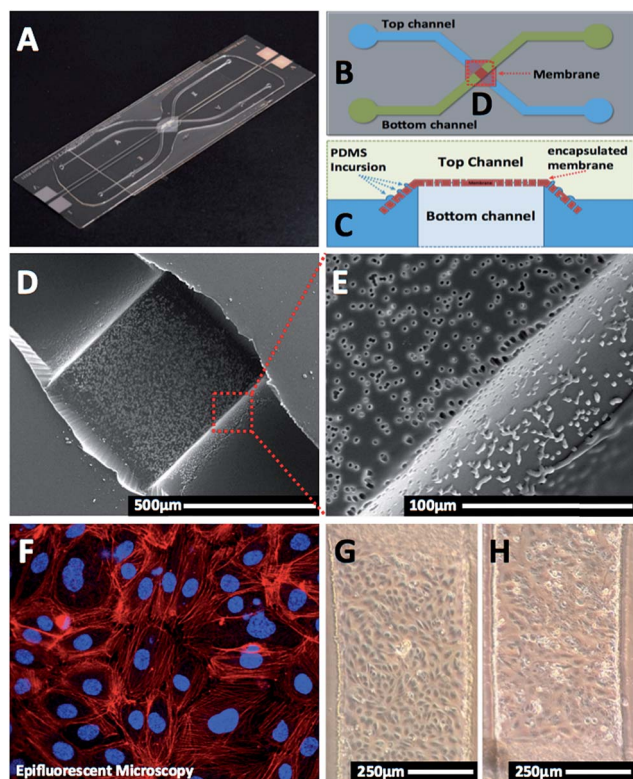
experiments not only in the context of the BBB, but also for numerous other applications. Additional details regarding cell culture protocols are included in ESI S2.†

Normally-closed pneumatically-actuated elastomer valves

Application of this technique results in robust elastomer double-layer structures, and as a proof-of-concept was applied in the context of normally-closed pneumatically actuated elastomer valves, similar in principle, to previous reports,[28,29] however, with an inherently more robust monolithic structure, and significantly simplified fabrication process.

As with many normally-closed elastomer valve approaches, undesirable irreversible bonding of the valve gate to the channel sealing substrate can occur. During proof-of-concept experiments, this bonding was avoided by selective PDMS passivation using manual application of ink to the valve gate followed by post bonding ethanol wash out.[40] To avoid this bonding on a larger scale, and with increased reproducibility, various other solutions such as valve actuation prior to bonding,[28] or selective surface de-activation[41] can be applied, while the problem can also be avoided using reversible pressure bonding with a clamp structure.
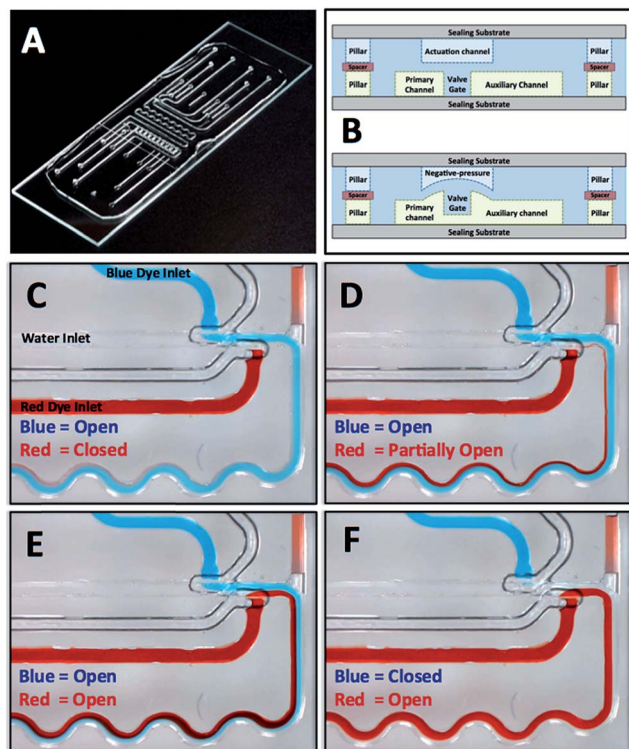

Fig. 5 Pneumatically actuated, normally-closed elastomer valves fabricated using PDMS injection moulding with direct 3D printed mould structures. (A) Shows a proof-of-concept prototype microfluidic system used to demonstrate valve functionality, (B) shows a conceptual illustration outlining the functional principal of the valves, (C–F) demonstrate operation of these valves as fluidic resistors. Water is introduced at the primary inlet using a syringe pump, and the dyed inlets are fed by reservoirs maintained at slightly positive pressure. Valve actuation chambers are manually pressurised using a syringe to produce full or partial opening of blue and red dye gates.
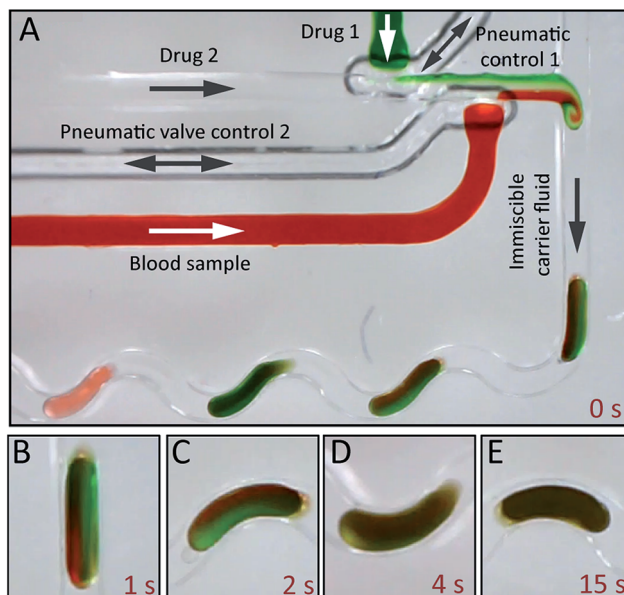
Fig. 6 (A) Application of the pneumatically actuated on chip valves in use as flow regulators of pressure driven fluids in a droplet slug based system. This system is an initial proof-of-concept prototype utilising these valves to actively modulate the component of coloured water dispensed into each droplet, and is planned for investigating the effects of various drug concentrations and combinations on the morphology of blood cells under flow, (B–E) show mixing of reagents within a slug at various time points.

Fig. 5 illustrates validation of these valves, Fig. 5A shows an assembled chip, while the cross section in Fig. 5B conceptually demonstrates operation of these valves. Pressurising the actuation chamber relative to the valve gate will close the valve; while evacuating the actuation chamber opens the valve. Applying an intermediate pressure can result in a partially open valve with finite fluidic resistance. In this proof-of-concept demonstration, this pressurisation and evacuation is achieved manually using a syringe.[42] Fig. 5C–F qualitatively illustrate the valves in use as variable flow resistors, controlling the confluent flow of water, and coloured water with food dye (further detail provided in ESI S3 and Video 1†).

Fig. 6 illustrates valves fabricated using this method modulating the concentration of reagents added to fluid slugs to allow rapid microfluidic mixing. In this arrangement, valves can be used to apply known ratios of fluid to the droplet stream, or fully isolate the dye channel, as would be required in research platforms investigating the effects of known volumes of drug to blood droplets. Fig. 6A shows the system configured as in Fig. 5, however with the addition of an immiscible fluid flow from the top channel, operation of the system is demonstrated in ESI Video 1.†

Discussion

Most reported fabrication techniques for encapsulation of functional substrates within PDMS, or fabrication of elastomer valves, involve the stacking and bonding of multiple layers of

PDMS thin films patterned with channel structures. Valves are commonly fabricated using this method,[28] and thin structures can be integrated by lamination between these PDMS films, so long as they are thin enough to allow sufficient adhesion of PDMS layers.[32] While these approaches are well-established, they are time-consuming, labour-intensive and error-prone, as all layers must be fabricated, aligned and bonded individually. These techniques can also lead to platforms that are prone to failure due to leakage caused by various defects, which can occur under different circumstances, including when the layers are not correctly aligned and wrinkles form, when debris is caught in between the two layers, when a pressure differential between the closed channel and ambient environment is significant enough to delaminate the PDMS layers, or a combination of these factors.[43]

While bonded multi-layer integration of devices within PDMS is limited to devices thin enough to allow for mechanical deformation of the PDMS to form a seal around the edges, this technique fully encapsulates all surfaces of the device not within the deliberate exclusion zones of the mould, and for this reason is not limited to integration of thin devices. Comparing the practicality of 3D printed and photolithographic moulds: fabrication using 3D printing allows rapid and arbitrarily reconfigurable prototyping and automatic mechanical mould alignment, however resolution and surface smoothness is limited by the printer used, various materials used in stereolithography require post-print processing steps and mould release is more challenging with these materials. Photolithographically defined moulds allow significantly higher resolution, however require cleanroom fabrication facilities, and make multi-layer moulds cumbersome, limiting the options for automatic mechanical alignment and thereby requiring transparent substrates.

Another consideration is the ease with which the PDMS structure can be de-moulded. In our experiments de-moulding of photolithographically defined moulds begins spontaneously, driven by thermal contraction, whereas the 3D printed moulds required manual removal of the part, however this was relatively straightforward. It is anticipated that design of the mould, cooling protocol and selective surface treatments could be optimised to enhance and control the thermal contraction de-moulding process. It may also be possible to inject gas into the mould to make the cooling and de-moulding even more rapid for scaling to automatic and rapid throughput for both photolithographic and 3D printed moulds. These investigations will be pursued in future work.

Conclusions

We have shown a practical method for the fabrication of monolithic microfluidic devices with complex 3D structures. This method allows for the integration of devices that enable complex functionality for microfluidic systems. This method is also suited to rapid prototyping and reduces fabrication error compared to established methods, allowing for more reliable and complex microfluidic chips to be realised in a short time. This technique allows for reduction in fabrication complexity, while allowing for increase in functional complexity, and could be applied to significantly simplify the fabrication of complex valve based research platforms such as those seen in large scale integration approaches.[12,44] Future research will investigate hybrid integration of various modular components such as membranes, electrodes, piezo-actuators, heaters, pressure sensors and biosensors within lab-on-a-chip platforms, with the potential of retaining high-resolution optical access. This technique can also take advantage of the emergence of high resolution 3D printing, enabling reusable moulds for very complex systems incorporating both valve membranes and hybrid integrated elements to be realised rapidly and reliably and should thus mark a major acceleration in the application of microfluidic platforms.

Acknowledgements

References

1 P. N. Nge, C. I. Rogers and A. T. Woolley, *Chem. Rev.*, 2013, **113**, 2550–2583.
2 K. S. Elvira, X. C. i. Solvas and R. C. R. Wootton, *Nat. Chem.*, 2013, **5**, 905–915.
3 P. M. Valencia, O. C. Farokhzad, R. Karnik and R. Langer, *Nat. Nanotechnol.*, 2012, **7**, 623–629.
4 K. Ren, J. Zhou and H. Wu, *Acc. Chem. Res.*, 2013, **46**, 2396–2406.
5 J. Kim, E. C. Jensen, A. M. Stockton and R. A. Mathies, *Anal. Chem.*, 2013, **85**, 7682–7688.
6 E. K. Sackmann, A. L. Fulton and D. J. Beebe, *Nature*, 2014, **507**, 181–189.
7 B. Xiong, K. Ren, Y. Shu, Y. Chen, B. Shen and H. Wu, *Adv. Mater.*, 2014, **26**, 5525–5532.
8 E. W. Esch, A. Bahinski and D. Huh, *Nat. Rev. Drug Discovery*, 2015, **14**, 248–260.
9 N. Gupta, J. R. Liu, B. Patel, D. Solomon, B. Vaidya and V. Gupta, *Bioengineering & Translational Medicine*, 2016.
10 T. A. Nguyen, T.-I. Yin, D. Reyes and G. A. Urban, *Anal. Chem.*, 2013, **85**, 11068–11076.
11 M. W. van der Helm, A. D. an der Meer, J. C. Eijkel, A. van den Berg and L. I. Segerink, *Tissue Barriers*, 2016, **4**, e1142493.
12 I. E. Araci and P. Brisk, *Curr. Opin. Biotechnol.*, 2014, **25**, 60–68.
13 A. K. Au, H. Lai, B. R. Utela and A. Folch, *Micromachines*, 2011, **2**, 179–220.

14 J. C. McDonald and G. M. Whitesides, *Acc. Chem. Res.*, 2002, **35**, 491–499.

15 S. Halldorsson, E. Lucumi, R. Gómez-Sjöberg and R. M. Fleming, *Biosens. Bioelectron.*, 2015, **63**, 218–231.

16 M. A. Unger, H.-P. Chou, T. Thorsen, A. Scherer and S. R. Quake, *Science*, 2000, **288**, 113–116.

17 B.-H. Jo, L. M. Van Lerberghe, K. M. Motsegood and D. J. Beebe, *J. Microelectromech. Syst.*, 2000, **9**, 76–81.

18 J. C. Love, J. R. Anderson and G. M. Whitesides, *MRS Bull.*, 2001, **26**, 523–528.

19 A. D. Stroock and G. M. Whitesides, *Electrophoresis*, 2002, **23**, 3461–3473.

20 M. Zhang, J. Wu, L. Wang, K. Xiao and W. Wen, *Lab Chip*, 2010, **10**, 1199–1203.

21 J. Kim, A. M. Stockton, E. C. Jensen and R. A. Mathies, *Lab Chip*, 2016, **16**, 812–819.

22 Y. Hwang, O. H. Paydar and R. N. Candler, *Sens. Actuators, A*, 2015, **226**, 137–142.

23 Y. He, J. Qiu, J. Fu, J. Zhang, Y. Ren and A. Liu, *Microfluid. Nanofluid.*, 2015, **19**, 447–456.

24 V. Saggiomo and A. H. Velders, *Adv. Sci.*, 2015, **2**, DOI: 10.1002/advs.201570033.

25 H. N. Chan, Y. Chen, Y. Shu, Y. Chen, Q. Tian and H. Wu, *Microfluid. Nanofluid.*, 2015, **19**, 9–18.

26 J. R. Anderson, D. T. Chiu, R. J. Jackman, O. Cherniavskaya, J. C. McDonald, H. Wu, S. H. Whitesides and G. M. Whitesides, *Anal. Chem.*, 2000, **72**, 3158–3164.

27 J. Hansson, M. Hillmering, T. Haraldsson and W. van der Wijngaart, *Lab Chip*, 2016, **16**, 1439–1446.

28 R. Mohan, B. R. Schudel, A. V. Desai, J. D. Yearsley, C. A. Apblett and P. J. A. Kenis, *Sens. Actuators, B*, 2011, **160**, 1216–1223.

29 J. Kim, M. Kang, E. C. Jensen and R. A. Mathies, *Anal. Chem.*, 2012, **84**, 2067–2071.

30 G. Comina, A. Suska and D. Filippini, *Lab Chip*, 2014, **14**, 424–430.

31 S. Waheed, J. M. Cabot, N. P. Macdonald, T. Lewis, R. M. Guijt, B. Paull and M. C. Breadmore, *Lab Chip*, 2016, **16**, 1993–2013.

32 A. Wolff, M. Antfolk, B. Brodin and M. Tenje, *J. Pharm. Sci.*, 2015, **104**, 2727–2746.

33 J. D. Caplin, N. G. Granados, M. R. James, R. Montazami and N. Hashemi, *Adv. Healthcare Mater.*, 2015, **4**, 1426–1450.

34 J. S. Lee, R. Romero, Y. M. Han, H. C. Kim, C. J. Kim, J.-S. Hong and D. Huh, *J. Matern.-Fetal Neonat. Med.*, 2016, **29**, 1046–1054.

35 J. Ribas, H. Sadeghi, A. Manbachi, J. Leijten, K. Brinegar, Y. S. Zhang, L. Ferreira and A. Khademhosseini, *Applied In Vitro Toxicology*, 2016, **2**, 82–96.

36 R. Booth and H. Kim, *Lab Chip*, 2012, **12**, 1784–1792.

37 E. O. Major, A. E. Miller, P. Mourrain, R. G. Traub, E. De Widt and J. Sever, *Proc. Natl. Acad. Sci. U. S. A.*, 1985, **82**, 1257–1261.

38 B. Niego and R. L. Medcalf, *J. Visualized Exp.*, 2013, e50934.

39 B. Niego, R. Freeman, T. B. Puschmann, A. M. Turnley and R. L. Medcalf, *Blood*, 2012, **119**, 4752–4761.

40 J. Y. Baek, J. Y. Park, J. I. Ju, T. S. Lee and S. H. Lee, *J. Micromech. Microeng.*, 2005, **15**, 1015.

41 S. CaiáLesher-Perez, *Lab Chip*, 2011, **11**, 738–742.

42 D. Irimia and M. Toner, *Lab Chip*, 2006, **6**, 345–352.

43 I. E. Araci, P. Pop and K. Chakrabarty, *IEEE Design & Test*, 2015, vol. 32, pp. 8–19.

44 P. Pop, W. H. Minhass and J. Madsen, *Microfluidic Very Large Scale Integration (VLSI)*, Springer, 2016.

CHAPTER 3: Complex microfluidics for photonic biosensor applications: Point of care, and sophisticated research platforms.

The overall hypothesis of this thesis is that overcoming fabrication challenges generally associated with complex multilayer microfluidic systems, will greatly increase their accessibility, therefore providing a pathway for widespread acceptance. The previous chapter outlined a fabrication method intended to simplify fabrication, while allowing scaling on-chip circuit complexity and functionality, it was shown that membranes and valves could be fabricated with relative ease, however it is not yet known whether this apparent advancement in fabrication of complex microfluidics will actually benefit real world applications. In particular, it is postulated that a sufficiently simplified fabrication technique, reducing iterative cyclic development time will enable accelerated prototype development which can enable researchers unfamiliar with multilayer microfluidics to rapidly adopt this technology.

This chapter explores this hypothesis by engaging in short term collaborations with two researchers who are not experts in microfluidics and rapidly advance their research using complex microfluidics. The chosen field of application for this chapter is photonics biosensors. Photonic biosensors are among the most sensitive biomarker detection technologies [46], and for this reason would be well suited to point-of-care diagnostic applications, and sophisticated research platforms. As a caveat, this kind of biosensor usually requires careful fluid handling strategies, requiring a series of carefully isolated fluids introduced in a defined sequence, which presents a challenge for point-of-care application. In addition, photonic biosensors require careful and precise environmental control. Photonic biosensors are exceedingly sensitive to bulk refractive index changes within the surrounding media, as can be introduced for example through changes in temperature and osmolarity of the media. The requirement for fluidic isolation and well controlled sample handling necessitates some manner of fluidic automation capable of environmental control to enable practical point-of-care application.

17

The work in this chapter is presented in the form of two journal articles specifically in the context of waveguide based, automated point-of-care sensing of dissolved analytes (Section 3.1), and plasmonic based monitoring of the secretion of single cells (Section 3.2).

The outcome of this work has demonstrated that removing the fabrication bottleneck generally associated with complex multilayer microfluidic systems, through deployment of the fabrication technique outlined in chapter 2, allows access to applications otherwise considered prohibitively difficult when limited to traditional fabrication methods.

Section 3.1 has demonstrated on-chip fluid automation approaches adapted to provide assay automation of an integrated photonic biosensor, with rapid fabrication turnaround offered by the technique outlined in chapter 2 allowing rapid integration of various control components.

Section 3.2 has shown adaptation of the fabrication technique to include well defined membranes for sophisticated environmental control of a single cell analysis platform, demonstrating the techniques capacity for rapid reconfigurability.

The Applications explored in this chapter have demonstrated that the fabrication technique outlined in chapter 2, does provide the fabrication timeframes required for rapid prototyping, allowing iterative design improvements, with turnaround within a couple of days. This proved crucial as designs were iteratively improved to deal with various unforeseen issues. Valve geometry was one such issue, it was necessary to scale the valves in an effort to condense complex fluid handling structures into the real-estate available, this resulted in initial performance short of that expected. Adhesion of the valve gates with the channel floor was one of the primary issues encountered as a result of scaling, as well as valve gates closing with sufficient speed to allow efficient pump operation. While it was possible to avoid adhesion through improvement of valve geometry, closing speed was improved through application of positive pressure to actively close valve gates. This led to additional issues, with positive pressure actively permeating gas across valve membranes to form bubbles within the system, requiring additional re-design of the fluidic systems and careful control of the pressure levels applied. The speed and reliability of the platform

18

introduced in Chapter 2 enabled the entire study of Section 3.1 to be completed during a 6 month visit to the ICN2 labs with Laura Lechuga and the study of Section 3.2 to be completed remotely in collaboration with EPFL even though 4 iterations of the microfluidics were required to achieve the final outcome.

Overall the fabrication approach of Chapter 2 has demonstrated significant benefit for research prototype development. However, to really prove value in point-of-care context, the platform should be demonstrated to function with more complex biological samples, for example with whole human blood and with repeatability and reliability required for clinical trials and ultimately mass deployment.

During the scope of this work, all pneumatic driven on chip components were actuated either manually for simple static applications, with a syringe or manual pump, or for complex dynamic automated applications, through implementation of a custom-built programmable valve driver system. The valve driver is a pneumatic system with two pressure vessels held one at higher and one lower than ambient pressure, with solenoid valves switching between the two and supplying this to on-chip control elements. it became apparent during this work that access to this valve driver represented an additional barrier for continued use of dynamic automated microvalve based microfluidic technology.

As further work beyond the scope of this doctorate, I would suggest development of a standardised automated programable control interface that can be readily deployed to end users, with a similar design rationale as a motherboard supporting a central processing unit. If such supporting equipment could be simplified and developed to the point that it was relatively cheap and easy to deploy, similar to a benchtop syringe pump, this may reduce the barrier for uptake of automated microvalve based fluid handling systems.

3.1 – An automated optofluidic biosensor platform combining interferometric sensors and injection moulded microfluidics

A primary factor limiting development and application of point-of-care diagnostic systems, is practical integration of biosensors with robust microfluidic handling systems, capable of automating assay processes required for operation [46]. As such, point-of-care application is identified as a field highly dependent on realisation of a simple, scalable and robust fabrication method, as required for high volume production. It is evident that point-of-care applications in particular would benefit from the automation and precision that complex multilayer microfluidic systems should provide.

While various microfluidic automation approaches exist, most of those that achieve fluidic isolation depend on valving components that require complex and time-consuming fabrication techniques, unsuited to rapid fabrication and incompatible with mass fabrication techniques [12, 19].

The paper of this section investigates whether an automated fluid handling system utilising lifting gate pneumatic microvalves [41] can be fabricated with the technique explored in Chapter 2, and whether this fabrication technique allows prototyping with short turnaround time and hence allows rapid iterative improvement.

This paper was the result of a collaborative project with the Nanobiosensors and bioanalytical applications group at ICN2 in Barcelona, the system was designed to facilitate point-of-care implementation of the Bimodal waveguide photonic biosensor developed by this group.

The paper demonstrates that it is practical to integrate complex microfluidic devices fabricated with the method outlined in chapter 2, with an active photonic biosensor platform, using dynamic control components to actuate fluids required for automation of a complex immunoassay.

The work related to this chapter has been peer-reviewed and published in: ***Lab on a chip***

The paper can be obtained via the DOI: 10.1039/C7LC00524E [30]

My role in this work was to design and fabricate fluidic systems, run biosensor experiments and write the majority of the manuscript. Others assisted with manufacture of the support equipment, assisted with experimental design, directed the surface functionalisation strategy employed and various other supporting roles. My leading role in this research is reflected in my being listed as first author.

Lab on a Chip

An automated optofluidic biosensor platform combining interferometric sensors and injection moulded microfluidics†

C. Szydzik,[a] A. F. Gavela,[b] S. Herranz,[b] J. Roccisano,[a] M. Knoerzer,[a] P. Thurgood, [iD] [a] K. Khoshmanesh, [iD] [a] A. Mitchell[a] and L. M. Lechuga [iD] *[b]

A primary limitation preventing practical implementation of photonic biosensors within point-of-care platforms is their integration with fluidic automation subsystems. For most diagnostic applications, photonic biosensors require complex fluid handling protocols; this is especially prominent in the case of competitive immunoassays, commonly used for detection of low-concentration, low-molecular weight biomarkers. For this reason, complex automated microfluidic systems are needed to realise the full point-of-care potential of photonic biosensors. To fulfil this requirement, we propose an on-chip valve-based microfluidic automation module, capable of automating such complex fluid handling. This module is realised through application of a PDMS injection moulding fabrication technique, recently described in our previous work, which enables practical fabrication of normally closed pneumatically actuated elastomeric valves. In this work, these valves are configured to achieve multiplexed reagent addressing for an on-chip diaphragm pump, providing the sample and reagent processing capabilities required for automation of cyclic competitive immunoassays. Application of this technique simplifies fabrication and introduces the potential for mass production, bringing point-of-care integration of complex automated microfluidics into the realm of practicality. This module is integrated with a highly sensitive, label-free bimodal waveguide photonic biosensor, and is demonstrated in the context of a proof-of-concept biosensing assay, detecting the low-molecular weight antibiotic tetracycline.

[a] School of Engineering, RMIT University, Melbourne, Australia
[b] Nanobiosensors and Bioanalytical Applications Group. Catalan Institute of Nanoscience and Nanotechnology (ICN2). CSIC, CIBER-BBN and The Barcelona Institute of Science and Technology, Campus UAB, Bellaterra, 08193 Barcelona, Spain. E-mail: Laura.lechuga@icn2.cat
† Electronic supplementary information (ESI) available. See DOI: 10.1039/c7lc00524e

Introduction

Photonic biosensors enable cost-effective, highly sensitive, and selective label-free detection of target biomarkers,[1–3] they require relatively simple support equipment and software to operate and a minimal physical footprint.[4] With appropriate functionalisation strategies, these biosensors can be reused multiple times[5] and have been shown to be capable of exceedingly low limits of detection.[6,7] While photonic biosensors are among the most highly sensitive biosensor technologies available,[2] many of their other unique characteristics are highly attractive for point-of-care applications, in which devices are generally required to be compact, self-sufficient and simple to operate while maintaining reliability, accuracy and reproducibility.[8] Despite these advantages, several challenges exist restricting practical adoption of photonic biosensors for

point-of-care devices.[1] One of the most significant challenges is fluid handling, as photonic biosensors generally require complex flow handling protocols, with sequential application of multiple reagents and a critical need for fluidic isolation. Fluid handling becomes increasingly complex when advanced assays are required, such as competitive immunoassays, commonly applied when the target analyte to be detected is of low molecular weight and is present in very low concentrations, as is the case with pesticides, toxins or antibiotic residues for food control and environmental monitoring applications.[9–11]

The field of microfluidics has been proposed extensively as a solution for point-of-care diagnostic devices for the healthcare sector,[8] and has attracted significant interest in recent years.[12–15] Microfluidic systems intended for point-of-care application must employ simple, ideally automated operational principles, and must maintain compatibility with scalable fabrication techniques suited to mass fabrication.[8,13] As a result, few of the fluid handling strategies commonly employed in point-of-care devices are suited to the specific requirements of photonic biosensors, lacking the necessary dynamic functionality, fluid isolation performance and scalability. Further, although integration of photonic biosensors with complex automated microfluidic systems could provide the level of precise

fluid handling required for point-of-care, merging of these two technologies is currently challenging due to fabrication complexity, and control of the interfaces necessary for the fluid handling protocols required to operate such sensors.

Numerous complex microfluidic fluid manipulation technologies exist in the literature capable of achieving on-chip fluidic isolation. Digital microfluidics,[16] droplet based microfluidics[17] and pneumatic valve based microfluidic systems[18] are some of the common technologies employed to manipulate, isolate and mix precise volumes of fluid on-chip. Among these technologies, pneumatic valve based microfluidic systems demonstrate the highest potential for flexible and scalable integrated platforms. Microfluidic automation of exceedingly complex fluid handling protocols has been achieved utilising pneumatic valve based systems for numerous applications,[18] including lab-on-a-chip platforms,[19–21] and biosensors.[22,23] Of particular interest, this technology has been applied to fluidic automation of photonic biosensors.[24–26] While application of such automated microfluidic systems provides the required fluidic isolation, a high degree of flexibility, and on-chip fluidic control in a manner not otherwise possible, fabrication of the valves required to operate such devices is generally cumbersome, and integration can become difficult to the point of impracticality.

We have recently begun to explore the possibility for complex integrated microfluidics and integrated optics.[27] We present here an automated fluid handling module designed for nanophotonic biosensors with complex valved microfluidics realised utilising a simple one-step injection moulding technique,[28] which can achieve complicated valved microfluidics which significantly reduce fabrication complexity and have the potential for scale-up mass manufacture. We demonstrate the utility of this microfluidic by integrating it with a highly sensitive bimodal waveguide photonic biosensor,[4] and demonstrate the functionality of the complete integrated system by performing repeated automated competitive immunoassays for the detection of an analyte of small molecular weight (the antibiotic tetracycline). The ability to realise such high quality valved microfluidics while maintaining simplicity and scalability renders complex automated microfluidics of the sort required for photonic biosensors practical. This work thus represents a major advancement in the development of practical photonic biosensors for point-of-care applications.

Photonic background

This work harnesses the bimodal waveguide photonic biosensor[4] (BiMW) depicted in Fig. 1, a photonic interferometric sensor design which has demonstrated an outstanding biosensing sensitivity for the detection of diverse biomarkers,[29–31] down to exceedingly low target concentrations in the atto-molar range.[7] bacteria detection at few cfu mL^{-1} (ref. 30) or hormone detection a few pg mL^{-1}.[32] Operation of this sensor is described in detail in previous publications,[4] but for reference a brief description is provided here. In these biosensors, monochromatic visible light is coupled
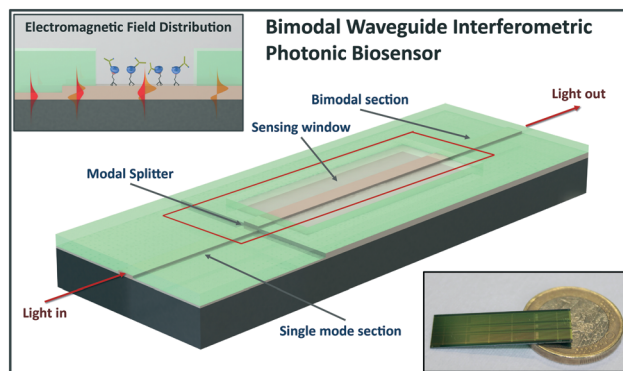

Fig. 1 Scheme illustrating the working principle of a bimodal waveguide biosensor, showing the main components of the bimodal waveguide photonic biosensor; inset top left shows how the electromagnetic field associated with the light beam propagates through the waveguide, while the bottom right inset is a photograph of the chip, shown with a 1-euro coin for reference.

into the photonic chip through a single mode input waveguide (fundamental mode), this mode is then split between two guided modes (fundamental and the first order mode), with the same polarization, through an interface with a step junction in the waveguide geometry. The surface of the biosensor is passivated with the exception of a sensing window, which is functionalised with a specific bioreceptor. Both modes are propagating along the sensing area and their evanescent fields interact with the biomolecules at the waveguide surface. The evanescent fundamental mode penetrates less deeply into the sensing area, and can thus be used as the reference. Any change in the refractive index of the sensing area causes an interference pattern and in turn, a variation of the intensity distribution of the light exiting at the device output. By measuring the output light intensity distribution, the sensor response can be determined.

Fabrication of the bimodal waveguide photonic biosensor is achieved in a cleanroom facility using standard microelectronics techniques as outlined in,[4] silicon nitride (refractive index 2.00) is used in the fabrication of visible wavelength waveguides, with a silicon dioxide cladding layer (refractive index 1.46). The bimodal waveguide is 3 μm in width, has a rib of 1.5 to 3 nm and a thickness of 150 nm (single mode zone) and 340 nm (bimodal zone). The active photonic area of the chip surface is limited to the photonic sensing window etched into the cladding within the bimodal segment of the waveguide, with an area of 15 mm by 50 μm. Multiple devices are fabricated at wafer level, and later divided into individual chips containing 20 BiMW sensors each, separated by 250 μm. Photonic access is achieved through end-fire coupling on the end of the device while output light is collected with a multi-channel photodiode or CCD camera on the other end.

The sensor surface is functionalised through immobilisation of a specific target, and thus, the selective biomolecular recognition which takes place results in a change of the refractive index at the sensor surface, which perturbs the evanescent field and can thereby be detected as changes in the interferometer output.

Microfluidic subsystem integration

Microfluidic design considerations

As described above, a primary issue hindering development of point-of-care photonic biosensor platforms is practical integration with on-chip microfluidic systems, providing automated sample and reagent fluid handling 1. Photonic biosensors generally require fairly complex fluid handling protocols, with multiple fluids manipulated sequentially; in addition, fluidic isolation is required in order to eliminate cross contamination between regents, and flow conditions must be reproducible. Sample volume is ideally kept to a minimum, with channel geometry minimised in order to ensure an adequate mass transport to the sensor surface to avoid unnecessary delays in the biointeraction. In addition, for practical point-of-care applications, any integrated fluidic system must be cheap to manufacture, with simple interfaces and ideally utilise simple and scalable fabrication techniques compatible with mass production.

Our previous work has primarily utilised simple microfluidic systems fabricated using polydimethylsiloxane (PDMS),[4] a biocompatible material commonly used in the fabrication of microfluidic devices.[33] Fluidic isolation was achieved externally through manual valve manipulation, and samples were manually introduced to a sample loop and flushed through the tubing using a syringe pump.

While numerous on-chip fluidic actuation technologies exist in literature, valve based approaches are the best suited to providing fluidic isolation. Due to recent improvements in fabrication techniques,[28] it should be possible to adapt normally closed pneumatically driven on-chip valve based technologies[23] to realise a sufficiently complex, but reliable, valved microfluidic system to automate a photonic BiMW biosensor.
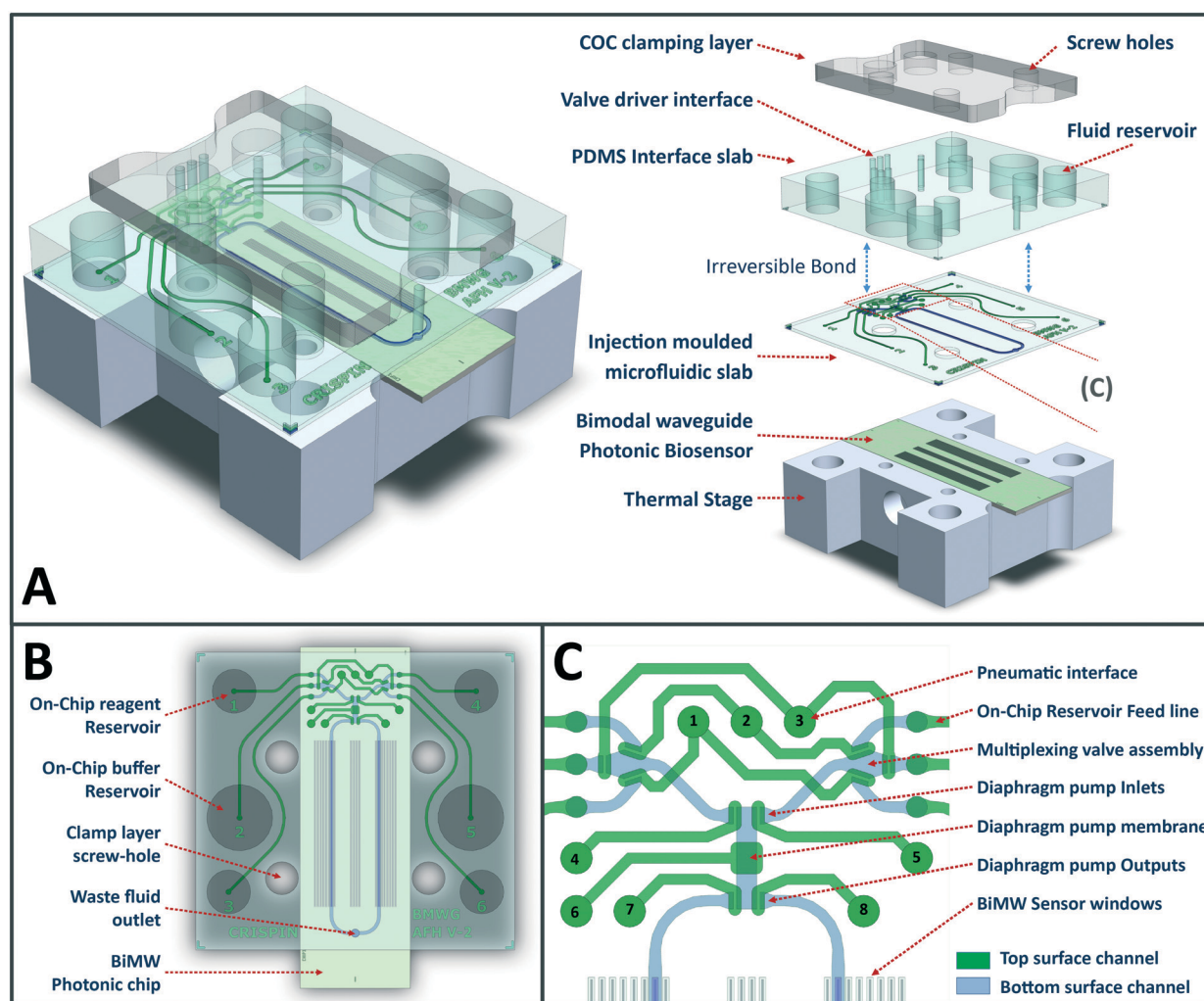
Fig. 2 Schematic of the automated microfluidic module and its various components. Fig. 2A shows a CAD model of the reusable microfluidic module reversibly bonded to the BiMW sensor with a clamp structure, which is fixed to the thermal stage of the setup with screws. Right is an exploded view showing the two primary components, a PDMS interface slab irreversibly bonded to a double sided injection moulded PDMS slab, and a clamping layer. Fig. 2B highlights locations of the primary fluidic reservoirs and overall alignment of the microfluidic and the photonic sensor, while Fig. 2C shows an enlarged schematic of the various active microfluidic components, with features on the top surface of the injection moulded PDMS slab shown in green and the bottom layer shown in blue.

Microfluidic system overview

Fig. 2 presents a diagram of the fluid handling module proposed for automatic operation of the BiMW sensor. Microfluidic channels are patterned into either side of a thin PDMS slab seen in Fig. 2A, utilising an injection moulding fabrication technique. This slab is bonded with a thicker PDMS interface slab, biopsy punched with interfaces and reservoirs of appropriate diameter as seen in Fig. 2B. The PDMS chip is then placed over the BiMW sensor and its associated photonic interface and thermal stage, and clamped in place as outlined in.[4] The module includes several gate valves to control the flow of the various fluids required for biosensing assays. These gate valves are multiplexed to minimise the number of external pneumatic actuators required. The module also includes a single on-chip diaphragm pump to actuate each of the fluids as selected by the gate valve assemblies. All fluidic channels patterned into the module are 250 μm wide, with exception of valve, pump and viaduct structures. The top channels, shown as green in Fig. 2 are 160 μm deep, while all primary fluidic channels patterned on the bottom of the slab, and shown in blue, are 140 μm deep. 6 on-chip fluidic reservoirs, accessible through routing channels in the top layer, are interfaced through 500 μm biopsy punched viaducts from the top to bottom layer. Further detail on functional sub-units is presented below.

Normally closed pneumatically actuated gate valves

The normally closed pneumatically actuated gate valves are illustrated in Fig. 2C. At the centre of each valve is a gate structure, a barrier of PDMS, 400 μm long and 100 μm wide, these gates are normally lowered to close channels, and can be pneumatically lifted to open the channel. This gate is patterned as a protrusion on a thin elastic membrane (60–100 μm thick) which can be deformed. Above this membrane is an oval shaped open channel which acts as an actuation chamber, with a width of 350 μm, length of 750 μm and channel depth of 160 μm. When this chamber is evacuated, the elastomeric PDMS membrane deforms upward, lifting the gate from the bottom of the channel, creating an opening in the barrier and allowing flow across the valve gate. Positive pressure is used to actively and rapidly close the valve gates, and is critical to enabling rapid valve switching, required for efficient pumping. In order to actuate and automate all on-chip valves, a customised external support equipment and software package was developed. This valve driver system operates on a similar principal to those shown in various pneumatically driven on-chip valve systems.[34]

The driver system interfaces with a control computer, and utilises micro-solenoid valves (Burkert Type 6650-189292) to switch between two reservoirs, maintained with an automated pressure regulation sub-system at defined relative pressures of −900 mBar for actuation and +50 mBar for valve closure. A Python script is used to rapidly switch individual solenoid valves in sequences appropriate to operation of on-chip control components.

Multiplexing valve assemblies

Fluidic multiplexing is required to minimize the number of active valve control lines, and thereby to minimise external support equipment. It should be possible to achieve multiplexing, while reducing the chance of fluidic contamination due to dead volume in fluidic junctions, through minimisation of valve size and by optimising valve and channel geometry. Multiplexing is achieved using parallel valve assemblies as shown in Fig. 2C. These assemblies consist of three gate valves, controlling the flow through channels that connect with the on-chip fluid reservoirs. These valves are operated symmetrically, with each of the valves paired with a complementary valve on the opposite assembly. Each assembly is addressed with its corresponding valve on the pump, such that only one of the open pairs is aspirated during pump actuation. These assemblies are designed with an elongated hexagonal geometry, with valve gates placed in a triangular configuration, minimising the distance between valve actuation chambers and minimising fluidic dead volume within the assembly. Running buffer reservoirs feed into the central gate, facilitating washout of the assembly when switching between reservoirs.

On-chip diaphragm pump

On-chip fluid propulsion is a critical function required to achieve automation; valve based on-chip pump systems generally utilise peristaltic principles to achieve this.[35] With the availability of the previously described gate valves, it is possible to also consider a pneumatically driven diaphragm pump for fluid actuation with active control of gate valves around this diaphragm, to control the direction of fluid flow. The on-chip pump consists of a symmetrical chamber structure with two inlets, two outlets, and a flexible diaphragm, illustrated in Fig. 2C while utilisation of a dedicated membrane, using an 800 μm square actuation chamber, provides propulsion. The desired inlet is initially opened, and the diaphragm is lifted, increasing the volume of the pump chamber and drawing fluid from the inlet; the inlet is then closed, the desired outlet opened, and the diaphragm is forced closed, distending into the pump chamber and reducing its volume, forcing the contained fluid through the open outlet.

Valve assemblies are positioned as close as possible to the pump structure, so as to reduce fluidic volume of the connecting channel, minimising required reagent volume and assay times. Due to the paired actuation of the valve assemblies, diffusion of fluids across open valve gates can contaminate the fluid within the unused assembly. To avoid this and ensure pure sample or reagent delivery to the sensor surface, it is necessary to purge the volume of the assembly to waste when switching between ports on opposite assemblies. This, as well as priming of all fluidic lines, is done through the waste channel output of the pump.

Microfluidic fabrication

Fabrication of the microfluidic modules was accomplished utilising a combination of the 'membrane sandwich' approach,[36] and a novel PDMS Injection moulding technique, previously described by our group.[28] In brief, complementary

mould structures are fabricated using standard photolithography techniques or 3D printing. All fluidic channel structures to be in contact with the sensor surface are patterned onto a bottom mould, while all actuation channels and *via* or interconnecting channels are patterned onto a complementary top mould. Polydimethylsiloxane (PDMS) pre-polymer (Sylgard 184 Silicone Elastomer – Dow Corning) is mixed with curing agent with a weight ratio of 10 : 1 respectively, and thoroughly degassed under vacuum. Degassed pre-polymer composite is then introduced between aligned complementary mould structures. The assembled mould structure is then placed into an oven for 1 hour at 80 °C, when cured, the mould structures are separated and the PDMS slab (shown in Fig. 2A) is extracted. A blank PDMS interface slab of approximately 4–5 mm thickness is then biopsy punched with appropriately aligned pneumatic interface holes (0.75 mm) and on-chip fluidic reservoirs (4–6 mm). The actuation side of the injection moulded PDMS slab is irreversibly plasma bonded to the interface slab; this assembled PDMS module can then be aligned over the sensor surface of the BiMW sensor and reversibly bonded. A thin (250–500 μm) PDMS cap can then be placed over the top of the module, this layer has cut-outs

allowing access for pneumatic interface tubing, it is reversibly bonded and prevents evaporation of fluid from the on-chip reservoirs. The thin evaporation preventative layer can easily be lifted at the edge of the assembly to allow access to the on-chip reservoirs; small perforations can be made with a hypodermic needle in the areas centred on these reservoirs, these perforations will seal due to the elastomeric nature of the PDMS as long as the PDMS is flat, however they allow gas transfer when a pressure differential is applied, equilibrating pressure within the reservoirs. Finally, the assembled module is clamped using screws between a polymethyl methacrylate (PMMA) clamp layer and the BiMW setup outlined in ref. 4. The physically realised PDMS device is presented in Fig. 3.

Microfluidic subsystem characterisation

To verify functionality of the microfluidic control systems, each of the components was initially verified independently. Fig. 3A and B shows these subsystems in operation with food dyes verifying fluidic isolation, while the final integrated configuration is shown in Fig. 3C. Low resolution microscopy of the entire module in operation with food dyes illustrates the
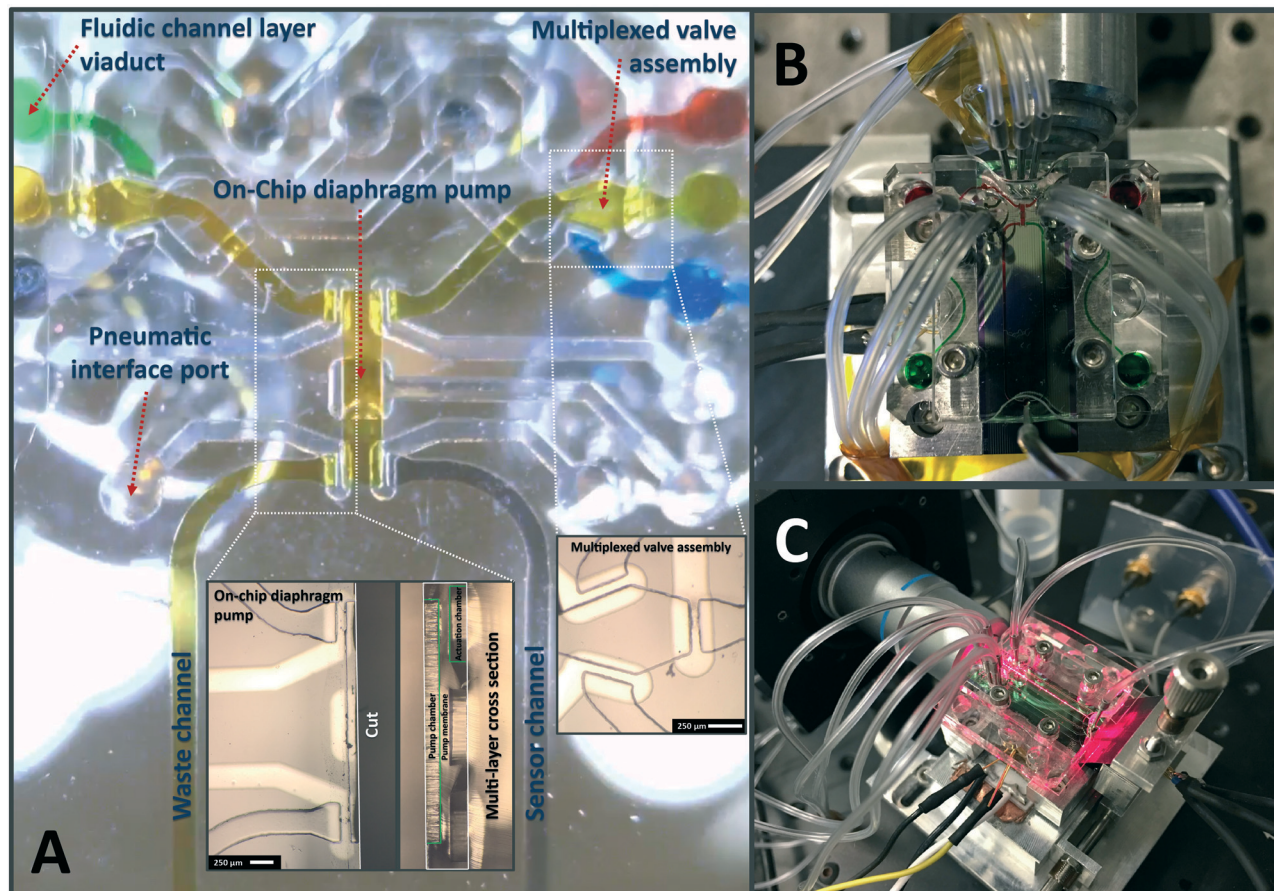
Fig. 3 Imaging of the microfluidic subsystems. Fig. 3A shows a low-resolution microscopy image of the area illustrated in Fig. 2C imaged in operation with color dyes while bonded to a glass slide. Control components are labeled, with high resolution images of the multiplexing valve assembly and pump inset including cross sectional cut of the pump structure. Fig. 3B shows integration of the microfluidic module with the BiMW sensor, with channels highlighted with color dyes, while Fig. 3C shows an operational image of the module integrated with an active BiMW sensor.

functionality of the multiplexing valve assemblies and pump in Fig. 3A, where the running buffer is represented with yellow dye in central reservoirs, while other colours represent reagent and sample fluids, respectively. Supplementary Video-1† demonstrates operation of the on-chip pump with food dyes purged through the waste channel. Inset within Fig. 3A includes higher resolution images of the pump and multiplexing assembly structures, as well as a cross-sectional cut of the pump structure, showing relative thickness of the valve structural layers. This dissected valve geometry is explored in further detail in Supplementary Fig. S-1.† Fig. 3B shows the microfluidic module aligned and reversibly bonded with a BiMW sensor chip, assessing valve functionality and verifying fluidic isolation. 3C shows the module integrated with an active BiMW photonic sensor while in operation. The on-chip diaphragm pump was experimentally demonstrated to achieve stable flow rates up to approximately 7.5 μL min⁻¹. During Automated experimental protocols flow rates of 1.5 μL min⁻¹ and 6 μL min⁻¹ were used for sample flow and waste purging operations respectively.

Biosensing proof-of-concept

In order to assess the functionality of the microfluidic module interfaced with the BiMW sensor, we have employed fluidic automation in the context of a complex competitive biosensing assay requiring repetitive reference and competitive analysis cycles.

As a proof-of-concept we demonstrate the detection of the antibiotic tetracycline. Tetracycline is one of the most widely used antibiotics, exhibiting a broad spectrum of antimicrobial activity against a variety of disease-producing bacteria. Antibiotics are used extensively in human and veterinary medicine, and also in aquaculture, in order to prevent or treat microbial infections. Antibiotic residues from different sources (household, pharmaceutical industry, and hospital) enter into municipal sewage but they are only partially eliminated at sewage treatment plants and as consequence, residues of these drugs and their metabolites are released into the environment. The uncontrolled exposure to antibiotic residues increases the appearance of antibiotic-resistant bacteria, which represents a serious and growing human health threat worldwide, because infections from resistant bacteria are increasingly difficult and expensive to treat. Therefore, due to its widespread use, monitoring of tetracycline levels is important in numerous fields such as clinical diagnosis,[37] food processing,[38] and environmental pollutant monitoring.[10] Tetracycline has a low molecular weight (444.45) and is often found in low concentrations (110 pg mL⁻¹ in contaminated surface water and 400 pg mL⁻¹ in contaminated groundwater[39]), for these reasons competitive immunoassays are well suited for its detection. In a competitive immunoassay format the chemical target to be detected, present in a sample, competes for the antibody binding sites with a receptor previously attached to the sensor surface. The sample containing the chemical target to be detected is incubated for

a few minutes with a fixed quantity of the corresponding antibody and then flowed on to the sensor surface. The signal is obtained by the interaction of the remaining free antibody of the incubated solution (sample + antibody) with the receptor layer. Therefore, the signal is inversely proportional to the concentration of the chemical target in the sample. The bioreceptor layer is expected to be re-usable during various analysis cycles by regeneration of the sensor surface, i.e. by dissociating the receptor–antibody interaction without destroying the bioreceptor activity.

It should be possible to automate our developed integrated microfluidic–BiMW system to perform the complex and repetitive fluid handling required for the competitive assay in order to detect the presence of tetracycline. Automation of this integrated system should allow a significant increase in assay repeatability, while reducing manual labour as well as the influence of any associated manual error variables.

In these experiments we have employed a tetracycline conjugate (DoxAc10-AD) and an antiserum specific for the family of tetracycline-related antibiotics (As256). The suitability of this immuno-reagents pair was first tested by a standard Surface Plasmon Resonance (SPR) Biosensor (data not shown), achieving a LOD of 0.09 nM and an IC₅₀ value of 3.6 nM. The SPR sensor could be reused for several measure-regeneration cycles of tetracycline by using 10 mM NaOH solution as a regeneration buffer.

Surface biofunctionalisation and competitive immunoassay

A previous surface biofunctionalisation of the sensor surface is mandatory to perform the analysis. In this case we have employed a silanisation protocol with carboxyethylsilanetriol sodium salt (CTES) which provides a surface functionalized with carboxyl groups, allowing the further covalent immobilisation of bioreceptors presenting amino groups in their structure, such as the evaluated hapten–protein conjugate (DoxAc10-AD) by the well-known EDC/NHS chemistry. Briefly, the BiMW sensors were first thoroughly cleaned, oxidised (oxygen plasma treatment, 5 min) and immersed in an aqueous 0.5% CTES solution for 1 h. After that, the CTES-treated chips were rinse with deionised water, dried under nitrogen stream and thermally cured at 110 °C for 1 h. CTES silanisation is performed utilising previously optimised protocols by our Group.[5] The silanised chip is then aligned with the microfluidic module such that a BiMW sensing window is located within the sensor channel, and reversibly bonded. The assembled device is then placed into the experimental setup and connected to the valve driver support equipment (for further information see: Supplementary Material SM-1:† Experimental setup). Further surface functionalisation steps are performed utilising the automated microfluidic module, at a flow rate of 1.5 μL min⁻¹, an automated on-chip fluid handling protocol is executed with minimal user input, thereby reducing user introduced variability and resulting in more reproducible surface conditions. Due to the reactive and time critical nature of functionalisation reagents, it is necessary to prepare and load reagents sequentially into on-chip reservoirs as they are

required. MilliQ DI water is used as a running buffer for the following process: initially, the reactive carboxylic groups of the silanised sensor surface are activated by flowing 200 mM EDC/50 mM sulfo-NHS solution in 100 mM MES buffer containing 0.5 M NaCl, at pH 5.0 for 10 minutes. The surface is briefly cleansed with DI water, followed by flow of the receptor molecule (DoxAc10-AD) at a concentration of 20 μg mL^{-1} in SA buffer (pH 5) allowing bonding with the freshly activated surface for 15 minutes. An additional DI water rinse is followed by a final flow of ethanolamine 1 M (pH 8.5), to deactivate residual carboxylic groups and to remove electrostatically bound ligand in an effort to avoid non-specific adsorptions. At this stage the sensor assembly is ready for the competitive assay. In a competitive immunoassay different steps are involved. Initially, the sensor surface needs to be conditioned with a buffer solution, until reaching a stable baseline signal. Then, the sample is mixed with a constant concentration of the antibody and the mixture is injected onto the sensor surface, allowing the interaction between the free antibody and the receptor immobilised onto the surface. The sensor surface is then washed with buffer to remove all unbound material and the signal after stabilisation is evaluated. Finally, the surface is regenerated and conditioned again with buffer, starting a new measurement cycle.

The surface functionalisation protocol and the competitive immunoassay employed are briefly introduced in Fig. 4. Fig. 4A illustrates the sensor surface in its initial state, 4B–D illustrate the technique used to immobilise the receptor (DoxAc10-AD) described above. Fig. 4E illustrates a functionalised surface in which the receptor molecule has captured the specific anti-

body; following this Fig. 4F shows the target–antibody interactions blocking antibodies from surface interaction.

Automated assay protocol

In order to perform a competitive immunoassay, the automated system must be able to perform an initial reference assay in order to benchmark sensor response to a known antibody concentration, followed by a competitive assay which will be used to quantify the target concentration. This 'cycle' of reference and competitive assays are complementary and must be repeated for each competitive assay. Each assay requires an initial flow of buffer solution in order to achieve a sensor baseline; this is followed by a sample flow, allowing surface interaction, likewise followed by a secondary flow of buffer as a sample washout step. The secondary baseline attained at washout can then be compared with initial baseline magnitude to interpret the effect of surface interaction. The sensor surface finally requires regeneration by actively stripping the bound antibodies using a mild acid or basic conditions, and a final buffer flow applied to bring the system back to a ready state. Automation of these assay protocols, implemented using the microfluidic module developed in this work, should result in time consistent cycling of the required steps of the complex assay, reducing interaction time variability and ensuring pure sample and reagent delivery. In order to achieve this, 20 minute detection cycles are programmed using Python script, automating all fluid handling required to perform an assay and subsequent surface
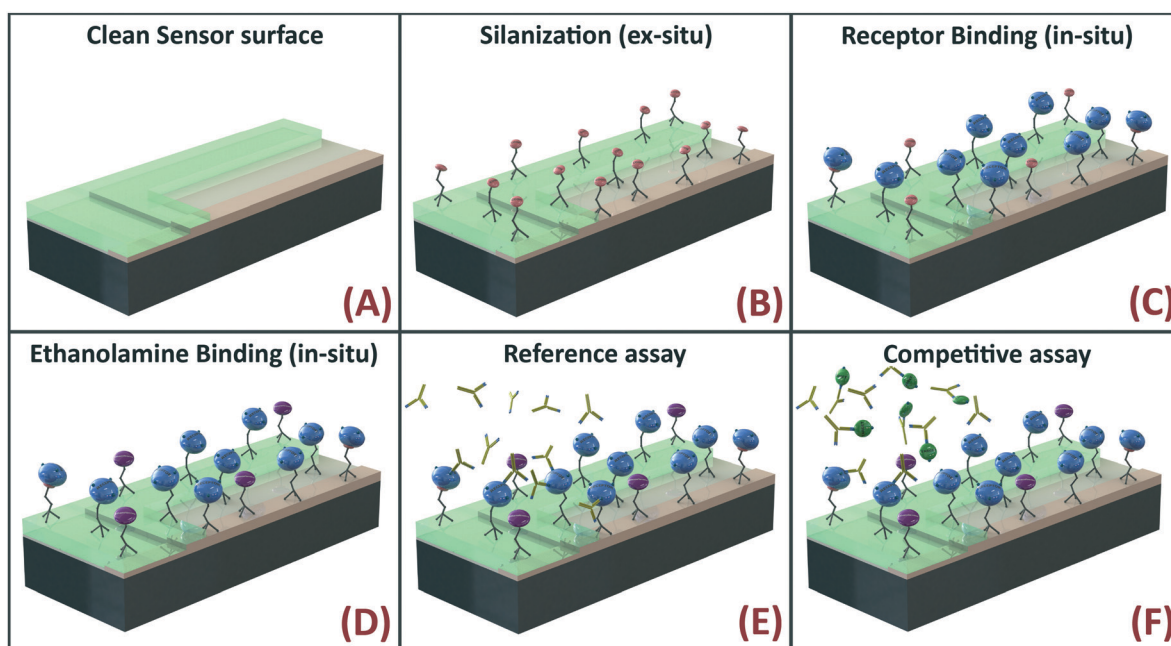
Fig. 4 Conceptually illustrated surface conditions during surface biofunctionalisation and during a competitive assay. Fig. 4A shows a clean sensor surface prior to functionalisation, this image represents a cross section of the BiMW, showing the waveguide surface (foreground) at the sensor window area with the passivation layer seen in green. Fig. 4B illustrates the sensor surface post silanisation with CTES, C illustrates receptor binding, followed by ethanolamine treatment in D, blocking any unbound carboxylic groups. Fig. 4E illustrates surface interactions during a reference assay, with antibodies binding to the receptor molecules, while F illustrates a competitive assay, antibody binding sites are occupied by target molecules reducing overall surface interaction.

regeneration using the BiMW sensor, with the exception of sample preparation. Initially running buffer, phosphate buffered saline (PBS) and regeneration fluid (NaOH-10 mM), are loaded into the on-chip reservoirs. An automated protocol then primes these channels, sending a small volume through the waste outlet, ensuring any bubbles are purged from the system and ensuring reagents are ready at the valve gate when required. Following initial priming, sample can be loaded and the automated sequence initiated, this sequence will initially flush sample through the waste path, cleansing the system and ensuring that sample delivered to the sensor is bubble and contaminant free; the sample is then directed through the sensor channel for 10 minutes passing a total sample volume of approximately 15 μL, during which time specific target binding can occur. Following this surface interaction period, the system flows PBS over the sensor for 4 minutes to flush out any unbound sample and to obtain a secondary baseline, this is followed by a 3 minute regeneration cycle where NaOH is directed over the sensor surface, stripping bound antibodies and readying the system for subsequent detection cycles; finally, the sensor surface is washed out with PBS for an additional 3 minutes returning the system to a ready state for subsequent measurements.

This automated protocol performs the assay fluid handling consistently, ensuring that flow conditions and interaction times are consistent for each assay. This was initially verified through manipulation of colour food dyes in place of sample and reagent fluids, as shown in Fig. 3C, prior to the assay application.

Biosensing of tetracycline antibiotic

Application of the automated assay protocol to perform fluid handling required for the competitive assay should allow repeated reproducible assay cycles, allowing target biomarker quantification, and evaluation of surface chemistry and its effectiveness following multiple regeneration cycles. Prior to experimentation, the sensor was initially biofunctionalised, reagents loaded into on-chip reservoirs and channels primed using an automated priming protocol. Then, the response of the sensor was evaluated by using the automated assay protocol.

As proof of concept, two different samples were analysed: PBS (sample free of antibiotic, used as a reference sample) and a 2 nM tetracycline solution in PBS. First, the sample was mixed with the antibody (AS-256) to a final concentration of 1 μg mL^{-1}. Then, 15 μL of the sample–antibody mixture was passed over the sensor over 10 minutes. During this step, the free antibodies interact with the receptor immobilized onto the sensor surface. It is expected that the presence of tetracycline in the sample will result in a lower interaction signal than the reference (competitive assay). During these experiments, the reference assay (sample free of tetracycline) was repeated before each competitive assay (2 nM tetracycline sample), in an attempt to compensate for degradation of the sensor surface occurring as a result of repeated surface regeneration.

Fig. 5 shows the sensor response for a sample free of tetracycline (reference assay) and a sample containing tetracycline in a concentration of 2 nM (competitive assay), sequentially analysed. Fig. 5A shows sensor readings during an example 20 minute automated measurement cycle running a target-free reference sample, with inset (1–4) conceptually illustrating interactions occurring on the surface of the sensor at various times during the cycle. The reference sample is mixed with the antibody and pipetted into the appropriate reservoir and the automated detection cycle is initiated. Fig. 5B (1–4) highlights the fluidic path taken from associated reservoirs at time points corresponding to 5A and 5C. Initially the sensor is immersed in PBS at a constant flow-rate of 1.5 μL min^{-1}; this is allowed to form a stable baseline, (1) before introduction of the sample. Initially, introduction of the sample causes a sharp change in signal due to a bulk change in the refractive index of the spiked sample, this is followed by a fixed surface interaction period in which antibodies present in the sample bind to the immobilised receptor, gradually modifying refractive index at the sensor surface, which can be seen as a gradual change in the signal and is conceptually illustrated in (2). Sample washout can be seen as a sharp change, corresponding in magnitude to that observed at sample inflow, this is due to the refractive index of the fluid returning to that of the running buffer or PBS, forming a secondary baseline, shown conceptually in (3). Finally, the surface of the sensor is stripped of bound antibodies using a regeneration solution (NaOH,10 mM), this surface regeneration step (4) prepares the sensor surface for subsequent detection cycles, following a return to running buffer (PBS) and a return to the initial baseline (1).

Surface interactions are quantified by assessing the phase variation of the BiMW interferometer, taking into account that a complete oscillation or fringe corresponds to a 2π rad phase variation. The arbitrary sensor signal (%) value, shown in Fig. 5A and C is tracked from the initial baseline time point in 5A (1) to the secondary baseline at time point 5A (3), taking any transitions across the fringe into account and subtracting the bulk refractive index peak. The total distance travelled represents the magnitude of the surface interaction signal, and are shown relative to π inset in Fig. 5A and C.

Fig. 5C displays sensor readings obtained during a competitive assay performed immediately following the reference, along with corresponding conceptual representations of surface interactions in insets of Fig. 5C (1–4). The competitive assay is performed using the same automated protocol as the reference; however the introduced sample contains 2 nM of tetracycline. It can be noted that the resultant increase in bulk refractive index due to additional components present in the sample has increased the magnitude of the spike observed at sample introduction and washout. It can be seen that the gradient of the surface interaction shown in area (2), is reduced when compared with the reference sample. It is also clear that the sensor response (overall magnitude of surface interaction, inset in 5A and C) is reduced in the competitive assay due to the presence of the target molecules (tetracycline) in the sample, occupying
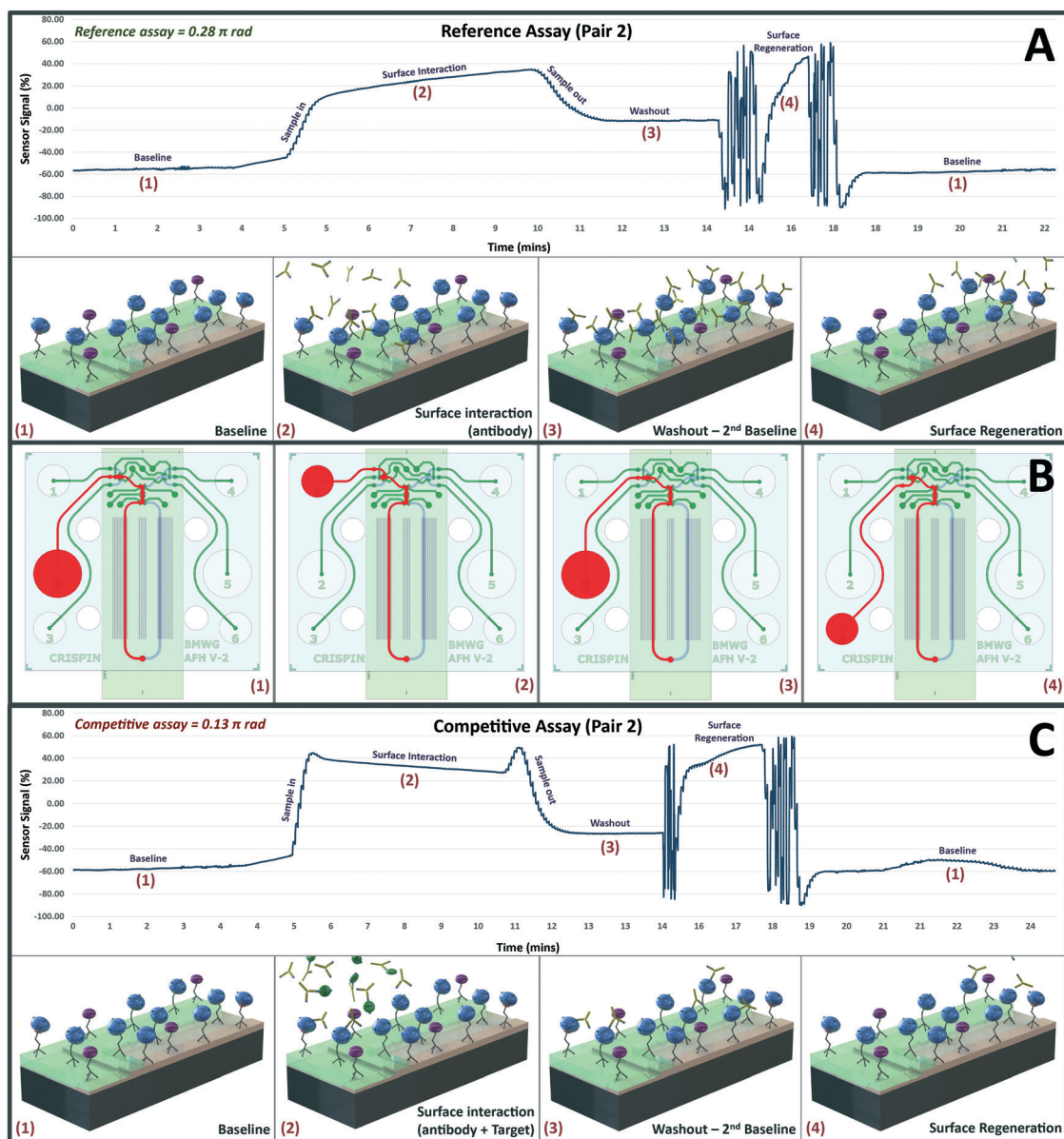
Fig. 5 Illustration of the surface interactions occurring at various time points during a reference and competitive assay pair, performed sequentially. Fig. 5A shows real–time sensor data during an example reference assay, with inset (1–4) conceptually illustrating interactions occurring on the sensor surface at critical time points during the cycle. Fig. 5B (1–4) highlights the fluidic path taken from the corresponding reservoir at the same time points during the assay, while Fig. 5C displays sensor readings obtained in a competitive assay performed immediately following the reference assay, along with corresponding conceptual representations of surface interactions in inset Fig. 5C (1–4).

the binding sites of the antibody, thereby reducing the quantity of available antibodies capable of binding to the receptor in the surface by an amount proportional to the target concentration. Fig. 6A overlays the response of a 2 nM tetracycline sample (competitive assay) and its corresponding reference. As it can be seen, the presence of 2 nM tetracycline leads to sensor response of 0.13π rad comparing to 0.28π rad for a sample free of antibiotic (reference), *i.e.* the presence of tetracycline lead to a 54% inhibition of the sensor response. The response of the competitive assay can be expressed as a percentage of its corresponding reference assay, this is shown in the inset in Fig. 6A, which corresponds to cycle 2 in Fig. 6B.

In order to assess the stability of the proof-of-concept surface functionalisation, repetitive reference and competitive cycles were performed, with target and antibody concentrations maintained at constant levels for each repetition. Fig. 6B illustrates the results, with reference cycles shown in green and competitive assays shown in red. Raw sensor data for each assay is shown in Supplementary Fig. S-2.†

As can be observed in Fig. 6B, the sensor response to reference assays in subsequent pairs reduces significantly. This is most noticeable between the first two assay pairs, and is presumably due to degradation of the immobilized receptor during the regeneration step. As the presence of target analyte is
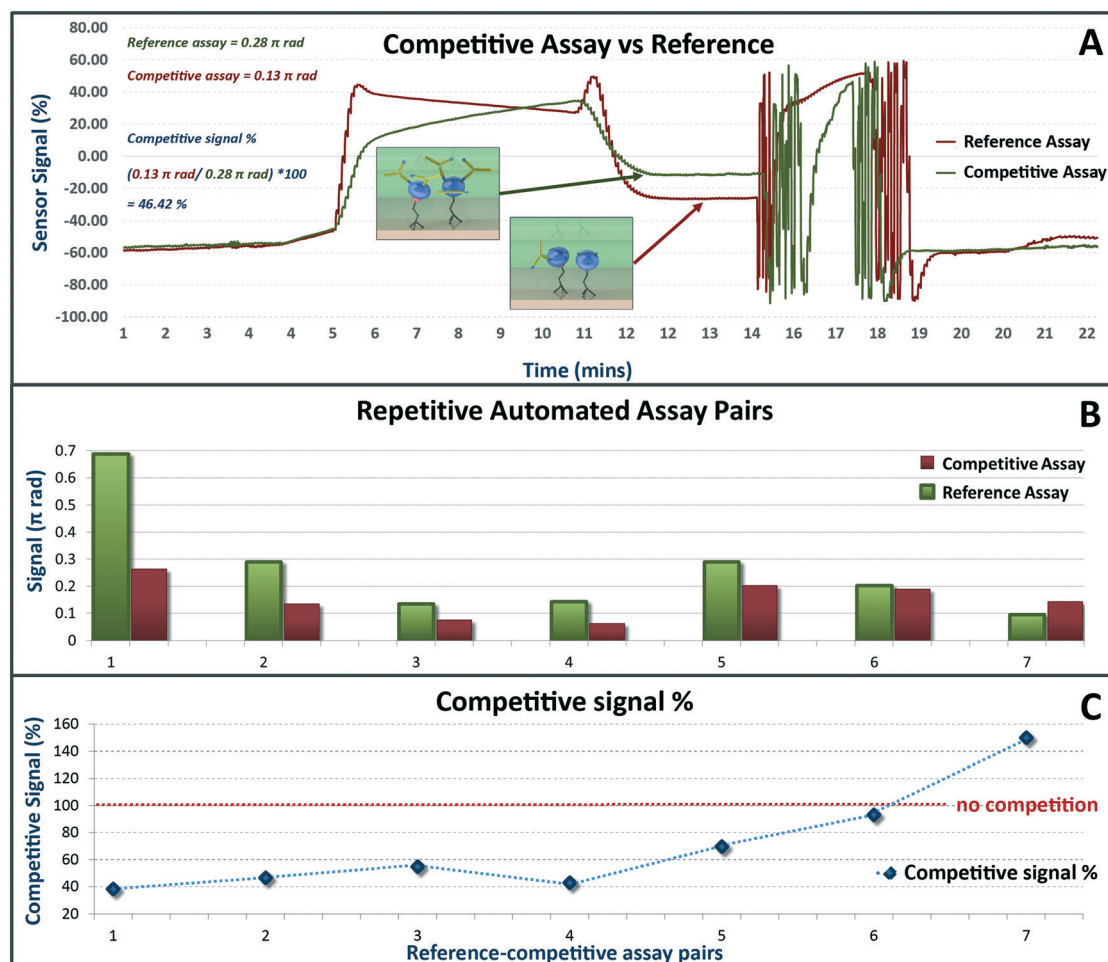
Fig. 6 Signal interpretation and performance of the proof-of-concept functionalized surface during repetitive regeneration cycles with fixed sample concentrations. Fig. 6A shows superimposed reference and competitive assay. The presence of tetracycline in the sample leads to an inhibition of the sensor response. Fig. 6B shows the sensor response for 14 sequential measurement-regeneration cycles, alternating reference sample (free of antibiotic) and spiked sample (2 nM tetracycline). Fig. 6C shows normalised results with each competitive assay as a percentage of its corresponding reference cycle.

detected as response inhibition, this sensor degradation can introduce a false positive result. For this reason, in order to dynamically compensate for surface degradation and increase the lifetime of the biosensor, each competitive assay was directly preceded by a reference assay. This could be avoided in future work by optimizing the sensor surface functionalisation procedure (receptor immobilization) and regeneration step. Each assay pair was normalized through comparison of the competitive result with its corresponding reference as a percentage, and the competitive signal in % shown in Fig. 6C.

It can be observed that the response of the sensor to the presence of tetracycline is comparatively stable, with signals (sample/reference ratio) at between 40–50% for the initial 4 assay pairs, this indicates relative surface stability for 8 measurement-regeneration cycles, with similar stability seen in repeated assays (data not shown). After 8 analysis a clear sensor degradation is observed, due to the repeated exposure of the bioreceptors to the regeneration solution (basic media). The increase in the competitive signal is presumably due to the

increase in non-specific binding events occurring as surface degradation results in the biolayer becoming less specific.

This biolayer lifetime is consistent with our previous results,[30] however it is presumable that improvements to the surface functionalisation protocol used in this proof-of-concept work could significantly improve surface integrity. In addition, in order to analyse real clinical or environmental samples, a more complete development of the biolayer will be required, adding antifouling properties to prevent non-specific binding in complex real samples, as we have demonstrated in previous publications of the BiMW interferometric biosensor.[7,30,32]

Conclusion

This work demonstrates a proof-of-concept implementation of an automated fluid handling module for photonic biosensors. The module is fabricated utilising a one-step injection moulding technique which significantly reduces fabrication

complexity of normally closed on-chip elastomer valves. This work makes use of the fabrication technique to realise on-chip fluid handling architecture required for operation of a highly sensitive bimodal waveguide photonic biosensor, automating complex fluid handling protocols required for the operation of a competitive immunoassay.

The capacity of the automated system is demonstrated in a proof of concept competitive immunoassay for the detection of the common antibiotic tetracycline. The system is shown to perform repetitive automated assay cycles, allowing a high degree of experimental control and temporal resolution. The system demonstrates multiple reference and competitive assay cycles, regenerating the sensor bioreceptor later between assays, as would be necessary in real applications requiring periodic testing, such as in food quality control or environmental monitoring.

This research represents a significant advancement in development of practical point-of-care photonic biosensors, providing complex automated fluid handling capabilities compatible with simple and scalable fabrication and robust integration. This research is intended to reduce the cost and effort required for the fabrication of complex lab-on-a-chip platforms, while increasing the level of functional integration, making application of these intricate devices across a broad range of research fields more practical. In addition, a sufficient reduction in fabrication complexity is intended to enable a higher level of fluidic control sophistication in point-of-care medical diagnostic devices, allowing use of more complex biosensors. This research could potentially be integrated into commercial large scale fabrication of point-of-care devices.

The automated nature of this system makes it suited to performing repetitive assay cycles which could be used to sweep parameters in order to optimise surface chemistry.

Future work will include optimising the biolayer and regeneration protocol, with the intention of providing more stable biosensors and increasing sensor lifetime. Further future work toward increasing performance when analysing low concentration targets is planned, including surface passivation similar to the approaches explored in,[40] intended to minimise loss of low concentration target molecules through non-specific adsorption in the PDMS module. Further expansion of the system is intended to allow for multiplexing of multiple biosensors, as well as the addition of sample preparation subsystems (if required), providing additional functionality critical to point-of-care applications. In addition, we intend to exploit the scalability of the fabrication technique used in this work through investigation of other biocompatible elastomer materials compatible with injection moulding, facilitating mass production.

Conflicts of interest

There are no conflicts to declare.

Acknowledgements

References

1 M.-C. Estevez, M. Alvarez and L. M. Lechuga, *Laser Photonics Rev.*, 2012, **6**(4), 463–487.

2 A. Fernández Gavela, D. Grajales García, J. C. Ramirez and L. M. Lechuga, *Sensors*, 2016, **16**(3), 285.

3 J. E. Baker, R. Sriram and B. L. Miller, *Lab Chip*, 2017, **17**(9), 1570–1577.

4 K. E. Zinoviev, A. B. González-Guerrero, C. Domínguez and L. M. Lechuga, *J. Lightwave Technol.*, 2011, **29**(13), 1926–1930.

5 A. B. González-Guerrero, M. Alvarez, A. G. Castaño, C. Domínguez and L. M. Lechuga, *J. Colloid Interface Sci.*, 2013, **393**, 402–410.

6 J.-H. Han, H.-J. Kim, L. Sudheendra, S. J. Gee, B. D. Hammock and I. M. Kennedy, *Anal. Chem.*, 2013, **85**(6), 3104–3109.

7 C. S. Huertas, D. Fariña and L. M. Lechuga, *ACS Sens.*, 2016, **1**(6), 748–756.

8 W. Jung, J. Han, J.-W. Choi and C. H. Ahn, *Microelectron. Eng.*, 2015, **132**, 46–57.

9 J. Adrian, S. Pasche, J.-M. Diserens, F. Sánchez-Baeza, H. Gao, M.-P. Marco and G. Voirin, *Biosens. Bioelectron.*, 2009, **24**(11), 3340–3346.

10 N. Kemper, *Ecol. Indic.*, 2008, **8**(1), 1–13.

11 B. Chocarro-Ruiz, A. Fernández-Gavela, S. Herranz and L. M. Lechuga, *Curr. Opin. Biotechnol.*, 2017, **45**, 175–183.

12 C. D. Chin, V. Linder and S. K. Sia, *Lab Chip*, 2012, **12**(12), 2118–2134.

13 V. Gubala, L. F. Harris, A. J. Ricco, M. X. Tan and D. E. Williams, *Anal. Chem.*, 2011, **84**(2), 487–515.

14 F. B. Myers and L. P. Lee, *Lab Chip*, 2008, **8**(12), 2015–2031.

15 A. K. Yetisen, M. S. Akram and C. R. Lowe, *Lab Chip*, 2013, **13**(12), 2210–2251.

16 K. Choi, A. H. Ng, R. Fobel and A. R. Wheeler, *Annu. Rev. Anal. Chem.*, 2012, **5**, 413–440.

17 S.-Y. Teh, R. Lin, L.-H. Hung and A. P. Lee, *Lab Chip*, 2008, **8**(2), 198–220.

18 J. Melin and S. R. Quake, *Annu. Rev. Biophys. Biomol. Struct.*, 2007, **36**, 213–231.

19 R. Gomez-Sjoeberg, A. A. Leyrat, D. M. Pirone, C. S. Chen and S. R. Quake, *Anal. Chem.*, 2007, **79**(22), 8557–8563.

20 L. M. Fidalgo and S. J. Maerkl, *Lab Chip*, 2011, **11**(9), 1612–1619.

21 Y. C. Yap, T. C. Dickson, A. E. King, M. C. Breadmore and R. M. Guijt, *Biomicrofluidics*, 2014, **8**(4), 044110.

22 J. Kim, E. C. Jensen, A. M. Stockton and R. A. Mathies, *Anal. Chem.*, 2013, **85**(16), 7682–7688.

23 J. Kim, A. M. Stockton, E. C. Jensen and R. A. Mathies, *Lab Chip*, 2016, **16**(5), 812–819.

24 H. Cai, J. Parks, T. Wall, M. Stott, A. Stambaugh, K. Alfson, A. Griffiths, R. Mathies, R. Carrion and J. Patterson, *Sci. Rep.*, 2014, **5**, 14494.

25 J. W. Parks, M. A. Olson, J. Kim, D. Ozcelik, H. Cai, R. Carrion Jr, J. Patterson, R. Mathies, A. Hawkins and H. Schmidt, *Biomicrofluidics*, 2014, **8**(5), 054111.

26 B. R. Schudel, C. J. Choi, B. T. Cunningham and P. J. Kenis, *Lab Chip*, 2009, **9**(12), 1676–1680.

27 C. Szydzik, A. F. Gavela, J. Roccisano, S. Herranz, A. Mitchell and L. M. Lechuga, presented at the *SPIE BioPhotonics Australasia*, 2016, (unpublished).

28 C. Szydzik, B. Niego, G. Dalzell, M. Knoerzer, F. Ball, W. Nesbitt, R. Medcalf, K. Khoshmanesh and A. Mitchell, *RSC Adv.*, 2016, **6**(91), 87988–87994.

29 C. S. Huertas, S. Domínguez-Zotes and L. M. Lechuga, *Sci. Rep.*, 2017, **7**, 41368.

30 J. Maldonado, A. B. González-Guerrero, C. Domínguez and L. M. Lechuga, *Biosens. Bioelectron.*, 2016, **85**, 310–316.

31 A. B. González-Guerrero, J. Maldonado, S. Dante, D. Grajales and L. M. Lechuga, *J. Biophotonics*, 2017, **10**(1), 61–67.

32 A. B. González-Guerrero, J. Maldonado, S. Dante, D. Grajales and L. M. Lechuga, *J. Biophotonics*, 2017, **10**(1), 61–67.

33 S. K. Sia and G. M. Whitesides, *Electrophoresis*, 2003, **24**(21), 3563–3576.

34 E. C. Jensen, A. M. Stockton, T. N. Chiesl, J. Kim, A. Bera and R. A. Mathies, *Lab Chip*, 2013, **13**(2), 288–296.

35 W. H. Grover, A. M. Skelley, C. N. Liu, E. T. Lagally and R. A. Mathies, *Sens. Actuators, B*, 2003, **89**(3), 315–323.

36 J. R. Anderson, D. T. Chiu, R. J. Jackman, O. Cherniavskaya, J. C. McDonald, H. Wu, S. H. Whitesides and G. M. Whitesides, *Anal. Chem.*, 2000, **72**(14), 3158–3164.

37 I. Chopra and M. Roberts, *Microbiol. Mol. Biol. Rev.*, 2001, **65**(2), 232–260.

38 C. Nebot, M. Guarddon, F. Seco, A. Iglesias, J. M. Miranda, C. M. Franco and A. Cepeda, *Food Control*, 2014, **46**, 495–501.

39 R. Daghrir and P. Drogui, *Environ. Chem. Lett.*, 2013, **11**(3), 209–227.

40 H. Zhang and M. Chiao, *J. Med. Biol. Eng.*, 2015, **35**(2), 143–155.

3.2 – Label-Free Optofluidic Nanobiosensor Enables Real-Time Analysis of Single-Cell Cytokine Secretion

The paper of the previous section focussed on complex microfluidic systems designed to facilitate controlled flow and fluidic isolation of various liquid reagents with respect to an underlying photonic waveguide-based biosensor. This sensor operated with the reagents and then the analyte flowed over the sensing region during operation. There are however, biosensing applications where flow cannot be permitted, where for example a target is required to be captured and an assay performed under static and carefully controlled environmental conditions.

Single cell analysis has shown significant promise in recent years, allowing insight into the heterogeneity of various cellular characteristics and response to stimulus, with impact across a broad range of fields [47]. Analysis of the secretions of cellular messaging biomarkers, cytokines, is one such field, with significant potential in unravelling the mechanism of intercellular interactions under various conditions.

Several challenges exist in maintaining viable cells held isolated in nanolitre scale volumes for long duration cytokine secretion analysis. Of primary concern, fluidic isolation of the captured cell is necessary to maintain the concentration of secreted biomarkers, however the water content of isolated cell culture media can evaporate over time, changing the concentration of dissolved components and thus the bulk refractive index, and eventually leading to bubble formation within the system. Plasmonic nanohole array biosensors are sensitive label free planar biosensors that can provide spatial information on binding of target biomarkers. For this reason, Plasmonic nanohole array biosensors are well suited to single cell cytokine detection, allowing observation of the spread of target biomarkers from captured cells. These sensors however, are highly sensitive to bulk changes in refractive index of the media in which they are sensing, leading to sensor noise or false positives, while any bubbles forming in the system are likely to disrupt the sensor.

While various strategies for controlling gas concentrations have been applied to cell culture platforms [48], these systems generally don't consider vapour transfer within microfluidic systems,

or the resulting impact on media refractive index, and such systems have not been applied to systems utilising active biosensing elements.

In the paper of this section, I have developed a microfluidic system consisting of active microvalve components, capable of isolating a small volume of fluid around a single cell of interest. The system also utilises a regulatory subsystem, which actively maintains the vapor pressure within this isolated volume, preventing the minute volume from evaporating, and stabilising the fluidic environment around the cell of interest. Microfluidics are fabricated using the injection moulding fabrication technique developed in Chapter 2, allowing the fabrication of complex 3-dimensional microfluidic components, including active fluid handling components and passive permeable membranes, without additional fabrication complexity.

This work was the result of a collaborative project with the Bionanophotonics Systems Laboratory group at EPFL in Lausanne, the system was designed to facilitate robust operation for long duration single cell analysis using the plasmonic nanohole array biosensors developed by this group.

This work Demonstrates that the fabrication method outlined in chapter 2 is practical and well suited to the fabrication of complex multilayer microfluidic devices, containing multiple active control elements as well as vapour permeable membranes which are particularly important where small volumes of fluid must be isolated for long durations.

The work related to this chapter has been peer-reviewed and published in: *Small*

This paper was identified as a 'hot topic' by the publisher, with a front cover and video abstract as seen in the links below:

The paper can be obtained via the DOI: **https://doi.org/10.1002/smll.201800698 [31]**

The front cover can be obtained via the DOI: **https://doi.org/10.1002/smll.201870119 [49]**

The video abstract can be seen here: **https://www.youtube.com/watch?v=sDjux6M0evw**

My role in this work was related primarily to the microfluidic component, conceiving the valved single cell capture and environmental control components of the system. I was involved in data analysis, the formulation of hypothesis based on the effects of the microfluidic environment on the biosensor response, and diagnosis of these issues based on biosensor response. I designed systems intended to stabilise the biosensor based on these hypothesis, and fabrication of these microfluidic systems. I assisted with calculations assessing stability of the microfluidic environment, put together several figures for the manuscript and assisted with writing the manuscript, focussing on the microfluidic component. As the emphasis of the paper was on biomedical application, the two lead authors were the EPFL post-docs who actually conducted the single cell analysis, I was the next author as lead platform researcher.
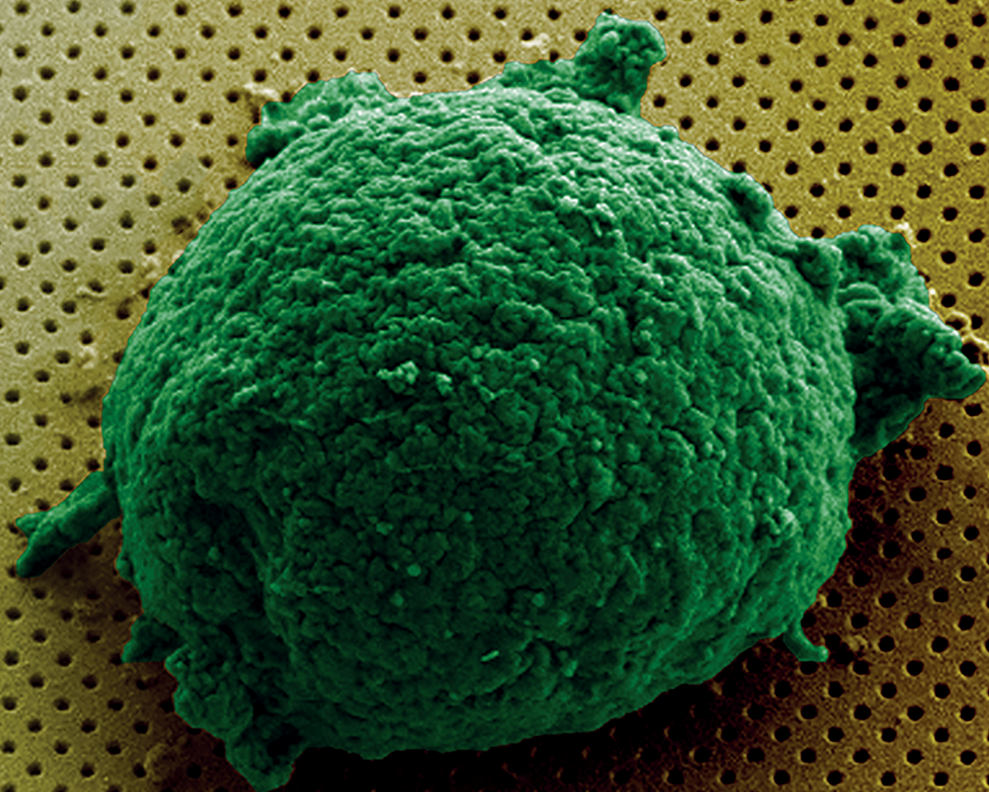
NANO · MICRO

small

Label-Free Optofluidic Nanobiosensor Enables Real-Time Analysis of Single-Cell Cytokine Secretion

Xiaokang Li, Maria Soler, Crispin Szydzik, Khashayar Khoshmanesh, Julien Schmidt, George Coukos, Arnan Mitchell, and Hatice Altug*

Single-cell analysis of cytokine secretion is essential to understand the heterogeneity of cellular functionalities and develop novel therapies for multiple diseases. Unraveling the dynamic secretion process at single-cell resolution reveals the real-time functional status of individual cells. Fluorescent and colorimetric-based methodologies require tedious molecular labeling that brings inevitable interferences with cell integrity and compromises the temporal resolution. An innovative label-free optofluidic nanoplasmonic biosensor is introduced for single-cell analysis in real time. The nanobiosensor incorporates a novel design of a multifunctional microfluidic system with small volume microchamber and regulation channels for reliable monitoring of cytokine secretion from individual cells for hours. Different interleukin-2 secretion profiles are detected and distinguished from single lymphoma cells. The sensor configuration combined with optical spectroscopic imaging further allows us to determine the spatial single-cell secretion fingerprints in real time. This new biosensor system is anticipated to be a powerful tool to characterize single-cell signaling for basic and clinical research.

1. Introduction

Single-cell analysis is one of the most powerful approaches toward the development of new therapies for serious diseases such as cancer or autoimmune disorders.[1] The recent implementation of advanced analysis technologies (e.g., next-generation sequencing) has boosted our knowledge and understanding of the complex heterogeneity in cellular genomics,

epigenomics, and transcriptomics.[2] However, the analysis of individual cell secretion is essential to fully understand the functional heterogeneity and decipher the underlying mechanisms of cellular interactions and communication. Intercellular signaling and formation of cellular networks is a highly dynamic process mediated by the expression and secretion of small proteins (e.g., cytokines) and other molecules, which identify the particular cell activities, behaviors, and functions.[3,4] The sensitive monitoring and analysis of cell secretion provide invaluable information of the specific functionality and real-time activity of individual cells in either physiological or pathological process. Such dynamic and accurate analysis is still an unresolved challenge. Traditional secretion analysis techniques include enzyme-linked immunosorbent assay (ELISA) or immunofluorescence staining; however, these methods lack sufficient sensitivity for detection of single-cell secretions.[5]

The past few years have seen the advances of innovative strategies for both cell isolation and protein secretion analysis to enable single-cell resolution.[6–9] For instance, Love et al. introduced a large-scale microengraved array which is able to generate the populational secretion profiles from single hybridoma cells,[6] or even to characterize the cytokine secretion of single T lymphocytes upon different activation scenarios.[9] While their methods are efficient enough to provide a high-throughput dataset, the intensive washing steps involved in the fluorescence labeling procedure dramatically impairs the temporal resolution (limited to a few hours) of the analysis. On the other hand, droplet microfluidics has been presented as a promising platform for single-cell sorting and analysis.[10–12] The technique basically involves encapsulating individual cells in droplets loaded with specific fluorescent antibodies or enzymes for capturing and detecting the secreted cytokines. However, subsequent cytokine quantification requires external readout means, such as flow cytometry or spectroscopic methods that increase the overall system complexity and only provide an end-point result. Despite the capabilities of these new techniques for single-cell isolation, the need of either fluorescent or enzymatic labels for detection significantly impairs the dynamic analysis and monitoring of the secretion in real time.

X. Li, Dr. M. Soler, Prof. H. Altug
Institute of Bioengineering
École Polytechnique Fédérale de Lausanne (EPFL)
CH-1015 Lausanne, Switzerland
E-mail: hatice.altug@epfl.ch
C. Szydzik, Dr. K. Khoshmanesh, Prof. A. Mitchell
School of Engineering
RMIT University
Melbourne 3001, Australia
Dr. J. Schmidt, Prof. G. Coukos
Ludwig Institute for Cancer Research
University of Lausanne and Department of Oncology
University of Lausanne
CH-1007 Lausanne, Switzerland

ADVANCED
SCIENCE NEWS
www.advancedsciencenews.com

NANO · MICRO
small
www.small-journal.com

Label-free biosensors emerge as a unique solution for the sensitive, accurate and real-time analysis of cell secretion.[13–15] This detection scheme circumvents the tedious and costly molecular tagging and enables the elucidation of biomolecular interactions in a noninvasive and dynamic manner. Among various label-free sensing platforms, optical biosensors are distinguished by their compatibility with physiological solutions, robust performance, and ability to perform quantitative detection.[16–20] The recent advances in nanotechnology have inspired the development of extraordinarily improved optical biosensors based on photonic nanostructures. Nanophotonics, by supporting strong light-matter interaction and dramatically confining light in small volumes, enables ultralow detection limits, exceptional miniaturization, and ultimate on-chip integration.[21] Particularly, plasmonic nanohole arrays (NHAs) have demonstrated a unique potential and flexibility for the implementation of powerful biosensors with high-throughput analyses and capabilities for point-of-care deployment and utilization.[22,23] Nanohole arrays can be manufactured with cost-efficient and straightforward techniques,[24] and they overcome the primary constraints of conventional surface plasmon resonance (SPR) devices, such as the light coupling requirements and the limited field of view for high-throughput assays.[25] Furthermore, gold NHA biosensors have demonstrated exceptional performance for the analyses of proteins and cells in a real-time and multiplexed label-free configuration.[24,26–28]

However, label-free photonic biosensors face critical challenges for addressing single-cell secretion analysis. Cytokines are relatively small molecules (MW 15–30 kDa) and are secreted in minute amounts (femtograms per cell per day). Therefore, the direct detection of single-cell secretion in real time without any signal amplification is not straightforward. In order to achieve the ultrahigh sensitivity required for the detection of cytokines secreted from an individual cell, it can be effective to minimize the local volume surrounding the cells by encapsulating them with microchambers. This will result in concentrated molecular distribution in the vicinity of the sensor surface. In this regard, microfluidics technology offers a powerful tool to create a highly miniaturized environment with compartmentalization for the analysis.[29] Nevertheless, the optical monitoring of an ultralow volume in cell culture conditions (i.e., 37 °C) introduces a significant evaporation problem. This is especially challenging when using polydimethylsiloxane (PDMS) as the material for microfluidics. This widely used material provides excellent transparency and high gas permeability, making it an ideal substrate for optical cellular bioassays.[30] However, the gas diffusion also leads to evaporation and associated optical noise when handling the ultralow volume of fluid.[31,32] Water evaporation through PDMS membranes may cause not only an increase in osmolality of the cell media but may also result in bubble formation and eventually dehydration of the cell chamber. These evaporation-mediated osmolality alterations induce local changes of the fluid refractive index, causing dramatic optical signal fluctuations that overwhelm the low magnitude secretion signature of single cells. Conventional approaches to prevent liquid evaporation, such as sealing the aqueous surface with mineral oil[31] or placing numerous sacrificial drops in the vicinity of the analyte chamber,[32] can be effective but increase overall system complexity, limit on-chip integration and pose potential contaminations to the assay. Conversely, thin PDMS membranes between culture areas and oxygen equilibrated water channels have been shown to reduce evaporation, while at the same time maintaining oxygen levels required for sustained culture.[33]

In this work, we introduce a new approach for the single-cell secretion analysis in real time using a label-free nanoplasmonic biosensor. We have developed an optofluidic device based on a gold nanohole array sensor integrated into an innovative multifunctional microfluidic system for the dynamic and accurate monitoring of cytokine secretion from individual cells (**Figure 1**a). The nanohole arrays covering the entire sensor surface are manufactured uniformly with low-cost and wafer-scale photolithography. For optical detection, we exploit a spectroscopic imaging method which converts each imaged point to an effective sensing element. We utilize the single step injection molding technique[34] to create a microfluidic system equipped with pneumatic valves that enables both the in-flow introduction of cells into the device and isolation of a microchamber
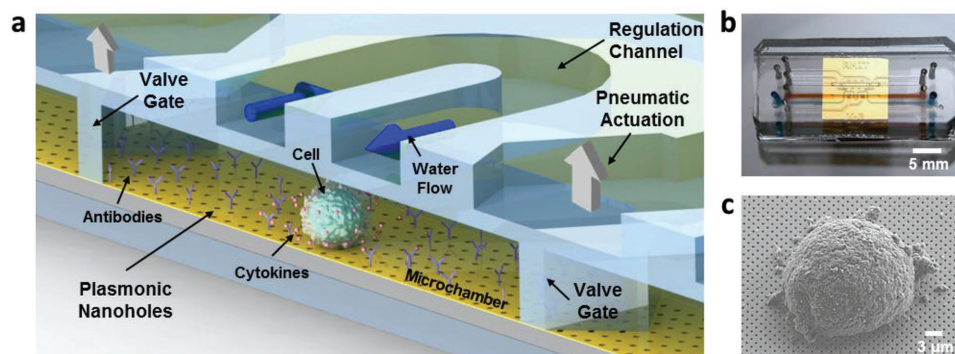
Figure 1. Illustration of the optofluidic system for real-time single cell analysis. a) Schematic representation of the microfluidic-integrated nanoplasmonic biosensor. The microfluidic system consists of two fundamental parts: a primary channel in contact with the plasmonic nanohole array chip, which includes two pneumatic valve gates for enclosing a small-volume microchamber for single-cell analysis, and a hydraulic regulation channel fabricated on top of the microchamber to provide humidity regulation through serpentine water flow. For analysis, the single cells attached to the plasmonic chip surface are surrounded by specific antibodies, which will capture the secreted cytokines postactivation. b) The picture of the integrated device. We highlight the primary channel (orange) and the regulation channel (blue) with flowing colored dyes, respectively. c) An SEM image of a single EL4 cell attached to the nanohole array chip.

**ADVANCED
SCIENCE NEWS**

www.advancedsciencenews.com

NANO · MICRO

small

www.small-journal.com

on the nanostructured sensor chip to confine and analyze individual cells. A valve-gated microchannel allows us to control the flow when introducing the cells that are then isolated within a low volume cell chamber, which maintains the cytokine concentration at a high level and improves the biodetection accuracy. Moreover, we harness the ability of our injection molding approach to create a continuous regulation channel that interacts with the underlying valve-isolated sub-microliter cell chamber through thin PDMS membranes (Figure 1a). The regulation flow simultaneously ameliorates evaporation, prevents bubble formation and enables a stable optical background signal for robust monitoring of single cell secretion analysis.

Our optofluidic device (Figure 1b) has been applied for the label-free detection of interleukin-2 (IL-2) from individual EL4 lymphoma cells (Figure 1c) in a real-time manner. The secretion dynamics can be monitored for a period spanning several hours, without any need to disturb the cell culture and label the secreted cytokine molecules, while keeping the appropriate temperature and humidity conditions for cell activity and viability. The temporal detection interval can be highly customized to ensure sufficient time resolution for the bioanalysis. Furthermore, due to the extended arrangement of NHAs over the entire chip surface, we have the flexibility to designate multiple detection areas around a single cell with varying distances apart, where the cytokine diffusion activity can be depicted spatially as well. This versatile

optofluidic biosensor provides a reliable and facile label-free detection platform to investigate the onset, dynamics, and diffusion of cytokine secretion activities at the single-cell level.

2. Results and Discussions

2.1. Optical Configuration of The NHA Biosensor

The plasmonic nanohole arrays offer highly sensitive label-free biosensing and are distinguished among other state-of-the-art plasmonic sensors due to the well-proven capabilities for device miniaturization, multiplexed analysis, and easy integration in lab-on-a-chip devices.[14,22,27] The current fabrication process for nanoplasmonic sensors requires sophisticated and costly techniques, such as e-beam lithography. This inevitably hinders the implementation of nanoplasmonic technology for routine biological analysis. Therefore, we have employed a nanofabrication procedure[35] enabling efficient and large-scale production of plasmonic NHA chips, which minimizes the costs and promotes the real application both in research and clinical fields. The fabrication process is based on deep-UV photolithography technique (Figure S1, Supporting Information) by using robust quartz wafers as the sensor substrate. As a result, we obtained 4-inch diameter wafers (**Figure 2**a) patterned with
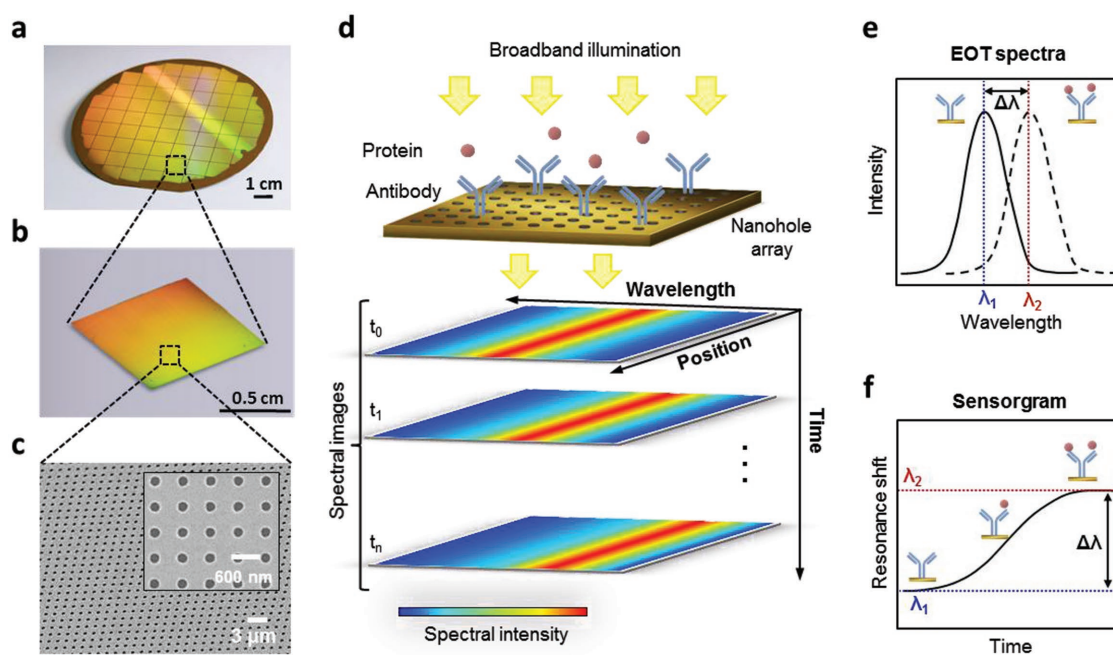

Figure 2. Configuration and working principle of the plasmonic nanohole array biosensor. a) The plasmonic nanohole arrays are fabricated uniformly on a thin gold film by wafer-scale deep-UV photolithography over the entire 4-inch diameter quartz wafer. b) The nanopatterned wafer is diced to 1×1 cm^2 sensor chip for analysis. The appearance of colors on the chip when viewed at a tilt shows the diffraction grating effect resulted from the nanohole arrays on its surface. c) An SEM image shows the uniformly distributed nanohole structures on the quartz substrate, where the nanoholes have a diameter of 200 nm and are separated center-to-center by 600 nm. d) The chip functionalized with biorecognition elements is illuminated normally with a broadband light source, exciting the surface plasmons which can be characterized by the appearance of specific EOT resonance peaks in the transmitted light. The transmission spectra are recorded and analyzed by the spectroscopic imaging setup, forming spectral images over time from t_0 to t_n. The two axes of the spectral images correspond to spatial position and wavelength. Upon analyte binding to the biorecognition elements, the change of refractive index on the plasmonic surface induces a wavelength shift of the resonance peak of the transmitted light. e) The spectral wavelength shift of the EOT resonance peak extracted from the spectroscopic images can be quantified directly in proportion to the changes of refractive index due to accumulated mass on the nanohole array surface. f) A sensorgram is obtained by tracking the resonance shift in real time, enabling the monitoring of biomolecular binding in a label-free manner.

ADVANCED
SCIENCE NEWS
www.advancedsciencenews.com

NANO · MICRO
small
www.small-journal.com

uniform arrays of gold nanoholes (200 nm diameter, 600 nm period) across the entire wafer surface as confirmed by SEM image analysis (Figure 2c). Wafers were further diced into small sensor chips of 1 × 1 cm² (Figure 2b) for cell analysis. The working principle of this biosensor is based on the phenomenon of extraordinary optical transmission (EOT), which is represented as a dramatic enhancement of light transmission through the regularly periodic subwavelength nanohole structures.[36,37] This light enhancement is characterized by the appearance of an EOT resonance peak in the transmission spectrum. The EOT resonance is highly sensitive to minute changes in the near-field refractive index over the nanohole surface. The molecular binding on the sensor surface induces a variation of the refractive index that leads to a spectral shift of the peak wavelength (Figure 2d). By tracing the spectral shifts with ongoing experiment time, we are able to depict the molecule binding events in a real-time format.

We characterized the performance and sensitivity of our NHA biosensor for label-free spectroscopic imaging. For the measurements, we placed the sensor chip on an inverted microscope where a collimated broadband light source illuminated the NHAs at normal incidence, resulting in the onset of EOT phenomenon (Figure S2, Supporting Information).[38] The transmitted light was collected by the objective underneath and coupled to a spectrometer through a 500 µm wide slit opening. The spectral content is then dispersed by a grating (600 lines mm⁻¹) and recorded on a 1024 × 1024 pixel CCD camera with a pixel size of 13 × 13 µm². The recorded CCD image consists of a spatially resolved 1D spectral image in which the horizontal axis represents the range of optical wavelength while the other represents the positions across the illuminated area of the NHAs through the slit opening (Figure 2d). By adjusting the wavelength to the EOT resonance position (i.e., ≈860 nm in aqueous solution), we can directly observe the EOT peak (Figure 2e) and monitor the spectral displacements in real time (Figure 2f). To evaluate the system sensitivity, we carried out a bulk refractive index calibration, which was determined to be 630 nm RIU⁻¹ (Figure S2, Supporting Information). This sensitivity outranges the majority of the state-of-the-art nanoplasmonic biosensors, demonstrating the unique potential of our system to perform single-cell secretion analysis.[21,39,40]

2.2. Surface Functionalization of NHA Biosensor for Cell Capture and Cytokine Detection

The establishment of a robust and stable surface chemistry strategy is critical in affinity-based biosensors to ensure sensitive, selective and reliable biodetection of the analytes-of-interest from a complex matrix such as cell media. This is particularly essential for in situ single-cell analysis since we ought to coimmobilize both cell and cytokine capturing probes (i.e., antibodies) for an extended period of time. **Figure 3**a illustrates the schematics of the designed surface functionalization. First, we coated the gold chip surface with an antifouling self-assembled monolayer (SAM) composed of polyethylene glycol (PEG) derived compounds, preventing binding of nonspecific molecules.[41] In particular, a mixture of two kinds of PEGylated alkanethiols was employed, with one carrying a reactive

carboxylic functional group (—COOH) and the other nonreactive hydroxyl group (—OH), respectively. The latter serves as a lateral spacer to minimize steric hindrance effects during protein attachment. The reactive carboxylic groups were subsequently activated by the general carbodiimide chemistry (i.e., EDC/NHS activation) that allows covalent binding of molecules presenting terminal amine groups (—NH2). At this point, we coimmobilized a mixture of streptavidin and poly-L-lysine (PLL), both containing a significant amount of terminal amine groups. PLL is a well-known polymer with the positive net charge that acts as an electrostatic force to attach floating cells (negative net charge),[42] avoiding any chemical modification of the cell membrane and therefore ensuring immobilization without affecting the cell physiology. Streptavidin was in turn used for the highly stable and oriented immobilization of biotinylated antibodies (Ab) against the cytokine of interest (IL-2). We tested the efficacy of our surface chemistry strategy for both cell attachment and cytokine detection, by depositing a cell suspension sample on the functionalized chip and incubating for 1 h at 37 °C. After carefully rinsing, we confirmed the presence of cells immobilized on the NHA surface by scanning electron microscopy (Figure 1c).

To evaluate the biosensor sensitivity for cytokine detection, we performed a calibration curve with standard protein samples. Samples spiked with different concentrations of recombinant IL-2 proteins (from 50–1000 pg mL⁻¹) were introduced over the functionalized NHAs. We employed a conventional PDMS microfluidic system with microchannels (500 µm wide, 180 µm high) for the sample injection, which was connected to a syringe pump for a continuous buffer flow. As shown in Figure 3b, the capturing of IL-2 to the antibodies was depicted by resonance shifting (Δλ) in a concentration-dependent manner. Higher concentrations of IL-2 samples lead to a greater resonance shift, as well as the progression of signals being accelerated with increasing concentrations. The plateau Δλ values obtained from each sample were then plotted as a function of the corresponding concentrations. By fitting to a nonlinear regression model (Figure 3c), we determined the limit of detection (LOD) of our biosensor, which is defined as the concentration with a signal amplitude corresponding to three times the standard deviation of the blank signal.[43] Based on the background signal we obtained from the zero-spiked sample, we achieved an outstanding LOD of 39 pg mL⁻¹ (2.6 pM) for IL-2 detection.

2.3. Design and Characterization of the Multifunctional Microfluidic System

Renewal of continuous media flow as employed in conventional microfluidic cell assays is not practical for single cell analysis, as it inhibits the accumulation of cell secretions, and thus results in depletion of target molecules. Isolating target cells within an enclosed volume, and minimizing this incubation chamber size would naturally facilitate sensitive biodetection required for single-cell resolution, through minimization of diffusive target loss. However, a number of challenges emerge. The intrinsic property of high gas permeability of thin PDMS membranes enables this material to be ideal for live cell culture. However,
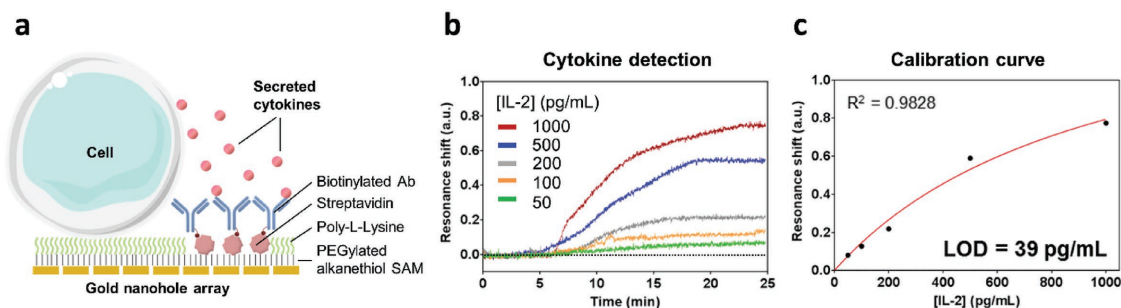
Figure 3. Surface chemistry and characterization of the NHA biosensor for IL-2 detection. a) Surface functionalization strategy for cell attachment and in situ detection of secreted cytokines: the gold surface is modified with a PEGylated alkanethiol self-assembled monolayer (SAM), functional groups of the SAM (COOH) are activated to bind to a mixture of streptavidin and poly-L-lysine covalently. Streptavidin is used to firmly attach the biotinylated antibodies against the target cytokines, while poly-L-lysine to stabilize the anchoring the cells on the sensor surface. b) Real-time sensorgrams of different concentration of cytokines (IL-2) ranging from 50 pg mL^{-1} to 1 ng mL^{-1}. c) Standard calibration curve for direct and label-free detection of IL-2 molecules. Each data point represents the mean value of 3 replicates. The limit of detection (LOD) is determined as the signal corresponding to three times the standard deviation of the blank.

this permeability also leads to evaporation of water through the PDMS structure, which can be problematic for long-term experiments. The significant degree of evaporation and subsequent shift in refractive index hampers the nominal operation of the NHA biosensor (**Figure 4**a).

We experimentally verified the detrimental effects of fluidic evaporation through bulk PDMS on sensor reliability with a basic microfluidic channel design placed within a 37 °C environment (Figure 4b). The evaporation induced significant drift in the resonance response compared to room temperature with the same relative humidity and under the same illumination scheme. Whereas, we obtained a more stable optical readout by supplying doubled humidity surrounding the microfluidics placed in a custom humidity box. This experiment confirmed
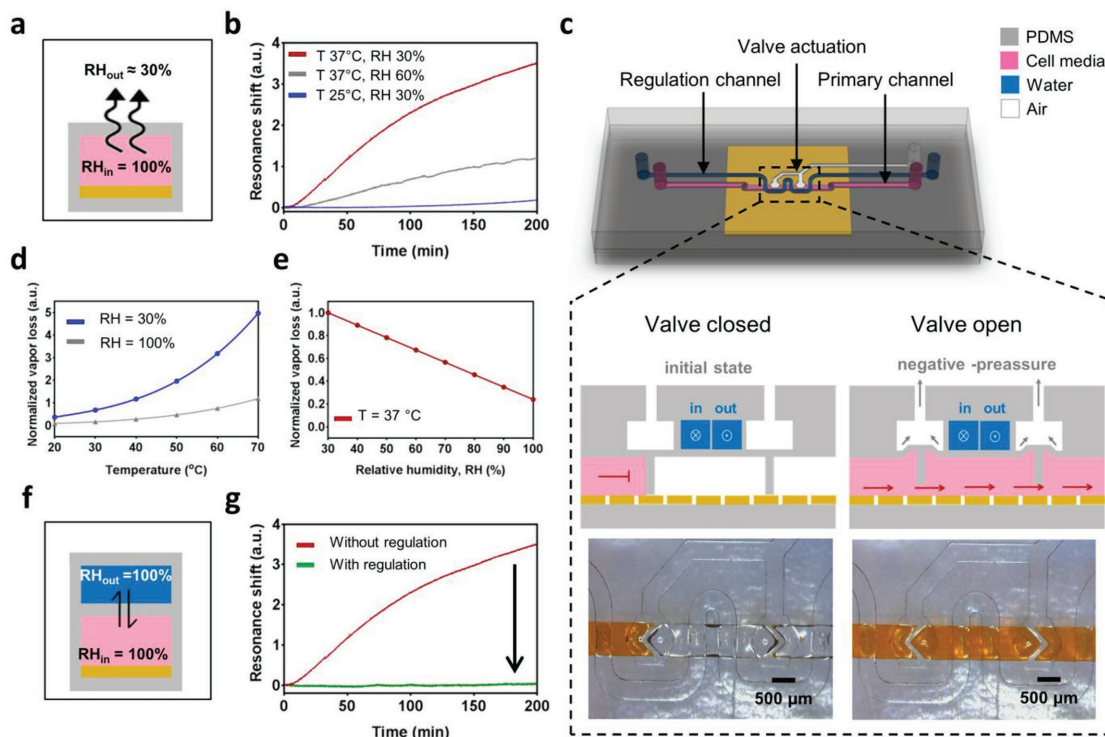
Figure 4. Design and characterization of the microfluidic system. a) Schematic illustration representing the evaporation of water from the PDMS microchamber (RH$_{in}$) to the surroundings (RH$_{out}$). b) Baseline drifts of the resonance peak under different conditions surrounding the microchamber with varying temperature and relative humidity. c) Schematic representation of the microfluidic system design with the primary channel for cell injection and culture (pink), pneumatic actuation (white) and the regulation channel blue). Zoom-in figures represent the cross-sectional view of the microfluidic system and the valve actuation mechanism. Real pictures of the microfluidic system are shown at the bottom. d) Numerical calculations of the vapor loss dependency on the temperature at different relative humidity. e) Numerical calculations of the vapor loss dependency on the relative humidity at 37 °C. f) Schematic illustration representing the compensation for the evaporation by the regulation channel filled with water. g) Baseline drift comparison of the sensor signal obtained without regulation (red) and with the regulation system (green) filled with water (100% humidity).

**ADVANCED
SCIENCE NEWS**

www.advancedsciencenews.com

NANO · MICRO

small

www.small-journal.com

that relatively high humidity is crucial to prevent evaporation and therefore to facilitate stable optical measurements.

In order to stabilize optical response under cell culture conditions, we have designed a novel multilayered microfluidic system utilizing our recently introduced injection molding fabrication technique (Figure S3, Supporting Information).[34] This system allows an isolated microchamber (Length × Width × Height ≈ 2 mm × 500 µm × 180 µm) with a chamber volume of 180 nL for cell measurements while compensating for vapor loss across the gas permeable PDMS structure. The microfluidic device utilises normally closed pneumatically actuated microvalves to isolate the fluid within the small incubation chamber. A schematic of this system is shown in Figure 4c. The primary channel is fabricated in the bottom layer for simple introduction of cells to the biosensor and potential cell retrieval after analysis. The upper layer incorporates the pneumatic lines and actuation chambers required to actuate the isolating microvalves, and a serpentine hydraulic regulation channel to regulate the local humidity and temperature of the incubation chamber. This is facilitated through a thin PDMS membrane present between the regulation and primary channel.

Evaporation of water occurs due to the vapor pressure difference across the wet and dry sides of a PDMS membrane. Based on the theoretical evaluation (Supporting Information 1.3), the evaporation rate through a PDMS membrane would mainly depend on the surface area and thickness of the membrane as well as the temperature and relative humidity of the ambient environment. Using this equation, we calculated the evaporation rate versus different environmental parameters, particularly the typical cell culture temperature (i.e., 37 °C). As shown in Figure 4d, increasing temperature promotes evaporation. In contrast, elevating the relative humidity on the wet membrane minimizes the evaporation from the incubation chamber, and ultimately reduces to nearly zero at a relative humidity of 100% (Figure 4e), which corresponds to the conditions when the regulation channel is filled with water, as shown in Figure 4f. At this point, although the vapor loss through the bulk PDMS and dry membranes persist, it is compensated by vapor transfer across the wet membrane driven by resulting vapor pressure difference. This is evidenced by the improved stability of the signals shown in Figure 4g.

2.4. Real-Time Analysis of IL-2 Secretion from Single EL4 Cells

After characterization and optimization of our optofluidic biosensor, we examined the performance for direct and label-free single cell IL-2 secretion analysis. IL-2 is one of the essential cytokines that are actively involved in numerous biological activities of the immune system, and it particularly exerts prominent functions in regulating the proliferation, activation, and differentiation of T lymphocytes.[44] Therefore, the dynamic analysis of IL-2 secretion events provides insights to better understand its pathophysiological roles in the immune system as well as its potential applications in disease treatments. We selected EL4 lymphoma cells for our experiments, as these cells are engineered to secrete IL-2 cytokines only upon defined chemical stimulus,[45] which represent an optimum

IL-2 secretion cell population to evaluate the sensitivity and specificity of our new analytical platform.

To perform the assay, we functionalized the nanoplasmonic chip as described before and assembled it with the multilayer microfluidic system. EL4 cells suspended in cell media were introduced into the primary channel with an ultralow cell density. The pneumatic valves were subsequently closed to stop the flow which resulted in a few isolated single cells being enclosed in the valve-gated chamber (**Figure 5**a). After a short period of incubation at 37 °C to allow firm cell attachment to the NHA surface, the optofluidic device was placed in the inverted microscope equipped with a customized incubator box that provides the proper temperature and CO_2 to maintain appropriate cell
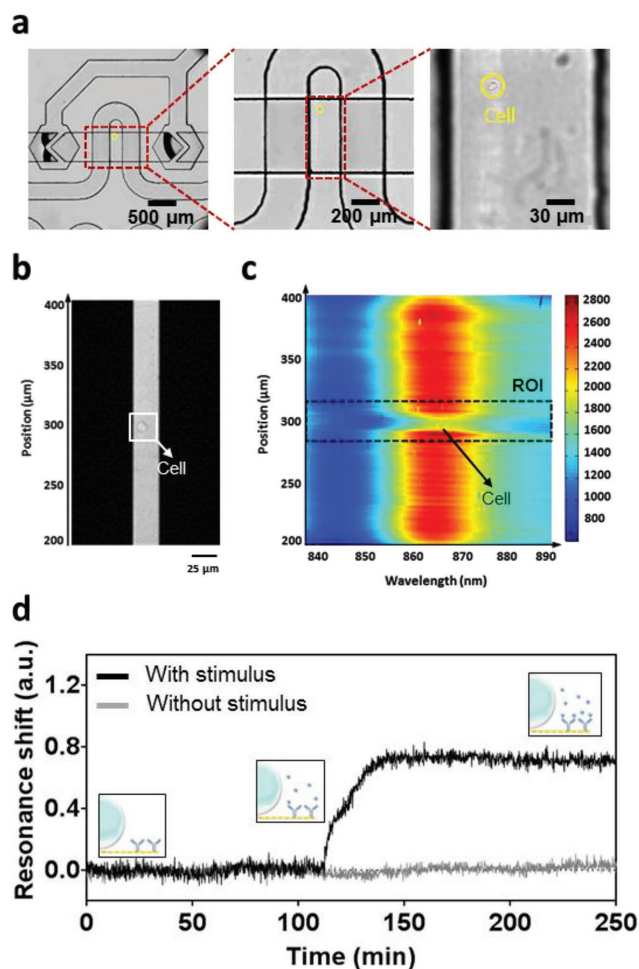
Figure 5. Real-time spectroscopic imaging of single-cell secretion. a) Optical images of an isolated cell encapsulated in the microfluidic chamber. b) CCD image of a single cell positioned in the center of the partially closed slit in the spectrometer. We cropped the image to highlight the attached single cell. Scale bar: 25 µm. c) The 1D spectroscopic image shows the EOT peak intensifies around 865 nm (red region) and the spectral signature generated by the cell spot. The region of interest (ROI, boxed with dashed line) for measurement is defined around the cell spot. d) Real-time sensorgrams obtained from a single EL4 cell secreting IL-2 cytokine upon chemical stimulation (black) and a negative control without the stimulus (gray). Inset figures schematically illustrate the IL-2 secretion and in situ capture by co-immobilized antibodies.

ADVANCED
SCIENCE NEWS
www.advancedsciencenews.com

NANO · MICRO
small
www.small-journal.com

culture conditions. Afterward, a collimated beam of broadband light illuminated the assembled device at normal incidence. We used a 20× magnification objective to image a single EL4 cell. The transmitted light through the NHAs entered the partially open slit in the spectrometer, forming an optical image recorded by the CCD camera as shown in Figure 5b. For illustration purpose, the acquired image was cropped to highlight the location of the cell. By further expanding the recorded image across the wavelength range, we obtained a 1D spectroscopic image (Figure 5c), where the spectral information was revealed alongside the exposed region of the NHAs through the slit. An evident signature in the spectrum appeared at the exact location where the single EL4 cell resides, which resulted from the distinct refractive index of cells. This unique phenomenon allowed us to position a single cell during spectroscopic imaging and define a specific region of interest (ROI) for biodetection. The ROI was subsequently defined in a way that it covers the cell position and the immediate surrounding NHA areas functionalized with anti-IL2 antibodies. In particular, we designated a 40-pixel ROI which corresponds to ≈30 μm on the NHA surface. Then, we extracted the corresponding spectrum of the transmitted light, which shows the EOT resonance peak at ≈860 nm. In order to monitor the capture of analytes in real time, we developed customized MATLAB scripts based on the centroid algorithm[26] to continuously interrogate the resonance peak shifts and to provide a precisely recorded sensorgram. Rather than simply tracking the shifts of maximum peak value, we significantly enhance the signal-to-noise ratio and improve the biosensor sensitivity. We exploited a custom built MATLAB interface that allows ROI definition, spectrum visualizing, centroid calculation and real-time sensorgram display in a user-friendly manner.

To start the analysis, we injected the chemical stimulus including the Ca^{2+} ionophore ionomycin and the phorbol ester PMA into the primary channel to initiate the activation and secretion of the EL4 cell. Immediately following stimulation, we closed the valve gates to keep a static and controlled volume in the cell microchamber. Then, we commenced the continuous monitoring of the peak position that displays the sensorgram in real time ($t = 0$). As shown in Figure 5d, we observed a significant resonance shift emerging at around $t = 110$ min (black curve). The signal increase could be directly attributed to the secretion and in situ capture of the IL-2 molecules. We performed an independent negative control experiment employing the same cell culture environment and analysis conditions but without injecting any external stimuli to verify this phenomenon. EL4 cells are a well-characterized cell line that only secretes IL-2 proteins upon proper activation by the chemical stimulus, so cells in common culture media should not produce any sensor response. As can be seen in Figure 5d, the gray line remained stable over the whole analysis duration. The absence of resonance response from the negative control indicates that our biosensor is not only selective for the detection of IL-2 but also repellent to other matrix proteins present in the culture media, avoiding any interference with the cell analysis. We demonstrated that our innovative lab-on-a-chip system is able to detect protein secretion from a single cell in a precise and accurate manner.

2.5. Temporal and Spatial Diffusion Analysis of Single-Cell Secretion

To account for the detection flexibility of our NHA sensing surface, we further exploited the biosensor to characterize the spatial features of single cell secretion in real time. The design of our nanoplasmonic surface with a uniform surface-spanning NHAs enables the simultaneous and independent monitoring of different ROIs. This feature permits not only analysis and detection of single-cell secretion in real time, but observation of the molecular diffusion along the sensor surface. Following the same procedure described before, we introduced different EL4 cells in the biosensor and enclosed them in the microfluidic chamber. **Figure 6**a shows the spectral signature of an isolated cell attached to the NHA chip, and enclosed within the valve-gated PDMS microchamber. In order to analyze the spatial diffusion of the secreted cytokines, we defined different ROIs covering the specific cell spot and surrounding areas (Figure 6b). In this case, each ROI measures 20 pixels in width and separates 40 pixels (center-to-center) away from each counterpart. Considering the overall optical magnification of the system, each ROI was ≈13 μm in width and ≈27 μm in period. The ROIs were extracted as independent spectral curves, and the peak centroids were interrogated in real time (Figure 6c).

We performed this measurement for three independent single EL4 cells (Figure 6d–f). In all cases, we observed a burst of IL-2 secretion at around 110–120 min poststimulation from the cell spot, as well as from the adjacent ROIs (ROI 1 and 1'). There was roughly 20 min of delay for the onset of resonance response from ROI 2/2'. The amount of resonance shifts declined from the cell spot outward, which we attribute to the diffusion process of cytokines in the static media environment. By plotting the endpoint secretion amount of IL-2 (in this case, at 180 min) as a function of different ROIs' locations, we obtained a bell-shaped secretion distribution (Figure 6g–i), where the secretion apex occurred within the central cell spot and declined almost symmetrically outward. It should be mentioned that the label-free biosensing configuration is not able to provide a 3D mapping of the cytokine secretion around the cell, but only the spatial distribution along the sensor surface surrounding the cell. However, the absence of flow in the microchamber and the long-time monitoring might facilitate the secreted cytokines to diffuse effectively across the sensor surface and therefore enable the quantification. The local IL-2 concentration was calculated by interpolating the relative resonance shift to the calibration curve (Figure 3c). We found significant differences among the three different cells. Especially the second measurement (Cell 2) showed a higher amount of secreted IL-2 (2500 pg mL⁻¹) while Cell 1 and Cell 3 appear to secrete less cytokine. This was also reflected in the spatial diffusion analysis, where we observed a more centralized spatial distribution for Cell 2. This phenomenon reveals the intrinsic heterogeneity in a bulk cell population. Whereas by using conventional methods for cell secretion analysis (e.g., ELISA), we would only obtain a single average value for IL-2 secretion at discrete time points. Our single-cell analysis method is promising for accurate observation and precise measurement of protein secretion from individual cells.
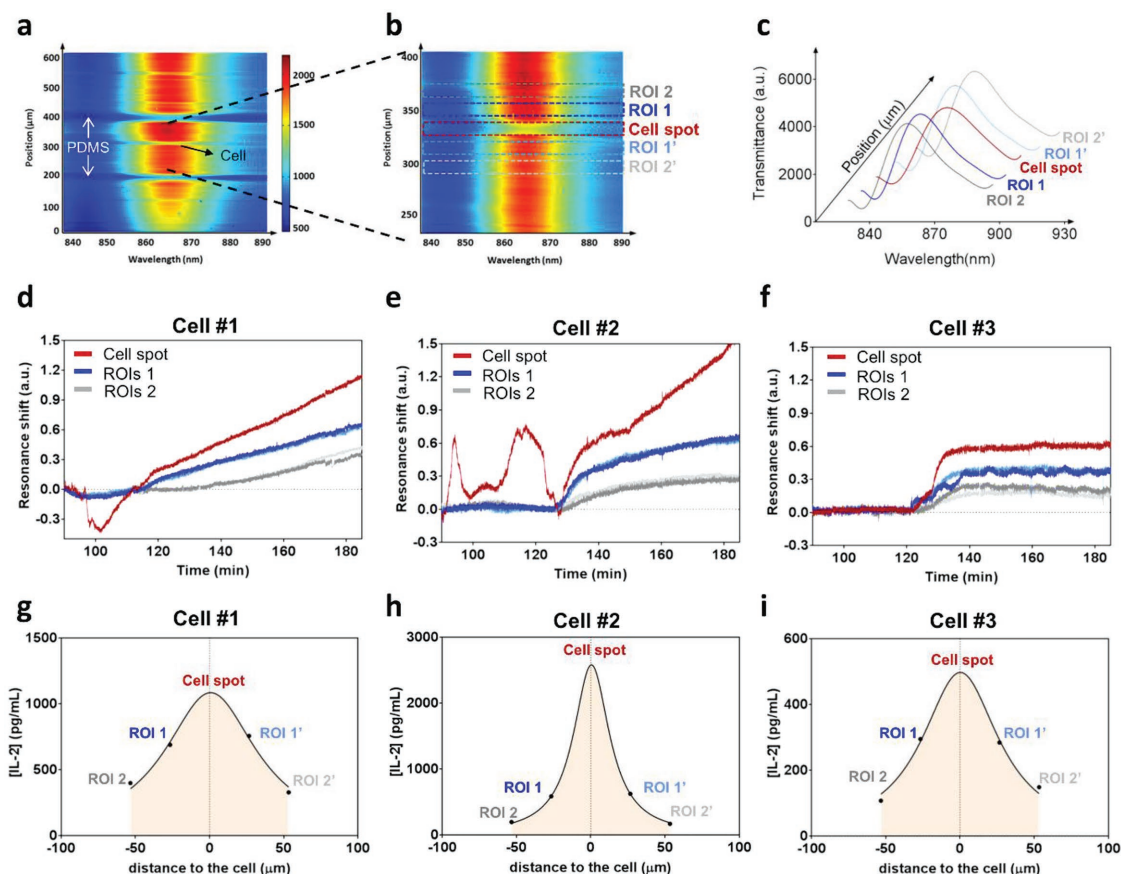
ADVANCED
SCIENCE NEWS
www.advancedsciencenews.com

NANO · MICRO
small
www.small-journal.com

Figure 6. Temporal and spatial diffusion analysis of single cells by label-free spectroscopic imaging. a) Spectral CCD image of the optofluidic system with three isolated cells encapsulated in the microchamber. Strong spectral gaps correspond to the interfacing PDMS of the regulation channel. b) Zoom-in of the spectral image for the ROIs definition at the center cell spot and surrounding areas. c) Spectral EOT peaks corresponding to the selected multiple ROIs. The peaks are interrogated simultaneously and independently. d–f) Independent measurements of IL-2 secretion from three different EL4 cells, monitoring the cell spot ROI and surrounding ROIs simultaneously. g–i) Spatial diffusion analysis of the secreted cytokines: plots correspond to the interpolated concentration of signals acquired for every ROI, fitted to a Gaussian distribution.

It is worth emphasizing that some stochastic noise was observed at the cell spots for Cell 1 and Cell 2 while leaving other ROIs clear of such interference (Figure 6d,e). We could attribute this noise to either cell membrane changes or stochastic cellular movement.[46] In order to prove this hypothesis, we performed another experiment where we split the transmitted light beam to simultaneously image the cell with a CCD camera and measure the plasmonic response. We observed the cell movement within an extremely narrow margin (less than 10 µm) before the onset of cytokine secretion (Figure S4, Supporting Information). This confirms that during the early stage of cell activation, cells undergo certain movements and possible membrane activities. The narrow scope of activity does not influence the detection of cytokines in the surrounding areas. It is important to mention that such phenomena were absent for Cell 3 measurement, while this cell secreted a much lower quantity of cytokines compared to the others. Therefore, the active cell movements could be associated with a higher secretion capacity. Overall, we have demonstrated the superior capabilities of our innovative optofluidic system for the single-cell analysis. This microfluidic-integrated nanoplasmonic biosensor enables a complete analysis of cell activation and secretion

from isolated individual cells in a label-free, real-time, and user-friendly manner. By expanding the real-time single-cell analysis to a high-throughput configuration with the incorporation of microfluidic cell traps or other strategies,[47] we would be able to identify and study cell activation and secretion more efficiently. Besides, the possibility of retrieving the cells after the analysis would make our optofluidic sensor an ideal system for its application in biomedical research.

3. Conclusion

We introduce a novel design of an optofluidic nanoplasmonic biosensor for single-cell cytokine secretion analysis. This biosensor platform builds upon the ultrasensitive gold nanohole arrays integrated with an easy to fabricate but sophisticated microfluidic system, enabling real-time monitoring of protein secretion from live cultured cells at single-cell resolution in a label-free manner. The integration of pneumatically actuated valve gates in the microfluidic device generates an isolated chamber with a few nanoliters volume for sensitive cell analysis. In particular, we incorporate for the first time a novel

multifunctional microfluidic design involving both regulation and primary microchannels to tackle the common PDMS-mediated evaporation challenge for reliable biodetection. This novel design circumvents the need for conventional oil sealing or providing a rather high ambient relative humidity, achieving a user-friendly and facile biodetection configuration. With this biosensor setup, we achieved an outstanding sensitivity of 39 pg mL^{-1} for direct IL-2 detection in complex media. The IL-2 molecules secreted from individual EL4 lymphoma cells can also be directly monitored over several hours without interrupting the cell culture. The uniform arrangement of NHAs over the whole sensor chip surface also allows us to elucidate the spatial distribution of cell secretion. Furthermore, the analysis with different single EL4 cells reveals distinct fingerprints for secretion capacity despite their similar phenotypes. With these capabilities, the proposed nanoplasmonic biosensor system represents a powerful tool to analyze cytokine secretion at the single-cell level in a label-free and real-time manner.

4. Experimental Section

Fabrication of NHA-Based Biosensor: The gold NHA chips were manufactured by using wafer-scale and high-throughput nanofabrication techniques on a robust, transparent quartz substrate in a single lithography step. Briefly, Radio Corporation of America (RCA) cleaned 4 inch fused silica wafers were first coated with Ti/Au (10/120 nm) by an e-beam evaporator (Alliance-Concept EVA 760). The Ti layer enabled the Au adhesion on the glass substrate, as well as suppressed the irrelevant surface modes induced by the Au/glass interface. Therefore, only the (1, 0) Au/Medium EOT peak could be monitored through a wide spectral interval, which was critical for wide dynamic sensing range. Next, the NHAs (200 nm diameter and 600 nm period) were patterned using a 248 nm deep-UV stepper (ASML PAS 5500/300 DUV) and were transferred into the Ti/Au layer using an ion beam etching tool (Oxford Instruments PlasmaLab 300 IBE) after developing the photoresist. The resist residuals on the surface were removed by oxygen plasma cleaning. Finally, the 4 inch processed wafer was diced into 1 cm × 1 cm chips for the subsequent optical measurements.

Fabrication of Microfluidic System: Microfluidic devices were manufactured with polydimethylsiloxane (PDMS, SYLGARD 184 SILICONE ELASTOMER KIT) by using a combination of the membrane sandwich fabrication method[48] and PDMS injection molding technique.[34] Figure S3 (Supporting Information) illustrates a pair of complementary molds that were utilized for the injection molding process. Molds were fabricated by standard photolithography techniques,[49] as described in the previous work.[34] In brief, SU-8 3050 (MicroChem Corp) was used to pattern the transparent upper borosilicate glass wafer substrate, and lower silicon wafer substrate with protruding features, with a height of 160 and 180 μm, respectively. PDMS prepolymer was prepared by mixing the silicone elastomer and the curing agent with a weight ratio of 10:1 respectively, followed by thorough degassing in a vacuum desiccator. The prepolymer was introduced between the molds, which were optically aligned and clamped in position under a dissecting microscope. Standoff distance between the molds could be adjusted by changing the spacer material positioned between supporting pillars regularly positioned across the molds. The clamped mold assembly was cured in an oven at 80 °C for 1 h and separated to extract the cured PDMS slab, which was further cut to size and biopsy punched with viaducts providing a pathway between the primary channel and primary channel interface lines. The upper surface was plasma bonded (Harrick Plasma PDC-002: 100% O$_2$, 1 min) to a 5 mm thick blank PDMS interface slab that was previously biopsy punched with 1 mm interface holes aligning with the interface areas on the fluidic inlets, outlets, and pneumatic interface areas. Microchannels

were patterned on both sides of the injection molded slab, namely, the primary channel measuring 500 μm in width for cell culture on the bottom surface, which corresponds to 500 μm wide fluidic interface lines on the upper surface, pneumatic actuation channels and 300 μm wide fluidic regulation channels were also patterned on the upper layer. The fluidic interface lines connected through biopsy-punched viaducts to the accessible interface areas, allowing fluidic access to the primary channel on the bottom layer. The complementary molds were separated by ≈60 μm during PDMS casting, resulting in a thin PDMS membrane (i.e., the regulation membrane) between the regulation and the primary channels. The detailed fabrication process of the pneumatically controlled valves was described elsewhere in a previous work outlining the simplified method by injection molding.[34] In Brief, the valve gates consisted of protruding barriers obstructing fluid flow positioned within the primary channel, directly under the actuation chambers, and forming an isolated channel segment as the incubation chamber. A thin PDMS membrane separated the hexagonal pneumatic actuation chambers and primary channel. When the actuation chambers were evacuated, the valve membranes were deflected upward, raising the valve gates clear of the primary channel floor and allowing fluid flow across the valves. The regulation channel passed in parallel above the primary channel and followed a serpentine configuration directly over the valve-gated area, readily maintaining the steady state of the isolated volume underneath the membrane.

Functionalization and Characterization of the Biosensor for IL-2 Detection: The nanoplasmonic chip was cleaned by consecutive washes in acetone, ethanol, and Milli-Q water, and then further treated with a UV-ozone cleaner (Bioforce Nanosciences) for 20 min. The detailed functionalization procedure is described in our previous publication.[25] Briefly, the cleaned chip was first coated with a mixture of PEGylated alkanethiols in absolute ethanol overnight at room temperature. The carboxylic groups on the chip surface were then activated by incubating with a cross-linking solution containing 200 × 10^{-3} M EDC and 50 × 10^{-3} M sulfo-NHS in 0.1 M MES buffer (pH = 4.5) for 15 min at room temperature. Subsequently, the activated chip was incubated with 0.01% poly-L-lysine and 100 μg mL^{-1} streptavidin solution diluted in phosphate-buffered saline (PBS) overnight at 4 °C, followed by incubation with biotinylated IL-2 antibodies (50 μg mL^{-1}) at room temperature for 1 h.

To determine the bulk refractive index sensitivity, a serial sequence of incrementally increasing dilutions of glycerol solutions with known refractive indices (RI)[50] was introduced in the biosensor and tracked the induced resonance shifts (Figure S2, Supporting Information). By plotting the resulting wavelength changes (Δλ) and fitting to a linear regression equation, the bulk sensitivity of the sensor (i.e., slope) was determined to be 630 nm RIU^{-1} (Figure S2, Supporting Information).

To calibrate the optical responses to multiple concentrations of IL-2, the standard recombinant IL-2 proteins diluted in PBS with gradient concentrations were injected over the biosensor chip at a flow rate of 20 μL min^{-1}. We utilized a conventional microfluidic system with microchannels (500 μm wide, 180 μm high) for the sample injection, which was connected to a syringe pump for continuous buffer flow. Each concentration was measured in triplicate. The chip surface could be regenerated by injecting 20 × 10^{-3} M NaOH solution post each injection. In addition, the calibration curve does not differ significantly from different dilution medium (i.e., cell medium vs PBS), which excludes possible matrix interferences. The limit of detection (LOD) of the biosensor was defined as LOD = 3 × σ_x, where σ_x is the standard deviation of the background optical signal.

Optical Measurement Setup and Data Processing: A spectrometer (Shamrock 303i, Andor, spectral resolution 0.1 nm) and a deep-cooled CCD camera (iKon-M, Andor) were installed onto an inverted microscope (Nikon Ti-U) to perform EOT-based optical measurements. A broadband tungsten–halogen lamp illuminated the nanoplasmonic chip at normal incidence. For single cell monitoring, the EOT signals were collected using a 20 × objective (CFI Plan Fluor DLL, NA = 0.5) lens from one individual EL4 cell and entered the spectrometer through a 400 μm wide slit opening, forming a 1D spectroscopic image. Andor Solis software was employed to analyze the spectra. Due to the spatial coverage of the

ADVANCED
SCIENCE NEWS
www.advancedsciencenews.com

NANO · MICRO
small
www.small-journal.com

nanostructures over the entire sensor surface, it was flexible to define the measurement loci according to specific needs, namely by selecting different positions of the region-of-interest (ROI). The spectroscopic images were obtained with 0.5 s exposure, and a grating of 600 lines mm^{-1} was used to have sufficient spectral resolution. The spectra were extracted from each ROI on the image by a custom MATLAB image processing script. The resonance peak position was defined by calculating the centroid of the peak within a fixed wavelength window (40% maximum intensity) and plotted in real time. Sensorgrams showed the centroid shifting versus time of multiple ROIs simultaneously. To extract reliable information from cell secretion, the sensorgrams were further normalized employing a control ROI placed on a cell-free region. To quantify the spectral shift and interpolate the calibration curve, curve fitting of the sensorgrams was performed with nonlinear regression using GraphPad Prism 7. The correlation between cytokine diffusion and multiple ROI locations was analyzed by Gaussian Lorentizian distribution.

Supporting Information

Supporting Information is available from the Wiley Online Library or from the author.

Acknowledgements

Conflict of Interest

The authors declare no conflict of interest.

Keywords

[1] J. R. Heath, A. Ribas, P. S. Mischel, *Nat. Rev. Drug Discovery* **2016**, *15*, 204.
[2] D. Wang, S. Bodovitz, *Trends Biotechnol.* **2010**, *28*, 281.
[3] A. Koseska, P. I. Bastiaens, *EMBO J.* **2017**, *36*, 568.
[4] G. C. Tsokos, N. R. Rose, *Clin. Immunol.* **2017**, *181*, 1.
[5] G.-C. Yuan, L. Cai, M. Elowitz, T. Enver, G. Fan, G. Guo, R. Irizarry, P. Kharchenko, J. Kim, S. Orkin, J. Quackenbush, A. Saadatpour, T. Schroeder, R. Shivdasani, I. Tirosh, *Genome Biol.* **2017**, *18*, 84.
[6] J. C. Love, J. L. Ronan, G. M. Grotenbreg, A. G. van der Veen, H. L. Ploegh, *Nat. Biotechnol.* **2006**, *24*, 703.
[7] Y. Shirasaki, M. Yamagishi, N. Suzuki, K. Izawa, A. Nakahara, J. Mizuno, S. Shoji, T. Heike, Y. Harada, R. Nishikomori, O. Ohara, *Sci. Rep.* **2014**, *4*, srep04736.
[8] A. J. Torres, A. S. Hill, J. C. Love, *Anal. Chem.* **2014**, *86*, 11562.
[9] A. J. Torres, R. L. Contento, S. Gordo, K. W. Wucherpfennig, J. C. Love, *Lab Chip* **2013**, *13*, 90.
[10] V. Chokkalingam, J. Tel, F. Wimmers, X. Liu, S. Semenov, J. Thiele, C. G. Figdor, W. T. S. Huck, *Lab Chip* **2013**, *13*, 4740.
[11] Y. F. S. Seah, H. Hu, C. A. Merten, *Mol. Aspects Med.* **2018**, *59*, 47.
[12] Y. Lu, L. Yang, W. Wei, Q. Shi, *Lab Chip* **2017**, *17*, 1250.
[13] S. Sang, Y. Wang, Q. Feng, Y. Wei, J. Ji, W. Zhang, *Crit. Rev. Biotechnol.* **2016**, *36*, 465.
[14] H. Im, H. Shao, Y. I. Park, V. M. Peterson, C. M. Castro, R. Weissleder, H. Lee, *Nat. Biotechnol.* **2014**, *32*, 490.
[15] S.-H. Wu, K.-L. Lee, A. Chiou, X. Cheng, P.-K. Wei, *Small* **2013**, *9*, 3532.
[16] B.-R. Oh, N.-T. Huang, W. Chen, J. H. Seo, P. Chen, T. T. Cornell, T. P. Shanley, J. Fu, K. Kurabayashi, *ACS Nano* **2014**, *8*, 2667.
[17] M. C. Estevez, M. Alvarez, L. M. Lechuga, *Laser Photonics Rev.* **2012**, *6*, 463.
[18] X. Fan, I. M. White, S. I. Shopova, H. Zhu, J. D. Suter, Y. Sun, *Anal. Chim. Acta* **2008**, *620*, 8.
[19] A. B. González-Guerrero, S. Dante, D. Duval, J. Osmond, L. M. Lechuga, *Procedia Eng.* **2011**, *25*, 71.
[20] L. Tu, X. Li, S. Bian, Y. Yu, J. Li, L. Huang, P. Liu, Q. Wu, W. Wang, *Sci. Rep.* **2017**, *7*, 11020.
[21] G. A. Lopez, M.-C. Estevez, M. Soler, L. M. Lechuga, *Nanophotonics* **2017**, *6*, 123.
[22] A. E. Cetin, A. F. Coskun, B. C. Galarreta, M. Huang, D. Herman, A. Ozcan, H. Altug, *Light: Sci. Appl.* **2014**, *3*, e122.
[23] T.-Y. Chang, M. Huang, A. A. Yanik, H.-Y. Tsai, P. Shi, S. Aksu, M. F. Yanik, H. Altug, *Lab Chip* **2011**, *11*, 3596.
[24] C. Escobedo, *Lab Chip* **2013**, *13*, 2445.
[25] D. R. Shankaran, K. V. Gobi, N. Miura, *Sens. Actuators, B* **2007**, *121*, 158.
[26] X. Li, M. Soler, C. I. Özdemir, A. Belushkin, F. Yesilköy, H. Altug, *Lab Chip* **2017**, *17*, 2208.
[27] M. Soler, A. Belushkin, A. Cavallini, C. Kebbi-Beghdadi, G. Greub, H. Altug, *Biosens. Bioelectron.* **2017**, *94*, 560.
[28] J. Park, H. Im, S. Hong, C. M. Castro, R. Weissleder, H. Lee, *ACS Photonics* **2018**, *5*, 487.
[29] J. He, A. T. Brimmo, M. A. Qasaimeh, P. Chen, W. Chen, *Small Methods* **2017**, *1*, 1700192.
[30] S. Halldorsson, E. Lucumi, R. Gómez-Sjöberg, R. M. T. Fleming, *Biosens. Bioelectron.* **2015**, *63*, 218.
[31] Y. S. Heo, L. M. Cabrera, J. W. Song, N. Futai, Y.-C. Tung, G. D. Smith, S. Takayama, *Anal. Chem.* **2007**, *79*, 1126.
[32] E. Berthier, J. Warrick, H. Yu, D. J. Beebe, *Lab Chip* **2008**, *8*, 852.
[33] P. C. Thomas, S. R. Raghavan, S. P. Forry, *Anal. Chem.* **2011**, *83*, 8821.
[34] C. Szydzik, B. Niego, G. Dalzell, M. Knoerzer, F. Ball, W. S. Nesbitt, R. L. Medcalf, K. Khoshmanesh, A. Mitchell, *RSC Adv.* **2016**, *6*, 87988.
[35] F. Yesilkoy, R. A. Terborg, J. Pello, A. A. Belushkin, Y. Jahani, V. Pruneri, H. Altug, *Light: Sci. Appl.* **2018**, *7*, 17152.
[36] L. Martín-Moreno, F. J. García-Vidal, H. J. Lezec, K. M. Pellerin, T. Thio, J. B. Pendry, T. W. Ebbesen, *Phys. Rev. Lett.* **2001**, *86*, 1114.
[37] S. G. Rodrigo, L. Martín-Moreno, A. Y. Nikitin, A. V. Kats, I. S. Spevak, F. J. García-Vidal, *Opt. Lett.* **2009**, *34*, 4.
[38] S. Hoon Lee, N. C. Lindquist, N. J. Wittenberg, L. R. Jordan, S.-H. Oh, *Lab Chip* **2012**, *12*, 3882.
[39] L. Feuz, M. P. Jonsson, F. Höök, *Nano Lett.* **2012**, *12*, 873.
[40] M. Bahramipanah, S. Dutta-Gupta, B. Abasahl, O. J. F. Martin, *ACS Nano* **2015**, *9*, 7621.
[41] T. McPherson, A. Kidane, I. Szleifer, K. Park, *Langmuir* **1998**, *14*, 176.

[42] D. Mazia, G. Schatten, W. Sale, *J. Cell Biol.* **1975**, *66*, 198.

[43] ACS Committee on Environmental Improvement, *Anal. Chem.* **1980**, *52*, 2242.

[44] S. L. Gaffen, K. D. Liu, *Cytokine* **2004**, *28*, 109.

[45] J. J. Farrar, J. Fuller-Farrar, P. L. Simon, M. L. Hilfiker, B. M. Stadler, W. L. Farrar, *J. Immunol.* **1980**, *125*, 2555.

[46] M. P. Raphael, J. A. Christodoulides, J. B. Delehanty, J. P. Long, J. M. Byers, *Biophys. J.* **2013**, *105*, 602.

[47] T. W. Murphy, Q. Zhang, L. B. Naler, S. Ma, C. Lu, *Analyst* **2018**, *143*, 60.

[48] J. R. Anderson, D. T. Chiu, R. J. Jackman, O. Cherniavskaya, J. C. McDonald, H. Wu, S. H. Whitesides, G. M. Whitesides, *Anal. Chem.* **2000**, *72*, 3158.

[49] H. Lee, K. Lee, B. Ahn, J. Xu, L. Xu, K. W. Oh, *J. Micromech. Microeng.* **2011**, *21*, 125006.

[50] L. F. Hoyt, *Ind. Eng. Chem.* **1934**, *26*, 329.

CHAPTER 4: Hemocompatible complex microfluidics for clinical blood analysis

The overall aim of this thesis is to explore whether simplifying the fabrication approach for complex microfluidics can reduce the barrier for uptake of this technology and advance it towards reaching the potential of mass deployment. Chapter 2 introduced a simplified fabrication technique and Chapter 3 showed that the technique could greatly accelerate the development of complex microfluidic components for research applications. In Chapter 3, complex microfluidic control components were used to manipulate basic, pre-prepared biological sample fluids used in an automated assay, as well as more complex samples including live cells. While basic pre-processed biological samples don't require strict adherence to carefully controlled environmental conditions, more complex samples containing viable cell cultures are sensitive to environmental conditions including temperature, humidity, dissolved gas and nutrient concentrations, fluid PH and more [50]. With this said, the environment generated and maintained in Section 3.2 was somewhat idealised as is often the case for laboratory research.

In real world clinical diagnostics, the sample of interest is often derived from blood. Blood is an exceedingly complex biological fluid, a vast amount of information can be extracted through analysis of biomarkers present within blood plasma [51], as well as direct analysis of various cellular components and their response to stimulus [52]. While blood or its constituents contain a wealth of valuable targets for a broad range of assays, there are numerous challenges associated with handling of blood in an in-vitro environment. While the influence of the above parameters can affect blood with a relationship dependant on exposure time, various blood components are sensitive to flow conditions, surface contact, and mechanical stimulation resulting from fluid manipulation at very short or transient timeframes, particularly whole blood containing platelets [52].

For these reasons, blood samples are usually processed and divided into their constituent elements using macro scale tools in a clinic such as centrifuge and filter columns among others. These require a well-equipped clinical laboratory and skilled operators and can take significant time and require relatively large quantities of blood.

It would be a great advantage to devise lab-on-a-chip solutions that could take whole blood sourced directly from the patient as a sample input, removing the need for sending the sample to a specialised laboratory, reducing the wait time and requiring minute sample volumes. For this reason, automation of fluid handling and sample preparation using whole blood as the sample fluid, has the potential for breakthrough impact in point-of-care applications of numerous biosensor strategies.

Microvalves are a critical control component enabling microfluidic automation. Microvalves can provide fluidic isolation, allowing dynamic reconfiguration, or switching between fluids, flow control, and can be configured to work in concert as micropumps. While the literature shows that numerous variations of microvalve geometries have been applied to a broad range of applications, these previous works generally don't consider the specific requirements that must be considered when working with blood. Hemocompatibility is a critical requirement of any microfluidic system designed to operate with blood samples, be this research platforms for investigating the nature of blood, facilitating drug discovery for compounds effecting blood function, or sample preparation for point-of-care devices.

Due to the complex protein makeup of blood, interactions with microfluidic devices generally result in biofouling, resulting from protein adsorption and cellular interactions with surfaces within the microfluidic devices. As a result, blood based microfluidic systems are often considered disposable or single use devices, this is particularly relevant in the case of devices investigating reactive properties of blood, such as platelet function and thrombus formation. Statistically significant biological data requires a high degree of replicate information to allow for statistical validation and analysis, as such, blood research requires a high volume replicate microfluidic devices.

This chapter investigates the practicality and design considerations of microfluidic control components capable of handling blood without significant deleterious impact at physiologically relevant flow rates. This work was the result of a collaborative project with the Australian centre for blood diseases, Monash University, and builds on the findings of chapter 3, investigating the real-world practicality of handling increasingly complex biological samples. In addition, this work

assesses the practicality and scalability of the fabrication technique outlined in chapter 2, investigating the practicality of fabricating the large quantities (10's to 100's) of single use disposable devices required for replicate bioassays.

The research outcomes resulting from this chapter have demonstrated that not only can the fabrication technique outlined in chapter 2 facilitate rapid iterative design processes, but in addition, provide a level of repeatability and reliability suited to fabrication of large quantities of devices that are required to effectively conduct clinical biomedical research. Specifically, early prototype device geometries have been rapidly fabricated, and replicates assessed, with a turnaround of only a few days enabling numerous design iterations and rapid development. When final geometries were identified, a comprehensive battery of assays were conducted, requiring hundreds of replicate devices with minimal inter-device variance and within relatively short donor-defined timeframes.

These studies allowed additional insight into some caveats associated with the use of normally closed elastomer microvalves. These studies identified delamination of microchannel walls at valve gate edges as an area of reduced hemocompatibility, presumably due to high transient flow rates within these areas, or the mechanical effects these areas had on blood. In order to avoid delamination, selective plasma bonding was performed, using an exclusion stamp to selectively prevent plasma activation in select areas. While selective plasma bonding allowed fabrication of devices not dependant on clamping mechanisms, time dependant adhesion of PDMS to glass coverslips [53] did unfortunately limit the shelf-life of lifting gate valves used in blood-based studies to approximately two weeks from fabrication. While this issue can be countered by reversibly bonding devices closer to the time of their use, this is a challenge that will need to be overcome as a requisite for Point of care application.

As further work beyond the scope of this thesis, I would suggest further exploration of valve geometries that optimise opening height with respect to pressure gradient, while also attempting to reduce delamination associated with torsion present at the edges of open microvalves. In addition, while the use of a material other than PDMS may avoid issues associated with time

51

dependant bonding, investigation of methods avoiding this issue would still be of benefit to research platforms constructed using PDMS.

Current ongoing work, beyond the scope of this doctorate, aims to expand the outcomes of this chapter, exploring hemocompatibility of dynamic fluidic actuation components, in the context of a blood-based bioreactor for assessment of blood function. While the paper of this Section focussed on individual control components for blood handling within microfluidic systems, ongoing work is focused toward reconfigurable systems utilising these control components, as well as hemocompatible fluid actuation mechanisms. This ongoing work is intended to realise a blood function assay, resulting in systems building on the outcomes of this thesis to provide a complex multilayer microfluidic system capable of processing and performing blood function assays on whole human blood. This work is planned for publication in late 2018 or early 2019, and as such is not explored within the scope of this thesis.

Overall, this chapter highlights that platforms fabricated with the technique outlined in chapter 2, are well suited to handling complex biological fluids. This indicates that it is possible to rapidly fabricate components suited to sophisticated fluidic manipulation with exceedingly complex biological fluids, with the level of reproducibility, and in numbers sufficient to gather statistically significant data from a battery of bioassays. This work outlines design considerations for modular control components, capable of manipulating blood samples, which could be applied to numerous point-of-care, or research applications.

The work related to this chapter has been peer-reviewed and published in: ***Lab on a chip***

The paper can be obtained via the DOI: 10.1039/C7LC01320E [32]

My role in this work was to conceive, design and fabricate microfluidic systems. I was involved in experimental design, performed initial mechanical characterisation experiments, assisted with initial bio-experiments and assisted with analysis of results, including coordination of several different multidisciplinary groups. I assisted with writing the manuscript and contributed several figures. This work was heavily multidisciplinary, with mechanical engineering components, seen in the computational fluid dynamics, and microparticle image velocimetry. Electronic and microsystems engineering components are seen in the device design and fabrication, and creation of support equipment such as the valve driver and computer interfaces. Cell biology and clinical biomedical components were critical in the comprehensive battery of hemocompatibility assays. My leading role in this research was shared with another PhD student, in the field of medicine and biology. We worked closely together to facilitate this highly collaborative and multidisciplinary work, and this is reflected in us both being listed as co-first authors.

Elastomeric microvalve geometry affects haemocompatibility†

Crispin Szydzik,‡[a] Rose J. Brazilek,‡[b] Khashayar Khoshmanesh, [iD][a]
Farzan Akbaridoust,[c] Markus Knoerzer,[a] Peter Thurgood, [iD][a] Ineke Muir,[d]
Ivan Marusic,[c] Harshal Nandurkar,[b] Arnan Mitchell[a] and Warwick S. Nesbitt [iD]*[ab]

This paper reports on the parameters that determine the haemocompatibility of elastomeric microvalves for blood handling in microfluidic systems. Using a comprehensive investigation of blood function, we describe a hierarchy of haemocompatibility as a function of microvalve geometry and identify a "normally-closed" v-gate pneumatic microvalve design that minimally affects blood plasma fibrinogen and von Willebrand factor composition, minimises effects on erythrocyte structure and function, and limits effects on platelet activation and aggregation, while facilitating rapid switching control for blood sample delivery. We propose that the haemodynamic profile of valve gate geometries is a significant determinant of platelet-dependent biofouling and haemocompatibility. Overall our findings suggest that modification of microvalve gate geometry and consequently haemodynamic profile can improve haemocompatibility, while minimising the requirement for chemical or protein modification of microfluidic surfaces. This biological insight and approach may be harnessed to inform future haemocompatible microfluidic valve and component design, and is an advance towards lab-on-chip automation for blood based diagnostic systems.

Introduction

There is an increasing drive toward microfluidic based blood diagnostics,[1–5] however a critical bottleneck impeding clinical translation of such devices is the ability to reliably deliver blood components to assay platforms without affecting blood composition or function.[6,7] Microfluidic performance in areas such as the mechanics of blood cell handling, effects on blood plasma protein and biomarker composition, materials haemocompatibility, and haemodynamic parameters, must be carefully considered in order to achieve effective blood handling. On-chip microvalve operated delivery, mixing, and pumping elements have the potential to deliver sophisticated, multiplexed, automated, and reliable haematology focused microfluidic diagnostics; however the effect of such dynamic

microfluidic components on blood function presents significant challenges. While haemocompatibility is a recognized criterion for microfluidic development, design approaches have been limited by a lack of sophistication with respect to the assessment of blood function, and have often relied on superficial measures such as haemolysis, and gross assessment of biofouling.[8,9] Few microfluidic studies have comprehensively defined haemocompatibility and virtually none describe a detailed blood-testing regime to assess and inform microfluidic device design.[10–14]

Blood presents significant and specific challenges when working with microfluidic systems.[6,15] Blood is a non-Newtonian fluid and its viscosity may be up to an order of magnitude more viscous than water (dependent on flow parameters and biochemical factors), leading to pressure differentials that may perturb flow and impair device performance.[16,17] In addition, blood plasma protein physisorption processes at microfluidic surfaces pose significant problems with regard to blood analyte (biomarker) loss, and blood cell adhesion.[15] The plasma protein and cellular components of blood, particularly von Willebrand factor (VWF), fibrinogen, and blood platelets, have evolved to react to local changes in the hydrodynamic (haemodynamic) environment through processes of protein conformational unfolding, surface adhesion and platelet–platelet aggregation.[18] VWF binding and function is critically sensitive to the prevailing

[a] *School of Engineering, RMIT University, 124 La Trobe Street, Melbourne, Victoria 3000, Australia. E-mail: warwick.nesbitt@rmit.edu.au*

[b] *The Australian Centre for Blood Diseases, Monash University, Alfred Medical Research and Educational Precinct, 99 Commercial Road, Melbourne, Victoria, 3004, Australia*

[c] *Department of Mechanical Engineering, University of Melbourne, Grattan Street, Parkville, Melbourne, Victoria 3010, Australia*

[d] *CSL Ltd, CSL Ltd, Bio21 Institute, Flemington Rd, Parkville, VIC 3052, Australia*

† Electronic supplementary information (ESI) available. See DOI: 10.1039/c7lc01320e

‡ These authors contributed equally.

haemodynamic conditions such that shear rates >5000 s^{-1} lead to conformational unfolding and presentation of platelet binding domains.[19–21] Fibrinogen exchange at artificial surfaces is mediated by competition with proteins of the contact activation (coagulation) pathway, such as high-molecular-weight kininogen, factor XII, and plasminogen, with studies demonstrating that sample flow can significantly increase initial adsorption rates and also modify exchange rates with coagulation factors (the Vroman effect).[22–24] Shear rates in relation to platelet function must be carefully considered.[25–27] Elevated shear rates on the order of 1500–$10\,000$ s^{-1} and extremes above $50\,000$ s^{-1} can directly trigger blood platelet Ca^{2+} signalling, α-granule secretion, adhesion, and platelet aggregation through the activation and engagement of platelet adhesion receptors, such as GPIb/V/IX and the integrin $\alpha_{IIb}\beta_3$.[28,29] In addition, platelet adhesion and activation at device surfaces can trigger coagulation through the generation of "coated" procoagulant platelets expressing surface phosphatidyl serine (PS).[30] Significantly, findings from our laboratories have demonstrated that shear rate micro-gradients above a critical threshold can acutely trigger platelet aggregation in microfluidic systems.[31–33]

Pneumatically actuated microvalves are the most common valve type in assays requiring multiplexed integration, as the fabrication processes are comparatively inexpensive and simple.[34] Pneumatic valves may operate through 'normally-open' or 'normally-closed' configurations.[35] Normally-open configurations may be designed for high-density systems, but are only possible with low aspect ratio rounded channels; requiring complex fabrication methods.[36] In addition, normally open valves are limited where portability is a requirement due to the need for bulky ancillary drivers to maintain fluidic isolation.[34] In contrast, normally closed valves are able to overcome these limitations, and generally operate at lower actuation pressures (typical actuation pressures of 1–12 psi) resulting in increased performance and the capability to use relatively small footprint valve drivers.[37] Normally closed lifting gate valves consist of a vertical gate geometry patterned directly onto a membrane that deflects away from the channel floor upon actuation.[34] This valve configuration allows for reliable fluidic isolation and integration with various functional substrates,[31] with recent advances in fabrication techniques by our group significantly reducing fabrication complexity, increasing the practical integration of this valve type.[38] A key consideration for optimised lifting gate valve performance is actuation pressure, with operating pressure range in part determined by overall valve geometry.[35] A hierarchy of valve geometries as a function of actuation pressure and fluidic channel geometry has been defined, such that v-shaped valves demonstrate the lowest actuation pressures in comparison to straight or diagonal valve variants.[35] In addition, v-shaped valves are typically more reliable, as they actuate more consistently, and their actuation pressures are more reproducible across replicate devices.[35] While a number of design principles focused purely on valve mechanical performance have been identified, the specific requirements for haemocompatible blood handling microvalves and the impact of valve haemodynamics on performance have not been investigated.

In this study, we define and describe a biologically informed approach for haemocompatible microfluidic design. Using this approach, we identify a v-shaped microvalve architecture that minimally impacts blood sample integrity and function without the requirement for surface passivation (prefouling).

Experimental

Device description

The overall design of the microvalve iterations tested, the "test-manifolds", and the pneumatic actuation chamber location are shown in Fig. 1a. Valve iterations were identified by the width of the valve chamber (μm) and overall geometry as; S300, S400, S500 and S600 (straight valves) and V300, V400, V500 and V600 (v-shaped valves) (Fig. 1a). Details of valve manifold dimensions are given in Table S1.† Under normal operation sample perfusion through the valve test-manifold was driven *via* an external Harvard PHD-2000 syringe driver, operating in withdraw mode, connected to the outlet channel in the PDMS block using a 30 ml glass syringe attached to 10 cm of Tygon (0.8 mm I.D.) tubing. In the case of FACS based assays or assays requiring perfusate collection, blood samples were loaded into sterile plastic 10 mL syringes prior to device connection and the syringe driver operated in infuse mode. Pneumatic gate operation was achieved by applying negative pressure through connection of a 50 ml plastic syringe to the actuation chambers by 10 cm of Tygon tubing.

Device fabrication

Fabrication of microfluidic devices was achieved using a previously described method.[38] In brief, a combination of a membrane-sandwich fabrication method and PDMS injection moulding, was utilised to produce thin double sided PDMS slabs.[38] Standard photolithography techniques[33] were used to fabricate the required complementary mould structures, using silicon and glass wafer substrates. These moulds consisted of primary fluidic channels and valve gates patterned onto the bottom mould, and pneumatic actuation channels and viaducts on the transparent upper mould. Polydimethylsiloxane (PDMS) pre-polymer (Sylgard 184 Silicone Elastomer – Dow Corning) was mixed with curing agent with a weight ratio of 10:1, and thoroughly degassed under vacuum. Degassed pre-polymer was introduced between the moulds, which were aligned, clamped and cured for 30 min at 100 °C. Following curing, the moulds were separated and the PDMS slab extracted. Interface holes were biopsy punched as required, and a 5 mm thick interface slab of PDMS was plasma bonded to the upper surface of the injection moulded PDMS slab (Harrick Plasma PDC-002: 100% O_2, 1 min). The interface slab, previously biopsy punched with corresponding 750 μm interface holes, acted to seal the pneumatic upper channels while providing the fluidic and
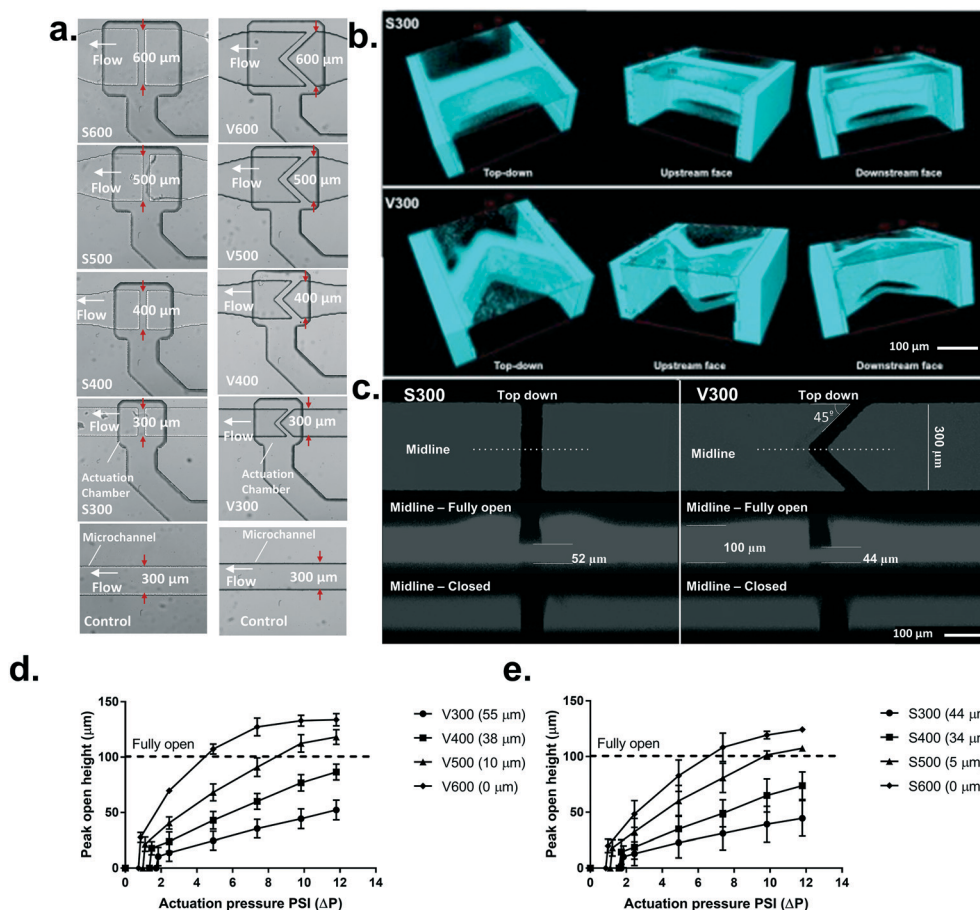
Fig. 1 Test device description and microvalve mechanical testing. a. DIC micro-image showing the straight and v-gate test-manifolds. The microfluidic test-manifolds consisted of five primary fluidic channels; a control (no-valve) channel, and four channels containing lifting-gate valves differing by the width of the valve chamber and channel expansion, including 300 μm, 400 μm, 500 μm and 600 μm. b. Confocal imaging of S300 and V300 microvalves in partially open state following perfusion with TRITC (1 μg mL^{-1}). Views show 3-dimensional reconstructions of S300 and V300 valve cases. Note the overall deformation of the valve gates under negative pressure resulting in microchannel clearance. c. Confocal imaging showing top down and lateral (midline) views of S300 and V300 gates in fully open and closed states. Note that opening heights were taken from the lateral midline. d. Valve opening height (midline) as a function of actuation pressure for v-gate valve manifolds. Numbers in brackets represent gate projection into the microchannel at a maximal actuation pressure of 7.37 psi. e. Valve opening height (midline) as a function of actuation pressure for straight valve manifolds. Numbers in brackets represent gate projection into the microchannel at a maximal actuation pressure of 7.37 psi.

pneumatic interface. A no. 1 borosilicate coverslip sealed the bottom of the injection-moulded slab and acted as the imaging window for microscopy-based experiments. Selective plasma bonding was achieved in a manner similar to those previously described for normally closed PDMS microvalves. In order to selectively prevent permanent plasma bonding of the valve gates, PDMS exclusion stamps were fabricated using photolithography to define a block with raised 150 μm tall pillars with geometry to match the location and size of all valve gates on the bottom of the injection moulded PDMS slab.[39] This exclusion stamp is aligned and placed over the valve gates prior to plasma treatment (100% O_2, 20 seconds) and allows plasma access to all PDMS surfaces with exception of the areas in contact with the exclusion stamp.

Computational fluid dynamic analysis

To conduct CFD analysis at the actuated microvalve assembly, the valve and microfluidic geometry were simplified and reconstructed from 3-dimensional confocal imaging data of valve assemblies perfused with TRITC (1 μg mL^{-1}) in mQ H_2O. Confocal images were exported as StereoLithograpy (stl) files using the open source software Fiji. The stl file was further optimized using surface reconstruction algorithms in MeshLab. Simplified reconstructions of the open valve geometry were then constructed based on these optimized stl files, using the CAD software, Solidworks (Dassault Systèmes). The mesh was constructed using snappyhexmesh resulting in a total of 16 136 cells (12 340 hexahedra and 3796 polyhedra). Grid convergence analysis was performed at the valve gate wall, using centerline flow profiles (Fig. S2†). To determine the local shear rate conditions for human whole blood at the micro-valve structure the Navier Stokes equations over the geometry domain were solved using OpenFOAM and SIMPLE algorithm, using a viscosity of 0.00345 Pa s and a density of 1050 kg m^{-3}. Blood can be approximated as Newtonian fluid at high shear rates.[39] Non-slip at the wall was considered.

µPIV analysis

µPIV analysis was performed in order to verify and support CFD models. Detailed methodology is supplied in ESI.†

High speed platelet imaging

Washed platelets (200×10^9/L) were loaded with $DiOC_6$ (2 µg ml^{-1}) for 10 min at 37 °C. Dye-loaded platelets (final platelet count = 200×10^9/L) were then reconstituted with isolated RBC prior to perfusion through the device. Platelet adhesion and activation were blocked with theophylline (10 mM) and eptifibatide (Integrilin-20 µg mL^{-1}). Reconstituted blood samples were perfused across the valve surface at a rate of 24 µl min^{-1} for 16 s. Epifluorescence ($488_{ex}/510_{em}$) images were acquired at 1100 fps (1280×1024) using a Phantom v1610 (Vision Research) CMOS camera attached to an Olympus IX83 microscope (UPLSAPO 60×/NA1.260 obj) with Spectra 4 light source. Images were compiled as maximum z-projections off-line in ImageJ.

Blood collection and handling

Ethics approval was obtained from the Alfred Hospital and Monash University Standing Committees on Ethics in Research involving Humans. All experiments were performed in compliance with relevant laws and guidelines and followed Monash Universities policies regarding the handling of human blood samples. Whole blood samples were obtained from consenting subjects *via* venesection into 2% w/v citrate. Samples were allowed to rest for 10 min at 37 °C prior to device perfusion. Full blood examination was routinely conducted using a Haemogram (Abbott Diagnostics) blood analyser prior to experimentation and blood haematocrit and platelet count recorded.

Assessment of valve dependent platelet aggregation

To assess platelet aggregation as a function of valve architecture human whole blood samples were incubated with the lipophilic membrane dye $DiOC_6$ (1 µg mL^{-1}) (Molecular Probes) and 0.02 U mL^{-1} apyrase (to eliminate released ADP during blood collection) for 10 min at 37 °C and subsequently perfused through the device at constant flow rates of 24 or 108 µL min^{-1}. Blood perfusion and platelet aggregation dynamics were acquired on an inverted Nikon TiU microscope (Nikon Plan Fluor 20×/0.50 objective) using an Andor Zyla sCMOS camera at 1 fps for 210 s. All image analysis was performed off-line in ImageJ using Huang's fuzzy image thresholding. $DiOC_6$ labelled fluorescent platelet aggregates were auto-thresholded such that the earliest micro-aggregates were included in the analysis window. Platelet aggregate size was expressed as either 2-dimensional cross section (µm^2) or integrated intensity as a function of time (s).

Platelet isolation

Washed human platelets were isolated from human whole blood as described.[40] Whole blood was collected into acid citrate dextrose (ACD) anticoagulant at a ratio of 6:1 (blood/ACD), to which 20 U ml^{-1} enoxaparin (Clexane) was added before being allowed to incubate at 37 °C for 15 min. Separation of platelet-rich plasma (PRP) and red blood cells (RBC) was achieved by centrifugation at $300 \times g$ for 16 min. Platelets were isolated from PRP by centrifugation at $1700 \times g$ for 7 min, followed by resuspension in an equal volume of platelet washing buffer (4.3 mM K_2HPO_4, 4.3 mM Na_2HPO_4, 24.3 mM NaH_2PO_4, 113 mM NaCl, 5.5 mMD-glucose, and 10 mM theophylline, pH 6.5). Platelets were washed by centrifugation at $1500 \times g$ for 7 min, followed by a final resuspension at a concentration of 200×10^9/ml in Tyrode's buffer (10 mM Hepes, 12 mM $NaHCO_3$, 137 mM NaCl, 2.7 mM KCl, and 5 mM glucose, pH 7.3) containing bovine serum albumin (5 mg ml^{-1}), calcium (1 mM), and apyrase (0.02 units per ml) (ADPase activity).

Reconstituted blood sample preparation

Reconstituted blood was prepared from human whole blood as described.[40,41] RBC were isolated by centrifugation at $200 \times g$ for 15 minutes, and the PRP fraction collected. The remaining RBC fraction was washed 2× with Tyrode's buffer pH 7.2 *via* centrifugation at $1700 \times g$ for 7 minutes. The final RBC fraction was re-suspended in Tyrodes pH 7.2 supplemented with 0.5% w/v BSA + apyrase (0.02 U mL^{-1}) and carried through a final centrifugation at $1700 \times g$ for 7 minutes. Packed RBC were stored at 37 °C for later use. Reconstituted blood samples were prepared using either isolated platelet suspensions in Tyrodes buffer pH 7.2 or autologous PRP at a final haematocrit (Hct) of 40% and a platelet count of 200×10^9/L. Hct and platelet counts were verified by full blood analysis.

Platelet and erythrocyte Ca^{2+} assay

Platelet cytosolic calcium levels $[Ca^{2+}]_c$ were monitored according to published methods.[40] Briefly, washed platelets (1×10^9/mL) were loaded with Oregon Green BAPTA 488 1,2-bis (2-aminophenoxy)ethane-N,N,N',N'-tetraacetic acid tetra(acetoxymethyl) ester (1 µM), and Fura-Red/AM (1.25 µM) for 30 min at 37 °C. Dye-loaded platelets (final platelet count = 200×10^9/L) were then reconstituted with washed red blood cells prior to perfusion through the device. Reconstituted blood samples were perfused through the test-manifold at Q = 24 or 108 µL min^{-1}.

RBC used for monitoring intracellular calcium changes in response to shear stress were washed with modified Tyrodes pH 7.2 + 2 mM $CaCl_2$ and 10 mmol l^{-1} glucose then resuspended in this buffer at a haematocrit of 0.002%. Fluo-4/AM dissolved at 2 mM in dimethyl sulfoxide was added to the RBC suspensions to obtain 3 µM and the suspensions were incubated with mild shaking for 1 hour at 37 °C. RBC were washed three times with supplemented Tyrodes following the incubation period and then suspended in supplemented Tyrodes. To examine changes in calcium flux, sequential confocal images of platelets or RBC were captured at a scan rate of 0.586 frames per s for 37.5 s over the 3.5 min perfusion time course at positions upstream, at the valve, immediately downstream and 1000 µm downstream of the valve structure. Standard image thresholding was used to demarcate RBC or platelets from the background and determine calcium dye

fluorescence. In the case of RBC Fluo4 fluorescence was monitored and fluorescence change normalised against resting (no perfusion) controls. In the case of platelets, the fluorescent ratio of Oregon Green BAPTA 488 to Fura Red was then calculated. Real time platelet calcium flux was calculated from ratiometric fluorescence measurements and converted to intracellular calcium concentrations (nM) as described previously.[42]

Haemolysis assay

Whole blood samples in 3.2% ACD collected following perfusion through the valve test platform were centrifuged at 500 × g for 5 minutes, and the resulting supernatant collected. The supernatant was subsequently centrifuged at 500 × g for 5 minutes, to pellet any intact RBC. 15 μL of each supernatant was then suspended in 185 μl 1% Tyrodes (4.3 mM K_2HPO_4, 4.3 mM Na_2HPO_4, 24.3 mM NaH_2PO_4, 113 mM NaCl, 5.5 mM D-glucose, pH 7.2) at 35 °C. A positive control was made by adding 15 μL of non-haemolysed haematocrit and 10 μl Triton X-100 to 185 μl of Tyrodes buffer. A negative control consisted of the collected supernatant of an unprocessed sample. 100 μl of each sample was then transferred to a clear, flat-bottomed 96-well plate and absorbance (495 nm) was measured. Background correction was determined from the average absorbance of the negative control samples. All samples were normalised with the positive control representing 100% haemolysis.

Plasma protein assay

To assess plasma VWF loss as a function of valve performance whole blood samples (500 μL) in 3.2% ACD were collected following perfusion through the valve test platform(s). Blood samples were centrifuged at 2000 × g for 2 min and the plasma fraction retained. Plasma VWF antigen (%) was determined *via* von Willebrand factor ELISA (Helena laboratories) as per the manufacturers instructions. To determine the effect of valve architecture on VWF multimer profile samples were collected as per ELISA and subsequently run on an agarose multimer gel and multimer range assessed *via* densitometry.

Erythrocyte and platelet FACS analysis

Whole blood samples in 3.2% ACD following perfusion through the valve test platform were collected. 5 μl samples from each valve iteration were immediately transferred to 12 × 75 mm Falcon® capped polystyrene test tubes containing 20 μL CD61 PerCP, 20 μL PAC-1 FITC or 5 μL PE-P selectin conjugated monoclonal antibodies. Tubes containing only one of each antibody were prepared using inactivated blood to act as voltages, tubes containing blood activated with 2 × 10^{-5} M ADP were used for channel compensation, and tubes stained only with CD-61 were used to obtain isotype control forward and side scatter buffers. For all samples containing PAC-1 antibodies, RGDS was also added to the solution to exclude non-specific binding. Data was then analysed in two-colour plots.

Statistical analysis

Statistical analysis was performed in GraphPad Prism using a one-way analysis of variance (ANOVA) with Dunnett's multiple comparisons test to compare means and determine significance.

Multiple regression analysis was performed using SPSS statistics. All variables were coded as continuous except the valve type, which was coded as an ordinal variable. Continuous results were assumed to have a normal distribution (using a normal probability plot), linearity (using a residual plot) and constant variability (using a scatter plot). All variables were entered into the analysis. The R^2 for this multivariate analysis was 0.780, showing the regression explained 78.0% of the variance in the data. F-Test demonstrated a high degree of significance (F = 116.218), allowing the assumption that the model explained a significant degree of variation in the data. All groups demonstrated statistical significance ($p < 0.05$). Non-multicollinearity was confirmed. Standardised coefficients were compared to determine the impact of variables.

Results

Valve gate mechanical performance

To characterise micro-valve performance as a function of actuation pressure we conducted scanning confocal microscopy experiments in which valve manifolds were perfused with a tetramethylrhodamine (TRITC) solution (1 μg mL^{-1}) and valve opening recorded in 3-dimensions (Fig. 1b and c; Video S1†). Fig. 1b and c demonstrate that application of negative pressure in the actuation chamber results in the upward deformation and expansion of the actuation membrane, lifting and asymmetrically stretching the valve gates resulting in an "arched" opening profile. Valve opening efficiency (measured at mid-line) as a function of actuation pressure directly correlated with valve geometry such that S600 and V600 valves demonstrated the greatest opening efficiency, with full gate clearance (100 μm) occurring at an actuation pressure of ≃4.9 psi (Fig. 1d and e). Significantly, overall valve chamber width appeared to be a direct effector of opening efficiency, with valves in the range of 300–500 μm only partially opening at an applied pressure of ~4.9 psi (Fig. 1d and e). It should be noted by the standard deviation that valve-to-valve variance was evident due both to batch-to-batch differences in fabrication and also the inherent tolerances of PDMS based elastomeric micro-valves. Head-to-head comparison of straight *versus* v-shaped valves demonstrated that the v-shaped design more reliably actuated at low pressures, with the v-shaped design displaying a lower overall minimum actuation pressure (Fig. 1d and e). Furthermore, as evidenced by the variance in replicate measurements the v-gate geometry typically actuated more consistently across the applied pressure range (Fig. 1d and e). Confocal imaging demonstrated that at an opening pressure of −7.37 psi the 300–500 μm wide valve gates projected up to ~5–55 μm into the microfluidic channel, increasing the likelihood of valve gate interactions with perfused blood components (Fig. 1d and e).

Effect of valve architecture on platelet aggregation and fouling

A key problem associated with microfluidic blood handling performance is fouling due to adhesion and/or aggregation of blood cells, particularly platelets, with component systems. To investigate the effects of valve architecture on platelet adhesion and aggregation we perfused both straight and v-shaped test-manifolds with citrated whole blood for up to 5 minutes. Fig. 2a and b demonstrate that for fully open and partially open states, platelet aggregation inversely correlates with valve gate size, such that 300 μm valves show the highest levels of platelet adhesion/aggregation. Head-to-head comparison of straight *versus* v-shaped valves demonstrated that straight valves are significantly more pro-aggregatory than v-shaped in fully open and partially open (40 μm) states (Fig. 2a and b). The V600 geometry demonstrated limited platelet adhesion/aggregation above that observed for no-valve controls in the fully open state (Fig. 2a). Epifluorescence imaging of the early platelet adhesion response demonstrated that platelet aggregation was initiated at the upstream edge and bottom face of valve gates (Video S2†). Furthermore, early aggregates formed as distinct "platelet strings" that in the case of straight gates were distributed across the entire bottom face (Video S3†). In the case of v-gates, "platelet strings" formed lateral to the v-gate apex, which was free of formed aggregates (Video S2†).

3-Dimensional confocal imaging of platelet recruitment at the valve gate geometries following prolonged (5 min) blood perfusion demonstrated that platelet fouling was localised primarily at the bottom face of the valve gates with consolidated aggregates extending freely away from both the upstream and downstream faces (Fig. 2d–g). Quantitation of the time to complete fouling in the fully open and 40 μm states demonstrated that straight valve designs were more prone to occlusion as a function of valve size compared to v-gates (Fig. 2c). A 5-fold increase in flow rate ($Q = 128$ μL min^{-1}) led to an approximate doubling in overall platelet aggregation at the v-gates across the size range tested (Fig. 3a and S3a†). Increasing haematocrit (Hct) from 40–60% led to an overall increase in platelet aggregation dependent on geometry and inversely with valve size (Fig. 3b and S3b†). Increasing platelet count led to an overall increase in platelet aggregation that scaled inversely with valve size (Fig. 3c and S3c†). Taken together these data suggest that, as for laminar flow systems, platelet margination (increased density at the wall) and mass transport effects due to red blood cell interactions may contribute to the aggregation response. There was no effect of anticoagulant (citrate *versus* hirudin) on the observed platelet response (Fig. S4†). Multivariate regression to predict aggregate size from; valve geometry (categorical), and open state, valve size, Hct, platelet count, and flow rate (continuous) demonstrated that all variables statistically significantly
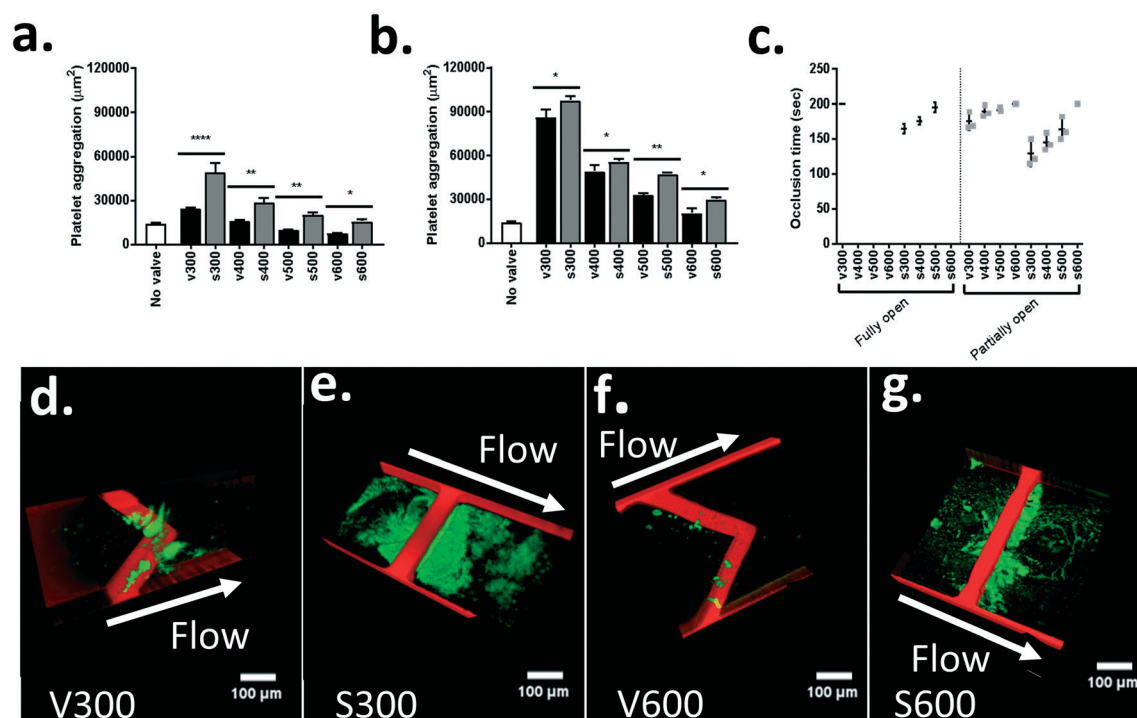

Fig. 2 Platelet aggregation and biofouling as a function of microvalve geometry. a. Platelet aggregation at straight *versus* v-gates in fully open states; $Q = 24$ μl min^{-1}. b. Platelet aggregation at straight *versus* v-gates in partially open (40 μm) states; at $Q = 24$ μl min^{-1}. Black horizontal bars indicate comparative valve shapes and sizes (*e.g.* V300 and S300) for which a significance significant difference was tested for using a paired *t*-test. * $p \leq 0.05$, ** $p \leq 0.01$, *** $p \leq 0.001$, **** $p \leq 0.0001$. c. Occlusion times of straight *versus* v-gates in fully open or partially open (40 μm) states; $Q = 24$ μl min^{-1}. d–g. 3-Dimensional reconstructions of confocal microscopy epifluorescence images of representative aggregate formation, imaged after 5 minutes of blood flow. Aggregates are represented in green and the valve geometries in red. Scale bar represents 100 μm. d. V300 partially open valve with aggregate. e. S300 partially open valve with aggregate. f. V600 partially open valve with aggregate. g. S600 partially open valve with aggregate.
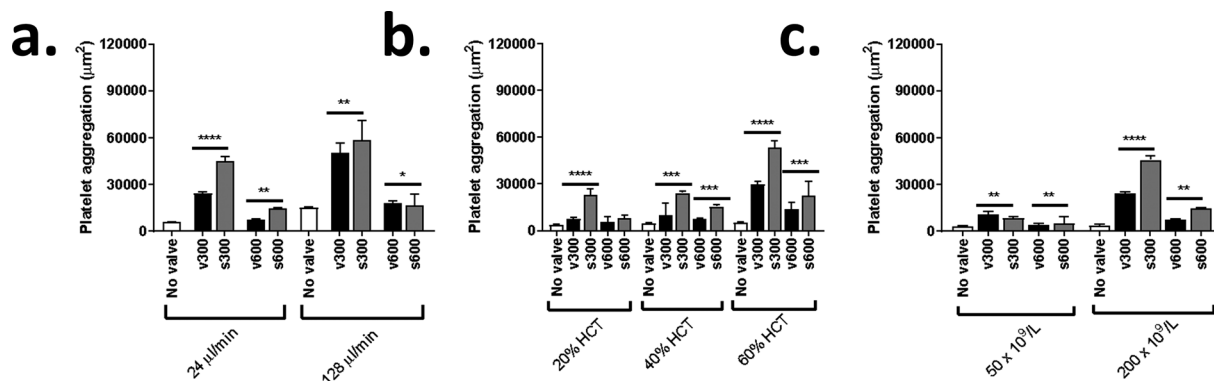
Fig. 3 Platelet aggregation in bulk flow as a function of microvalve geometry. a. Platelet aggregation at straight *versus* v-fully open gates at $Q = 24$ $\mu l\ min^{-1}$ and $128\ \mu l\ min^{-1}$. b. Platelet aggregation at straight *versus* v-fully open gates ($Q = 24\ \mu l\ min^{-1}$) as a function of hematocrit. c. Platelet aggregation at straight *versus* v-fully open gates ($Q = 24\ \mu l\ min^{-1}$) as a function of platelet count. All data shows $n = 3$ independent experiments normalized to valve surface area (μm^2). Error bars indicate standard deviation. Black horizontal bars indicate comparative valve shapes and sizes (*e.g.* V300 and S300) for which a significance significant difference was tested for using a paired *t*-test. * $p \leq 0.05$, ** $p \leq 0.01$, *** $p \leq 0.001$, **** $p \leq 0.0001$.

affected aggregate size [$F(7,236) = 79.593$, $p < 0.05$, $R^2 = 0.780$] (Table S2†). This analysis demonstrated that valve category was a significant effector of haemocompatibility (Table S2†) ($\beta = 1.041$ for straight valves, 0.750 for v-shaped valves). Taken together this data suggests that near wall platelet adhesion and aggregation and hence fouling can be significantly modulated by changes in valve geometry.

Effect of valve architecture on platelet activation

An important consideration for microvalve performance is the effect that valve haemodynamics have on platelet activation in bulk flow, particularly where downstream cell and biomarker assay are required. To investigate the impact of micro-valve design on platelet activation we examined the impact of valve architecture on platelet Ca^{2+} signal transduction in bulk flow (Fig. 4a and S5a†). Maximal platelet $[Ca^{2+}]_c$ (a

global marker of platelet activation status) inversely correlated with valve size, with the straight valve architecture more reactive than v-shaped, in both fully open and partially open (40 μm) states (Fig. 4a and S5a†). Fig. 4b–d (Fig. S5b–d†) demonstrate that as per platelet $[Ca^{2+}]_c$ distinct markers of platelet function; platelet integrin $\alpha_{IIb}\beta_3$ activation (PAC1 binding), α-granule secretion (P-selectin expression), and platelet procoagulant function (phosphatidyl serine exposure) mapped to valve size and shape, suggesting that global platelet function in the bulk flow is significantly affected by valve geometry.

Effect of valve architecture on blood plasma VWF and fibrinogen

Platelet adhesion and aggregation is critically driven by the shear dependent binding and unfolding of plasma VWF and
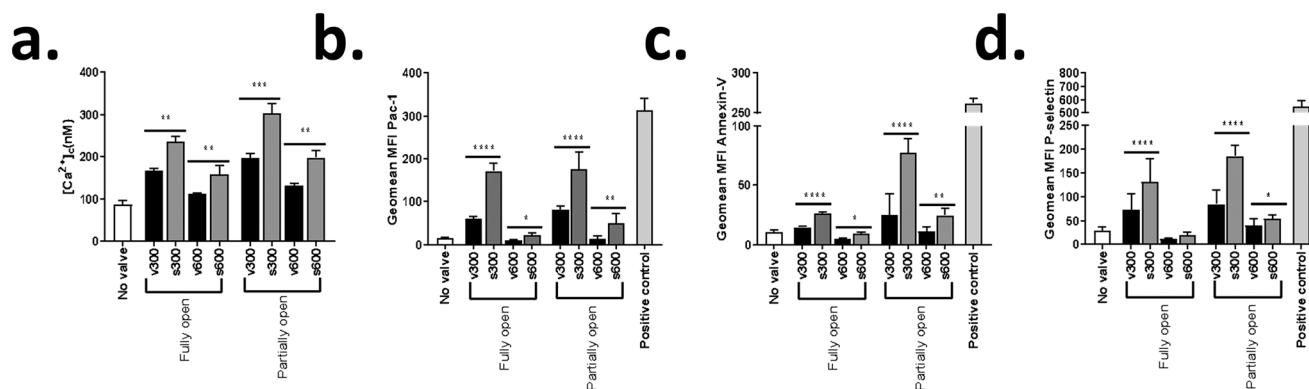

Fig. 4 Platelet activation in bulk flow as a function of microvalve geometry. a. Maximal platelet cytosolic calcium flux $[Ca^{2+}]_c$ (nm) under perfusion at $Q = 24\ \mu l\ min^{-1}$ in the fully open and partially open (40 μm) states ($n = 3$ independent experiments). b. Fluorescence activated cell sorting (FACS) analysis showing mean fluorescence intensity (MFI) geomean distribution of FIT-C PAC-1 antibody binding (integrin $\alpha_{iib}\beta_3$ activation) to platelets in human whole blood following perfusion through V300, S300, V600 and S600 gates ($Q = 24\ \mu l\ min^{-1}$) in the fully open and partially open (40 μm) states. c. FACS analysis showing MFI geomean distribution of FITC-annexin-v binding to platelets in human whole blood following perfusion through V300, S300, V600 and S600 gates ($Q = 24\ \mu l\ min^{-1}$) in the fully open and partially open (40 μm) states. d. FACS analysis showing MFI geomean distribution of expression of P-selectin antibody binding to platelets in human whole blood following perfusion through V300, S300, V600 and S600 gates ($Q = 24\ \mu l\ min^{-1}$) in the fully open and partially open (40 μm) states. All data indicates $n = 3$ independent experiments normalized to valve surface area. Error bars indicate standard deviation. Black horizontal bars indicate comparative valve shapes and sizes (*e.g.* V300 and S300) for which a significance significant difference was tested for using a paired *t*-test. * $p \leq 0.05$, ** $p \leq 0.01$, *** $p \leq 0.001$, **** $p \leq 0.0001$.

the surface immobilisation of fibrinogen.[42] To investigate the effect of valve design on plasma VWF and fibrinogen, valve test manifolds were perfused with whole blood or platelet poor plasma (PPP) and VWF or fibrinogen concentration in the flow-through assessed pre- and post-perfusion. Fig. 5a demonstrates that perfusate VWF antigen loss directly correlated with valve gate size, such that the 300 μm valves show the highest levels of loss. Head-to-head comparison of straight *versus* v-shaped valves demonstrated that straight valve designs led to significantly more VWF loss than v-shaped (Fig. 5a). VWF multimer analysis demonstrated no preferential loss of higher molecular weight multimers (data not shown). PPP experiments demonstrated that VWF loss was not dependent on the presence or absence of platelets or erythrocytes (Fig. 5a). Fig. 5b demonstrates that while perfusate fibrinogen loss did not correlate with valve gate size, loss was significantly greater (∼2-fold) for straight valve geometries in comparison to v-gate. Treatment of the valve test manifolds with BSA to block the PDMS surface completely blocked both VWF antigen and fibrinogen loss demonstrating that both are driven by competitive surface physisorption mechanisms (Fig. 5a and b).

Effect of valve architecture on erythrocyte handling

Erythrocyte (red blood cell – RBC) stability in the context of microfluidic systems is critical, particularly where platelet assays are concerned, due to the propensity of RBC's to secrete potent platelet activators such as ADP and ATP upon mechanical activation and haemolysis. Subtle changes in RBC $[Ca^{2+}]_c$ and PS exposure have been demonstrated to correlate with increasing RBC mechanical fragility and overall reduction in RBC deformability.[43] To investigate the overall mechanical stability of RBCs as a function of valve design, isolated RBC at a Hct = 40% were perfused through the test manifolds and haemolysis assessed for an actuation duty cycle of 1 Hz over 200 s. Fig. 6a demonstrates that the straight valve design

shows poorer RBC mechanical handling, while v-shaped designs demonstrated no increase in haemolysis over no-valve controls. Increasing the overall size of the straight valve case completely eliminated valve-dependent haemolysis (Fig. 6a). RBC echinocyte formation was inversely correlated with valve size, with v-shaped valves displaying less echinocyte formation in comparison to straight valves (Fig. 6b). Fig. 6c demonstrates a marginal but significant increase in RBC $[Ca^{2+}]_c$ that was gate-size dependent, with the S300 valve in the 40 μm open state showing a significant increase in RBC $[Ca^{2+}]_c$ in comparison to the V300 case. Measurement of correlated RBC PS exposure demonstrated RBC procoagulant function is dependent on valve geometry and size, with the S300 gate at 40 μm opening showing a significant increase in RBC PS expression (Fig. 6d). Taken together this data demonstrates that RBC mechanical stability and activation status is sensitive to valve gate architecture and overall valve size; significantly v-shaped valves were superior across the tested size range.

Valve geometry effects predicted blood shear rate exposure

Previously published studies from our laboratories and others demonstrate that shear rate (both peak shear rate and potentially shear rate gradients) significantly affect blood platelet function and VWF structure, particularly at microfluidic step geometries.[31–33] Based on our blood assay findings we therefore hypothesised that shear rate magnitude (both at the wall and bulk flow) and/or shear rate gradients may play a role in determining the observed effects on blood function. To examine this hypothesis while isolating the variables of microvalve geometry from opening height we conducted a series of computational fluid dynamic (CFD) simulations in which gate-opening height was fixed at 40 μm. Valve mesh generation for CFD was derived from simplified 3-dimensional reconstructions of confocal imaging data (see
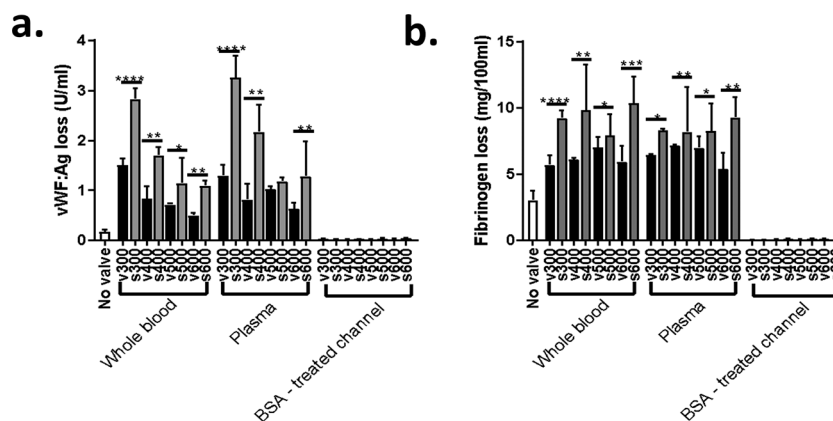

Fig. 5 Plasma protein physisorption and composition as a function of microvalve geometry. a. VWF antigen activity loss (μ ml^{-1}) in whole blood and PPP samples following perfusion through valve manifolds at 24 μl min^{-1}, compared to no-valve control. b. Plasma fibrinogen loss (mg/100 ml) in whole blood and PPP samples following perfusion through the valve manifolds at 24 μl min^{-1}, compared to no-valve controls. All data indicates n = 3 independent experiments normalized to valve surface area. Error bars indicate standard deviation. Black horizontal bars indicate comparative valve shapes and sizes (*e.g.* V300 and S300) for which a significance significant difference was tested for using a paired t-test. * $p \le 0.05$, ** $p \le 0.01$, *** $p \le 0.001$, **** $p \le 0.0001$.
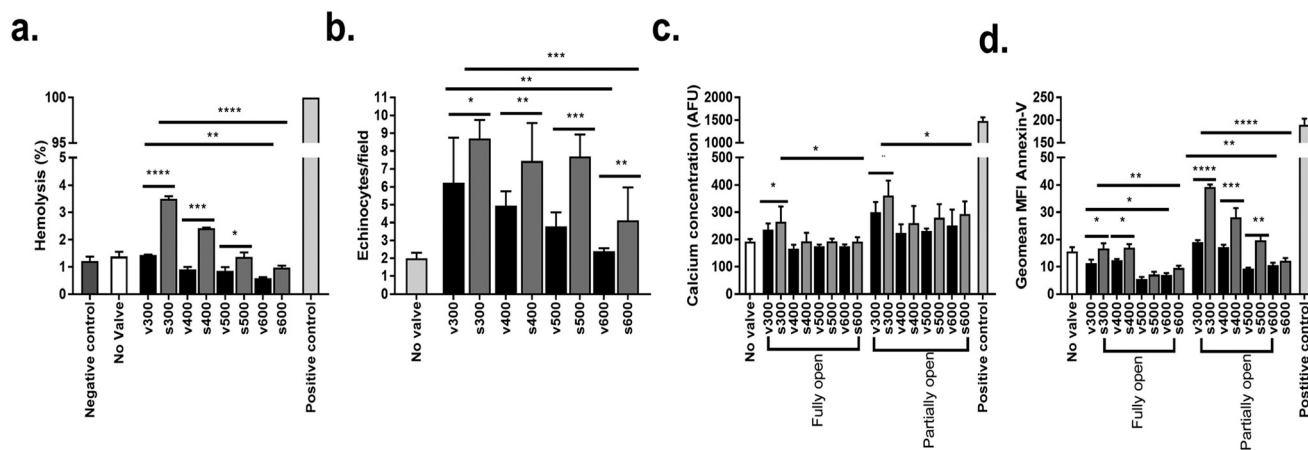
Fig. 6 Erythrocyte mechanical stability and activation as a function of microvalve geometry. a. Erythrocyte (RBC) hemolysis (% of lysed +ve control) for straight and v-shaped valve cases at an opening duty cycle of 1 Hz ($Q = 24$ μl min^{-1}). b. RBC echinocyte formation (total number of echinocytes per field) in blood films taken following isolated RBC (40% Hct) perfusion for V300, S300, V600 and S600 cases in the fully open state ($Q = 24$ μl min^{-1}). c. Maximal RBC cytosolic $[Ca^{2+}]_c$ (arbitrary fluorescence units – AFU) as a function of human whole blood perfusion through valve gates ($Q = 24$ μl min^{-1}) in full open and partially open (40 μm) states. d. FACS analysis showing MFI geomean distribution of FITC-annexin-v binding to isolated RBC (40% Hct) following perfusion through straight and v-gates ($Q = 24$ μl min^{-1}) in the fully open and partially open (40 μm) states. All data indicates $n = 3$ independent experiments normalized to valve surface area. Error bars indicate standard deviation. Black horizontal bars indicate comparative valve shapes (e.g. V300 and S300) for which a significance significant difference was tested for using a paired t-test. Longer error bars at the top of the figure indicate comparative valve sizes (e.g. V300 and V600) for which a significance significant difference was tested for using a paired t-test. * $p \leq 0.05$, ** $p \leq 0.01$, *** $p \leq 0.001$, **** $p \leq 0.0001$.

Methods) and was in part validated using μPIV (Fig. S1a–d†). CFD demonstrated that shear rate contours both at the microvalve gate walls but also within the cross-section of the gate are distinct for straight versus v-shaped valves (Fig. 7a and b and S6a and b†). High wall shear rates (wsr) were found to be distributed relatively uniformly (in the flow direction) across the S300 gate surface (wsr maxima >8750 s^{-1}) [Fig. 7a]. In contrast, v-shaped valves displayed a narrow band of high wsr (>10 000 s^{-1}) only at the upstream edge of the valve gate that rapidly reduced across the gate surface (Fig. 7b). In both cases wsr was reduced where the microvalve gates met the side walls (Fig. 7a and b). Examination of the shear rate contours in cross-section of the gate predicted a relatively larger region of reduced shear rate for the v-gate cases in comparison to straight (Fig. 7a and b insets), suggesting that blood components passing through this region of bulk flow will experience overall lower shear rate exposure at the v-gates in comparison to the straight valve geometry. CFD analysis of 600 μm valve cases showed a similar trend to that of the 300 μm cases but with a reduction in overall wsr and bulk flow shear rate magnitude (Fig. S6a and b†).

Valve geometry effects predicted platelet (particle) trajectories

To model the potential impact of gate geometry on individual platelet trajectories and shear rate exposure, we simulated the trajectories of 15 particles of 2 μm diameter (representative of 2 μm discoid platelets). These particles were released along discrete horizontal planes at incremental distances from the upstream microchannel wall, with particle 1 at the

centreline and particle 15 at the lateral margin (Fig. 7c and d and S6c and d†). Analysis of particle trajectories across the gate geometries with particles released at planes of 40 μm and 3 μm from the gate ceiling suggested a rough equivalence of peak shear rate as a function of height for both straight and v-gate cases (Fig. 7c and d and S6c and d†). However, while trajectories were uniformly distributed across the straight gate at 40 and 3 μm release heights; with some trajectory convergence due to the arched open valve geometry, v-gate cases demonstrated marked divergence of trajectories across the gates at 40 μm and significant convergence at 3 μm (Fig. 7c and d and S6c and d†). This effect was predicted to initiate across the vertical upstream aspect of the v-gates (Fig. 7c and d and S6c and d†). High-speed epifluorescence imaging (see Methods) of platelet trajectories in whole blood ($Q = 24$ μL min^{-1}) at mid-plane (approximately 40 μm) from straight and v-shaped valves supported our CFD modelling results and demonstrated that in the presence of normal Hct, plasma, and cellular components discoid free-flowing platelets display marked divergence across the v-gate surface, in contrast platelet trajectories diverged downstream of the straight gate margin (Fig. 7e and f and S6e and f; Video S4†).

Our CFD modelling results, in conjunction with our platelet adhesion/aggregation experiments, led us to hypothesise that the v-gate geometry may alter platelet trajectories and shear rate exposure over time, increasing haemocompatibility by limiting both the duration of exposure to elevated shear rate and contact with the gate surface. To explore this hypothesis further we extrapolated platelet (particle) shear rates ν time and platelet distribution as a function of z (distance
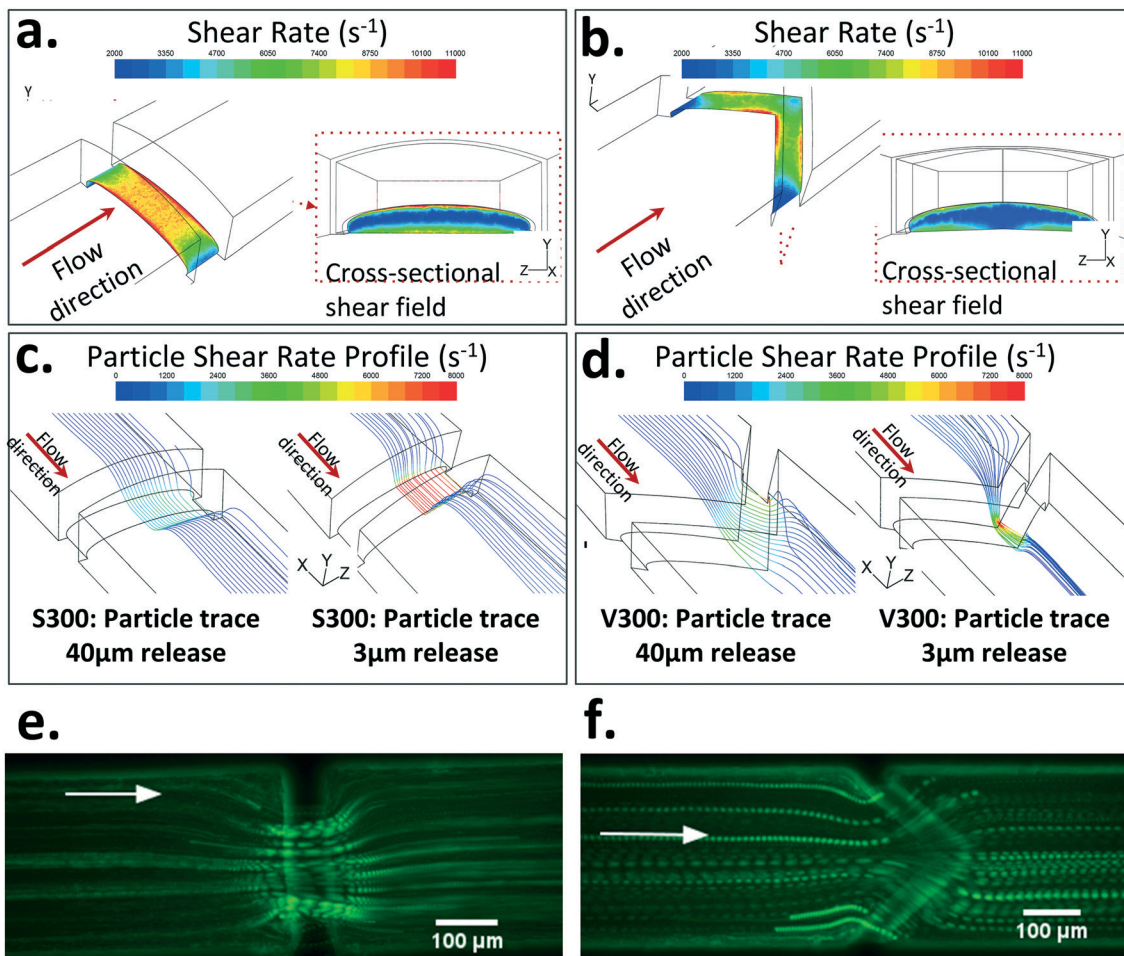
Fig. 7 Computational fluid dynamic (CFD) analyses of 300 μm straight *versus* v-gate geometries. a. 3-Dimensional shear contour profiles of S300 gate geometry at Q = 24 μl min^{-1} and opening height of 40 μm. Note the peaks in shear rate at the upstream and downstream edges of the straight gate and the overall elevation in shear rate across the straight gate surface. b. 3-Dimensional shear contour profiles of V300 gate geometry at Q = 24 μl min^{-1} and opening height of 40 μm. Note the initial peak in shear rate at the midline upstream face of the gate surface and overall reduced shear rates. Note the generation of a low shear rate pocket that extends across the microchannel cross-section. c. Particle shear rate for fifteen 2 μm particles released 40 μm and 3 μm from the microchannel ceiling for the straight gate case. Note the parallel particle trajectories across the gate surface. d. Particle shear rate for fifteen 2 μm particles released 40 μm and 3 μm from the microchannel ceiling for the v-gate case. Note the "funneling" for particles released at 3 μm towards the valve gate midline. Note the loss of funneling at 40 μm from the microchannel ceiling and divergent particle trajectories across the v-gate surface. e. Superimposed image of particle trajectories taken from 16 seconds of flow in partially open S300 valves. f. Superimposed image of particle trajectories taken from 16 seconds of flow in partially open V300 valves.

from the gate surface) for particles released 3 μm from the upstream microfluidic ceiling. Our modelling demonstrated that for two sample particles released (particle 1 at centreline–particle 15 at the lateral margin) the shear rate v time profiles in the straight gate case is relatively symmetric in the flow direction with shear rate peaks at the upstream and downstream edges of the gate surface (Fig. 8a and c and S7a and c†). In contrast, the v-gate cases demonstrated asymmetric shear rate v time profiles with rapid peaks at the upstream gate edge followed by a steady reduction in shear rate across the gate surface (Fig. 8b and d and S7b and d†). This difference was reflected in the shear gradient data (shear rate v time plots) (Fig. 8a–d and S7a–d†). Mapping of platelet aggregate distribution as a function of predicted gate wsr, for straight and v-gate cases, demonstrated a direct correspon-

dence of overall platelet recruitment with shear rate distribution, with peak recruitment occurring towards the centreline for straight gate cases while translated laterally for v-gates (Fig. 8e and f and S7e and f).

To investigate the effect of gate geometry on particle trajectories in the z-plane (relative to the gate surface) we extrapolated particle trajectories from CFD analysis for equidistantly spaced particles released in a horizontal plane 3um from the upstream channel ceiling. Fig. 8g and h demonstrate that for the v-gate cases, particles released 3 μm from the upstream ceiling are displaced between 3–8 μm from the v-gate surface while converging toward the v-gate apex in the x, y, while in the straight gate case particles were predicted to remain 3 μm from the gate surface, with minimal convergence. This indicates that the v-gate geometry may effect
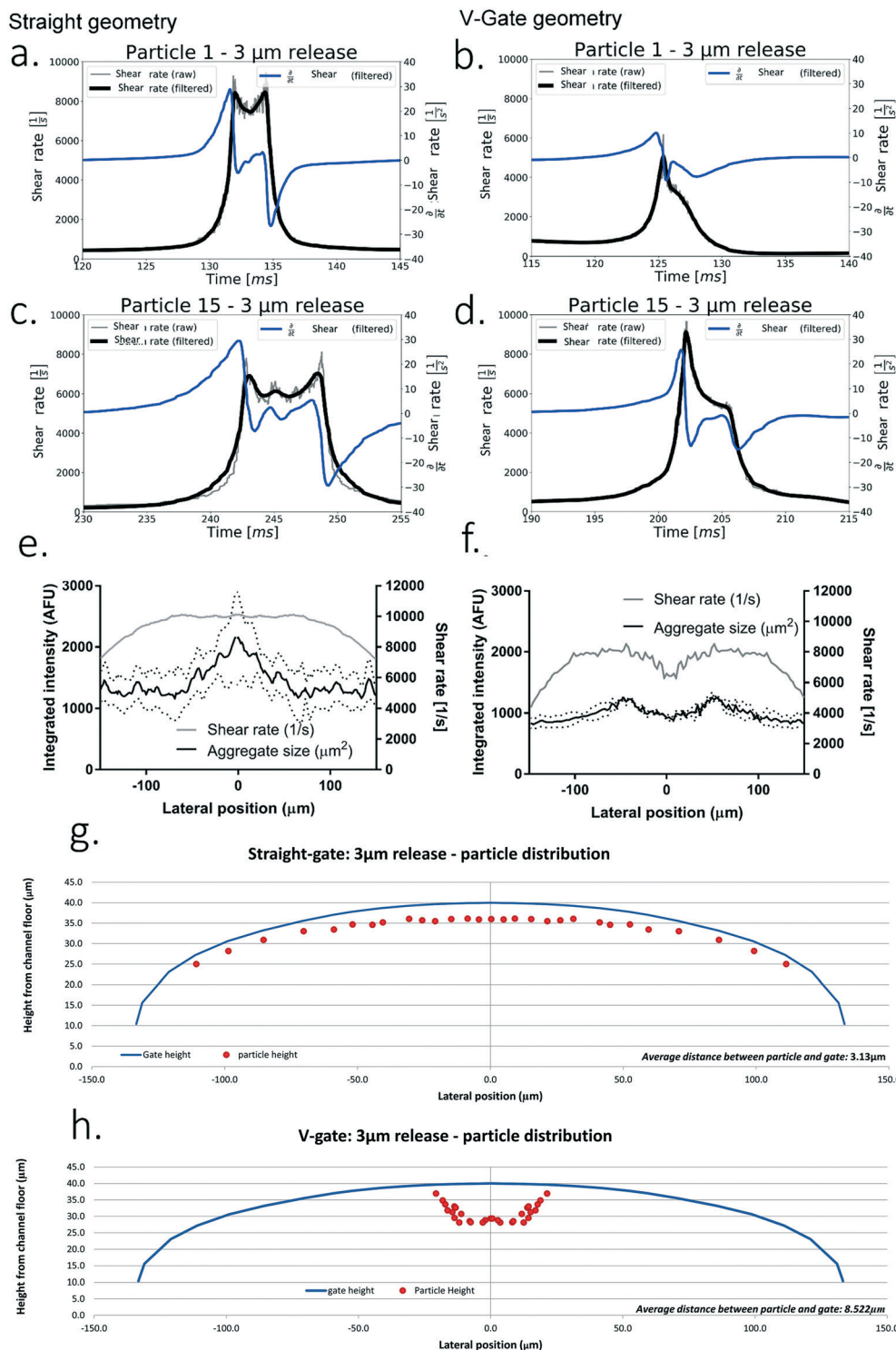
Fig. 8 Shear analyses of 300 μm straight *versus* v-gate geometries. a–d. Particle shear rate (s^{-1}) v time (black line) and shear rate gradient (s^{-1}/s) (blue line) plots for particles released 3 μm from the microchannel ceiling. Particle 1, released at the channel midlines is shown in the straight geometry (a) and v-gate (b), while particle 15, released at the lateral margin, close to the channel sidewall, is shown for the straight geometry in (c) and the v-gate in (d). Note the symmetric shear rate and shear rate gradient profiles for the straight case *versus* the asymmetric distribution and the overall reduction in peak shear rate for the v-gate. Particle 15 in both cases displayed extended shear profiles due to sidewall effects and the overall upward deformation of the valves in the open state. e and f. Plots of maximal platelet aggregation (black line) and wall shear rate (grey line) across the S300 partially open (40 μm) (e) and V300 partially open (f) as a function of distance from the valve midpoint. All data shows *n* = 3 independent experiments. Error bars indicate standard deviation. g and h. Cross sectional particle distribution for particles released 3 μm from the microchannel ceiling, plotting valve open height at a vertical cross-section along the centre of the valve gate (blue) and particle location at this given plane (red dots) for the v-gate (g) and straight valve geometry (h). Note the lateral convergence and vertical displacement away from the gate surface present in the v-gate case, while the straight geometry experiences only minor convergence and particles remain within 3 μm.

overall platelet distribution relative to the gate surface, and therefore the likelihood of platelet-gate surface interactions. Comparison of platelet aggregate distribution as a function of predicted z-position from the gate surfaces (Fig. 8e–h), for straight and v-gate cases, demonstrated an inverse correlation of overall aggregate position with z-displacement, with minimal aggregation occurring at the centreline apex where the predicted z-displacement was highest (Fig. 8e and f).

Discussion

Published findings from our laboratories and others demonstrate that initial platelet aggregation at both *in vivo* and *in vitro* stenosis geometries is initiated by local shear rate gradients and elevated wsr.[31–33] Based on these findings we hypothesised that micro-valve geometry with its impact on the local haemodynamic environment is a key factor contributing to microvalve haemocompatibility. Investigation of platelet surface aggregation and bulk flow activation following blood perfusion through straight and v-gate valve iterations demonstrated that v-shaped valves display less overall platelet activation and aggregation than straight valve architectures. We demonstrate that for either design, the degree of Ca^{2+} flux, α-granule secretion (P-selectin expression), integrin $\alpha_{IIb}\beta_3$ activation, PS exposure, and platelet aggregation are affected by the overall valve geometry. The consistent impact of valve geometry on a range of distinct platelet functional outputs suggests that valve geometry needs to be carefully considered with respect to downstream assay requirements, particularly where specific aspects of platelet function are under investigation.

Confocal imaging following 5 min of blood perfusion demonstrated that gate fouling was the result of consolidated platelet aggregate formation extending both up and downstream of gate surfaces (Video S3†). The propensity of valve gates to undergo fouling appeared to be initiated by, and highly dependent on, the rapid formation of discrete "platelet jets". (Video S3†). Imaging of early stage platelet aggregation at valve gate surfaces demonstrated that fouling initiated at the upstream margins of the gates where acceleration in shear rates were predicted. These observations correlate with previously published observations from our laboratories that have shown that microfluidic step geometries significantly modulate platelet aggregation through the generation of shear gradients that drive discoid platelet to platelet cohesion events.[33] The early stage "platelet jets" observed at valve gate surfaces appear to be composed of strings of tethered platelets reminiscent of observations made by our laboratories and others that have demonstrated that at elevated shear rates, or in the presence of significant shear rate gradients, platelet recruitment is driven by discrete discoid platelet membrane tethering, primarily driven by platelet GP1b/V/IX–VWF binding events and the high shear unfolding and self-association of VWF multimers.[26,32,44] While it is not possible to limit shear rate magnitude at operational gates due to flow restriction during valve closure (under constant pressure conditions), our current findings in conjunction with previously published observations lead us to posit that further modification of the overall shape of the upstream face of gate surfaces (shallower entry angles), changes in the surface profile of the bottom gate surface, and/or improved control of the rate of gate closure and thereby modification of the overall shear rate change, may further reduce or eliminate valve effects on blood platelet function. Exploration of these design concepts, while outside the scope of the current work, is under current investigation.

Our CFD modelling suggests a significant shift in the shear rate distribution across the v-gate surface in comparison to the straight valve case. Specifically, peak wsr was biased at the upstream edge of the v-gate apex; in contrast wsr maxima were distributed relatively uniformly across the straight gate surface. In addition our CFD modelling in conjunction with our platelet flow and adhesion/aggregation studies suggest that platelet path lines diverge across the v-gate surface towards regions of overall lower wsr. Furthermore, our CFD modelling suggests that for the v-gate case platelet trajectories may undergo displacement, away from the gate surface, by up to 2.5× the average discoid platelet diameter (3–8 μm from the gate surface) that may have the additional effect of limiting platelet to v-gate surface interactions during blood perfusion. This limitation on gate surface contact may be a key determinant of the increased haemocompatibility of the v-gate geometry as platelet aggregate formation, and therefore fouling, is critically dependent on the frequency and ability of platelets to interact with surface immobilised adhesive substrates.

Surface passivation through chemical modification or protein blocking of PDMS based microfluidics has been the "go to" method to limit blood dependent fouling. Physisorption of serum albumin, Pluronic block copolymers, or more sophisticated PEGylation and silanization techniques have been used to limit fouling,[45,46] however the efficacy of these approaches is application specific.[47,48] A key limitation of physisorption based blocking techniques is the relatively labile nature of these surface modifications limiting both device reliability and shelf life. Furthermore, while bulk protein physisorption methods may limit some blood-surface interactions in microfluidic systems, surface exchange of protein species such as fibrinogen (the Vroman effect) is still possible, dependent on perfusion rates and exposure times.[23] A chief aim of the present study was therefore to identify a microvalve design that minimises the requirements for surface modification steps (pre-fouling) to achieve haemocompatibility. Our experimental findings in combination with CFD modelling suggest that the haemodynamic profile of valve surfaces may be a significant contributor to both plasma protein adsorption and platelet surface interactions. By controlling both valve gate haemodynamics and therefore surface binding events it may be possible to develop microfluidic blood-handling systems that do not require surface passivation, greatly simplifying the number of device dependent steps and fabrication processes, and improving device shelf life.

Haematology based assays in the microfluidic context require a diverse range of flow rates dependent on assay requirements ranging from rates as low as <1 μl min^{-1} to several ml h^{-1}.[49–54] In the context of devices that require complex switching control, rapid blood sample delivery and flow rates have the potential to minimise sample handling times and increase assay throughput. Relatively high flow rates become increasingly important where relatively high shear rates are required for test development, such as platelet functional assays.[55] In combination with our previously published findings, our data support the concept that upstream microvalved blood handling systems be designed in such a way that they minimise both the overall applied shear rate (at a given flow rate), but also seek to eliminate acute changes in shear rate within valved components.[31] We posit that this may be of particular relevance during microvalve actuation, where dynamically changing valve-gate geometry and therefore haemodynamic profile may significantly impact blood function. In particular, the haemodynamic profile of valve gates under conditions of partial actuation or during opening-closing cycles where gates may transiently project into blood flow is a key consideration. The ability of valve gates to completely clear the microfluidic channel in the fully open state is particularly critical, given our findings that microvalves below a size cut-off of 400 μm^2 may obstruct up to 55% of microchannel height, leading to significant effects on the haemodynamic profile and platelet function, irrespective of gate geometry. This concept is supported by our findings that at a fixed clearance height of 40 μm, where shear rate gradients are acute, all valve types were found to elicit increased levels of platelet aggregation and activation. Critically, valves in the size range from 300–500 μm at a partial opening height of 40 μm experienced complete occlusion over a 200 s time frame, demonstrating that dynamic changes in valve haemodynamics may play a critical role in microfluidic fouling. This may be compounded by the duty cycle of valve opening with repeated closure leading to increased blood sample modification due to the repeated application of transiently high shear rates.

Erythrocytes (RBC) may be damaged during flow in non-physiological environments and under extreme shear stress, such as that generated within microfluidic systems. Shear-induced damage of RBC may result in haemolysis, echinocyte formation (morphology change), or in altered mechanical properties of RBC that in turn reduce their ability to withstand further damage by shear stress.[56,57] Significantly, sub-threshold shear stress that is applied over multiple cycles has been shown to have a cumulative effect on RBC mechanical stability.[58] RBC mechanical stability (haemolysis) and morphology (echinocyte formation) were significantly impacted by valve size and geometry at a duty cycle of 1 Hz. Significantly, v-shaped valves across the tested size range showed no RBC haemolysis above no-valve controls, while for straight valve designs haemolysis correlated inversely with valve size at a duty cycle of 1 Hz. The echinocyte data suggest that RBC deformability and membrane elasticity are significantly influenced by valve geometry. Decrease in RBC deformability, changes of cell volume, increased cellular rigidity, increased levels of haemolysis, and changes in plasma membrane structure, such as phosphatidyl serine exposure correlate with increases in RBC [Ca^{2+}]$_c$.[43,59] Both RBC [Ca^{2+}]$_c$ and PS exposure showed a generalised inverse trend with respect to valve size and geometry. The marginal increase in PS, while not statistically significant, may be problematic where blood coagulant function (contact activation) is a consideration, particularly under conditions where blood samples have not been adequately anti-coagulated. Our findings suggest that a v-shaped valve design is superior as a single pass device, with respect to RBC handling, but may also represent a suitable design for serial valve systems, such as micropumps, where RBC's may experience repeated exposure to elevated shear rates.

A key limitation of this study is the use of an idealised CFD model to describe a complex elastomeric microvalve system and dynamic blood flow effects. The CFD mesh was derived from confocal imaging of operational valves (free of platelet aggregates) in both the partially and fully open (static) states and CFD then carried out on these fixed states. However, it should be noted that this CFD modelling approach is limited by the overall resolution limits of the confocal system and does not account for transient or dynamic deformations of the elastomeric valves during actuation. Furthermore, the CFD modelling carried out in this study does not consider dynamic changes in valve geometry as a result of platelet binding and aggregation events. It is undoubtedly the case that platelet aggregation will feedback on local haemodynamics and modify both peak shear rates and shear rate gradients that are imposed on blood flow. These limitations highlight the critical need for more complex and dynamic non-Newtonian and mechanical CFD models to more accurately inform blood handling microfluidic development in the future. Our interpretation of the overall haemodynamics of valve iterations and the effects on blood interactions therefore need to be qualified with these limitations in mind. Secondly, while we have endeavoured to incorporate a battery of blood based functional assessments to characterise valve performance these assays by no means address all of the complex blood functions that may be important for haemocompatibility. In this context, functional outputs to a large degree need to take into consideration the flow rate requirements of the specific downstream assay in use. Indeed, the flow rate range utilised across the blood based microfluidic literature demonstrates the diversity in possible assay conditions. Therefore the limitations of the present study need to be considered in this broader context.

Conclusion

In conclusion, we demonstrate a hierarchy of elastomeric microvalve design that demonstrates that v-shaped valves display the highest degree of haemocompatibility. Significantly, this valve geometry minimises the requirements for surface

chemical modification to reduce biofouling. Taken together with previously published studies examining the impact of shear rate and shear rate gradients on platelet and blood function, this study highlights the importance of considering the overall haemodynamic profile of microfluidic components when designing blood-handling systems. We believe that the approach defined in this study is a step toward rational, biologically focused, blood handling microfluidic design, with the potential to be extended to a range of microfluidic components.

Author contribution

The manuscript was written through contributions of all authors. All authors have given approval to the final version of the manuscript. CS designed, fabricated, and ran mechanical testing of the microfluidic device and co-wrote the manuscript. RJB carried out biological experiments and co-wrote the manuscript. KK developed and ran the CFD simulations. FA developed and ran the μPIV experiments. MK developed and built the ancillary valve drivers and carried out mechanical testing. PT contributed to the design of the test manifolds. IM carried out VWF experiments and multimer analysis. IM developed the μPIV experiments and imaging system. HN contributed to biological experimental design. AM designed the microfluidic device and fabrication methods and contributed to experimental design. WSN developed the experimental design, supervised the study and wrote the manuscript.

Conflicts of interest

There are no conflicts to declare.

Acknowledgements

Notes and references

1   C. Rivet, H. Lee, A. Hirsch, S. Hamilton and H. Lu, *Chem. Eng. Sci.*, 2011, **66**, 1490–1507.
2   B. Weigl, G. Domingo, P. Labarre and J. Gerlach, *Lab Chip*, 2008, **8**, 1999–2014.
3   C. Briggs, S. Kimber and L. Green, *Br. J. Haematol.*, 2012, **158**, 679–690.
4   S. K. Vashist, P. B. Luppa, L. Y. Yeo, A. Ozcan and J. H. T. Luong, *Trends Biotechnol.*, 2015, **33**, 692–705.
5   Y. Song, Y.-Y. Huang, X. Liu, X. Zhang, M. Ferrari and L. Qin, *Trends Biotechnol.*, 2014, **32**, 132–139.
6   W. Van Oeveren, *Scientifica*, 2013, **1**, 392584.
7   R. J. Gilbert, H. Park, M. Rasponi, A. Redaelli, B. Gellman, K. A. Dasse and T. Thorsen, *ASAIO J.*, 2007, **53**, 447–455.
8   L. Tingjie, Z. Limin, L. Kar Man and Y. Jun, *J. Micromech. Microeng.*, 2010, **20**, 105024.
9   B. S. Lee, J. N. Lee, J. M. Park, J. G. Lee, S. Kim, Y. K. Cho and C. Ko, *Lab Chip*, 2009, **9**, 1548–1555.
10 C. G. Conant, M. A. Schwartz, T. Nevill and C. Ionescu-Zanetti, *J. Visualized Exp.*, 2009, 1644.
11 K. Miura and S. Shoji, in *Micro Total Analysis Systems '98: Proceedings of the uTAS '98 Workshop*, held in Banff, Canada, 13–16 October 1998, ed. D. J. Harrison and A. van den Berg, Springer Netherlands, Dordrecht, 1998, pp. 85–88, DOI: 10.1007/978-94-011-5286-0_20.
12 H. Takao, K. Miyamura, H. Ebi, M. Ashiki, K. Sawada and M. Ishida, *Sens. Actuators, A*, 2005, **119**, 468–475.
13 Y. Oimatsu, K. Kaikita, M. Ishii, T. Mitsuse, M. Ito, Y. Arima, D. Sueta, A. Takahashi, S. Iwashita, E. Yamamoto, S. Kojima, S. Hokimoto and K. Tsujita, *J. Am. Heart Assoc.*, 2017, **6**, e005263.
14 H. Takao, K. Miyamura, H. Ebi, M. Ashiki, K. Sawada and M. Ishida, *Sens. Actuators, A*, 2005, **119**, 468–475.
15 L.-C. Xu, J. W. Bauer and C. A. Siedlecki, *Colloids Surf., B*, 2014, **124**, 49–68.
16 Y. Jun Kang and S.-J. Lee, *Biomicrofluidics*, 2013, **7**, 054122.
17 Y. J. Kang, S. Y. Yoon, K. H. Lee and S. Yang, *Artif. Organs*, 2010, **34**, 944–949.
18 K. Broos, S. F. De Meyer, H. B. Feys, K. Vanhoorelbeke and H. Deckmyn, *Thromb. Res.*, 2012, **129**, 245–249.
19 W. Ouyang, W. Wei, X. Cheng, X. F. Zhang, E. B. Webb Iii and A. Oztekin, *J. Non-Newtonian Fluid Mech.*, 2015, **217**, 58–67.
20 S. W. Schneider, S. Nuschele, A. Wixforth, C. Gorzelanny, A. Alexander-Katz, R. R. Netz and M. F. Schneider, *Proc. Natl. Acad. Sci. U. S. A.*, 2007, **104**, 7899–7903.
21 C. E. Sing and A. Alexander-Katz, *Biophys. J.*, 2010, **98**, L35–L37.
22 A. L. Fogelson and K. B. Neeves, *Annu. Rev. Fluid Mech.*, 2015, **47**, 377–403.
23 S. L. Hirsh, D. R. McKenzie, N. J. Nosworthy, J. A. Denman, O. U. Sezerman and M. M. M. Bilek, *Colloids Surf., B*, 2013, **103**, 395–404.
24 M. Zhang and T. A. Horbett, *J. Biomed. Mater. Res., Part A*, 2009, **89**, 791–803.
25 L. D. Casa, D. H. Deaton and D. N. Ku, *J. Vasc. Surg.*, 2015, **61**, 1068–1080.
26 S. M. Dopheide, M. J. Maxwell and S. P. Jackson, *Blood*, 2002, **99**, 159–167.
27 D. Varga-Szabo, I. Pleines and B. Nieswandt, *Arterioscler., Thromb., Vasc. Biol.*, 2008, **28**, 403–412.
28 T. A. Springer, *Blood*, 2014, **124**, 1412–1425.
29 T. V. Colace, G. W. Tormoen, O. J. McCarty and S. L. Diamond, *Annu. Rev. Biomed. Eng.*, 2013, **15**, 283–303.
30 H.-J. Choo, T. B. Saafir, L. Mkumba, M. B. Wagner and S. M. Jobe, *Arterioscler., Thromb., Vasc. Biol.*, 2012, **32**, 2946–2955.

31 R. J. Brazilek, F. J. Tovar-Lopez, A. K. T. Wong, H. Tran, A. S. Davis, J. D. McFadyen, Z. Kaplan, S. Chunilal, S. P. Jackson, H. Nandurkar, A. Mitchell and W. S. Nesbitt, *Lab Chip*, 2017, **17**, 2595–2608.

32 W. S. Nesbitt, E. Westein, F. J. Tovar-Lopez, E. Tolouei, A. Mitchell, J. Fu, J. Carberry, A. Fouras and S. P. Jackson, *Nat. Med.*, 2009, **15**, 665–673.

33 F. J. Tovar-Lopez, G. Rosengarten, E. Westein, K. Khoshmanesh, S. P. Jackson, A. Mitchell and W. S. Nesbitt, *Lab Chip*, 2010, **10**, 291–302.

34 A. K. Au, H. Lai, B. R. Utela and A. Folch, *Micromachines*, 2011, **2**, 179–220.

35 R. Mohan, B. R. Schudel, A. V. Desai, J. D. Yearsley, C. A. Apblett and P. J. A. Kenis, *Sens. Actuators, B*, 2011, **160**, 1216–1223.

36 J. Kim, M. Kang, E. C. Jensen and R. A. Mathies, *Anal. Chem.*, 2012, **84**, 2067–2071.

37 H. Kazuo and M. Ryutaro, *J. Micromech. Microeng.*, 2000, **10**, 415.

38 C. Szydzik, B. Niego, G. Dalzell, M. Knoerzer, F. Ball, W. S. Nesbitt, R. L. Medcalf, K. Khoshmanesh and A. Mitchell, *RSC Adv.*, 2016, **6**, 87988–87994.

39 S. S. Shibeshi and W. E. Collins, *Appl. Rheol.*, 2005, **15**, 398–405.

40 W. S. Nesbitt, I. S. Harper, S. M. Schoenwaelder, Y. Yuan and S. P. Jackson, in *Platelets and Megakaryocytes: Volume 3, Additional Protocols and Perspectives*, ed. J. M. Gibbins and M. P. Mahaut-Smith, Springer New York, New York, NY, 2012, pp. 73–89, DOI: 10.1007/978-1-61779-307-3_6.

41 W. S. Nesbitt, F. J. Tovar-Lopez, E. Westein, I. S. Harper and S. P. Jackson, *Methods Mol. Biol.*, 2013, **1046**, 39–58.

42 S. Gogia and S. Neelamegham, *Biorheology*, 2015, **52**, 319–335.

43 E. Meram, B. D. Yilmaz, C. Bas, N. Atac, O. Yalcin, H. J. Meiselman and O. K. Baskurt, *Biorheology*, 2013, **50**, 165–176.

44 M. J. Maxwell, E. Westein, W. S. Nesbitt, S. Giuliano, S. M. Dopheide and S. P. Jackson, *Blood*, 2007, **109**, 566–576.

45 L. Convert, V. Chabot, P.-J. Zermatten, R. Hamel, J.-P. Cloarec, R. Lecomte, V. Aimez and P. G. Charette, *Sens. Actuators, B*, 2012, **173**, 447–454.

46 S. Mukherjee, T. G. Kang, Y. Chen and S. Kim, *Crit. Rev. Biomed. Eng.*, 2009, **37**, 517–529.

47 B. Ziaie, A. Baldi, M. Lei, Y. Gu and R. A. Siegel, *Adv. Drug Delivery Rev.*, 2004, **56**, 145–172.

48 I. Wong and C.-M. Ho, *Microfluid. Nanofluid.*, 2009, **7**, 291.

49 S. Tripathi, Y. V. B. Kumar, A. Agrawal, A. Prabhakar and S. S. Joshi, *Sci. Rep.*, 2016, **6**, 26749.

50 V. VanDelinder and A. Groisman, *Anal. Chem.*, 2007, **79**, 2023–2030.

51 A. I. Rodríguez-Villarreal, M. Arundell, M. Carmona and J. Samitier, *Lab Chip*, 2010, **10**, 211–219.

52 R. D. Jäggi, R. Sandoz and C. S. Effenhauser, *Microfluid. Nanofluid.*, 2007, **3**, 47–53.

53 A. Kummrow, J. Theisen, M. Frankowski, A. Tuchscheerer, H. Yildirim, K. Brattke, M. Schmidt and J. Neukammer, *Lab Chip*, 2009, **9**, 972–981.

54 K. Loutherback, J. D'Silva, L. Liu, A. Wu, R. H. Austin and J. C. Sturm, *AIP Adv.*, 2012, **2**, 042107.

55 W. S. Nesbitt, E. Westein, F. J. Tovar-Lopez, E. Tolouei, A. Mitchell, J. Fu, J. Carberry, A. Fouras and S. P. Jackson, *Nat. Med.*, 2009, **15**, 665–673.

56 M. Kersaudy-Kerhoas and E. Sollier, *Lab Chip*, 2013, **13**, 3323–3346.

57 C. Szydzik, K. Khoshmanesh, A. Mitchell and C. Karnutsch, *Biomicrofluidics*, 2015, **9**, 064120.

58 M. Diez-Silva, M. Dao, J. Han, C.-T. Lim and S. Suresh, *MRS Bull.*, 2010, **35**, 382–388.

59 M. C. Wesseling, L. Wagner-Britz, F. Boukhdoud, S. Asanidze, D. B. Nguyen, L. Kaestner and I. Bernhardt, *Cell. Physiol. Biochem.*, 2016, **38**, 2414–2425.

CHAPTER 5: Conclusions and Future Work

At the beginning of this thesis it was noted that while complex microfluidics were introduced several decades ago, and have been shown to enable significant outcomes in a research context, they have not yet achieved significant traction in real world end-user applications, and certainly have not seen the predicted disruptive impact analogous to introduction of the integrated circuit to the electronics industry, as anticipated in their early days. This thesis thus set out to explore the hypothesis that a key factor preventing the uptake and rapid development of complex microfluidics was the challenges associated with existing multilayer elastomer fabrication approaches. It was proposed that if a simplified approach could be developed, then this would lower the barrier to harnessing and developing this technology, and this would in turn accelerate it towards deployment in real world end-user applications. It was hoped that these steps might perhaps ultimately lead to the realisation of the full potential that complex multilayer microfluidic systems have been predicted to achieve.

To this end, this thesis investigated a new fabrication method intended to facilitate practical realisation of complex multilayer microfluidic structures. Application of this fabrication method was explored in the context of real-world problems, assessing the practicality, adaptability and scalability of the method. Finally, the method was used to fabricate complex multilayer microfluidic systems in volumes required to enable biological studies, facilitating insights into the use of common multilayer control components for handling complex biological samples, studies that would be impractical with traditional methods.

5.1 Outcomes of this work

A primary outcome of this work was a fabrication method, outlined in chapter 2, which demonstrated that fabrication of key complex multilayer microfluidic components can be greatly simplified, overcoming numerous challenges associated with traditional multilayer fabrication methods. The level of simplification offered by this fabrication method was shown to allow

69

relatively simple and reliable fabrication of these common components, significantly reducing fabrication overheads. This method was demonstrated in a proof of concept capacity to allow the fluidic manipulation and environmental control sophistication advantages that complex multilayer microfluidic structures provide, with a level of accessibility similar to that available to basic microfluidic systems.

Chapter 3 explored the practicalities of application for this technique, field testing the fabrication method in the context of real-world applications, but in the context of short-term collaborative engagements with researchers who could benefit from complex multilayer microfluidics, but who were not experts in the field. The adaptability of the fabrication method was explored, demonstrating its capacity to rapidly develop a toolbox of modular components, and adapt and refine these components and systems based on these components to create solutions to problems faced by the collaborating research teams. The collaborative projects focussed on integration of microfluidics with highly sensitive photonic biosensor platforms. In the first case study pneumatic microvalve based systems were adapted to perform assay automation and were integrated with a highly sensitive photonic biosensor platform, with the ultimate goal of creating a 'point of care' environmental detection of an antibiotic in seawater. In the second case study the new fabrication technique and toolbox of proven components was applied to enable sophisticated environmental control, adapting vapour permeable membranes and microvalve control elements to allow sophisticated environmental control of an isolated volume over an integrated plasmonic biosensor, facilitating long duration single cell analysis. Chapter 3 demonstrated that removing the fabrication bottleneck generally associated with complex multilayer microfluidic systems, enabled rapid development of practical solutions that genuinely improved the target applications at a speed that was feasible during short term and even remote collaboration. Such rapid development and iterative improvement would have been impractical with traditional multi-layer fabrication methods. Overall, chapter 3 showed that the fabrication method introduced in chapter 2 showed significant potential for rapid development of research prototypes and was highly suitable for rapidly achieving significant outcomes through collaboration with researchers outside the field of microfluidics creating clear opportunities for growth in uptake of this technology.

Having shown in chapter 3 that fabrication technique of chapter 2 was very well suited to research collaboration, chapter 4 explored application of this approach in a biomedical clinical context investigation the utility of the platform when using whole blood and the scalability of the approach to producing 100's of replicate devices needed for limited clinical trials. The capacity of this fabrication method to handle increasingly complex biological samples was assessed, moving from blood plasma to whole blood. Chapter 4 established the hemocompatibility of the fabricated devices and a selection of modular building blocks demonstrating that microfluidic control functionality without significant deleterious impact on blood at physiologically relevant flow rates. The fabrication technique could enable practical fabrication of hundreds of replicate devices, enabling biological studies using complex multilayer microfluidic devices, that would otherwise be prohibitively difficult due to the large numbers of replicate devices required to gather statistically significant data. Overall, the chapter highlighted that platforms fabricated with the technique, were well suited to handling complex biological fluids, and this was validated in the context of a comprehensive battery of blood function assays. This initial research has attracted the attention of clinical researchers and even some initial interest from a point of care device company, indicating that the barrier to real world uptake of this technology in a clinical context has certainly been lowered.

5.2 Concluding remarks and suggestions for future work

The work in this thesis operates on the assumption that challenges associated with fabrication of complex multilayer microfluidic systems are a primary bottleneck preventing widespread acceptance of the technology. The work in this thesis has demonstrated that access to complex multilayer microfluidic systems without the fabrication overheads generally associated with these systems does allow their application to areas that would otherwise be prohibitively difficult. While overcoming fabrication challenges may allow the advantages of complex multilayer microfluidic systems to be applied to otherwise unexplored applications, there are of course other caveats associated with application of complex multilayer microfluidic systems.

During this work, there was significant interest in systems that can be realised through application of the fabrication technique, a fair amount of draw was generated, with numerous research avenues necessitating careful consideration of the direction of this research. It quickly became apparent that while design and fabrication of prototype systems has a short turnaround, deployment of these systems to additional real-world applications, is somewhat limited by the availability of support equipment. Each independently controllable on-chip microvalve component in this thesis required an off-chip electronically controlled solenoid valve and substantial additional external support equipment. While the work in this thesis chose not to focus on challenges associated with external support equipment or control interface, it is possible that another significant challenge in widespread acceptance of complex multilayer microfluidic systems is this complexity of control interface and required support equipment. This is particularly relevant in the case of pneumatic on chip control components, as these systems generally require elaborate pressure regulation subsystems and off-chip solenoid valve manifolds to actuate on-chip components. Simplified interfaces and robust, cheap support equipment are a critical requisite to successful point of care translation of complex multilayer microfluidic control components. As with other researchers in this field, it was possible to reduce this burden through parallelism using one external valve to control multiple on-chip valves in unison, however truly complex systems (with 100's or even 1000's of valves) remain impractical due to the linear relationship between the on-chip complexity and the interfaces and external support equipment required.

A solution to this problem potentially exists in the direction of further integration. If it is possible to integrate some of the functionality of the external support equipment directly on-chip, it may be possible to scale on-chip complexity with a nonlinear reliance on interfaces and external systems. An initial implementation of this idea would be to move the electronically controlled solenoid valves on-chip, or to a semi integrated chip carrier component. While this would reduce the complexity of the external support equipment, the complexity of these integrated valves would again scale along with their application, and fabrication overheads would quite possibly outweigh any advantage. Another potential solution, which has attracted significant interest in the literature, would be implementation of an electronically addressed microvalve [54-56]. If it were possible to offload microvalve control interfaces to well established electronic systems, the issue

of interface would be significantly simplified, and external support equipment could be reduced to the scale of a simple microcontroller. It is possible that practical realisation of electronically addressable microvalves carries the promise of realising the predicted revolution in microfluidic system complexity, however, while promising, numerous challenges need to be overcome to enable practical realisation of electronically addressable microvalves. Such valves would require an actuation mechanism that can provide pressure differentials and scalability comparable with pneumatic or hydraulically driven microvalves, while the requirement for mechanical transducers generally introduce additional fabrication challenges and the scaling relationships for the energy required to switch valves may not favour miniaturisation.

Alternatively, simplification of required external support equipment could potentially be achieved through increasing sophistication of on-chip systems, working toward serial control interfaces. As the computer industry moved from parallel communications interfaces, toward universal serial bus communications, a similar paradigm shift in on-chip pneumatic control components would drastically increase the available sophistication for a given level of off-chip complexity.

Numerous advances have been made toward multiplexing and addressing regimes that enhance on-chip complexity while minimising required external control components. The field of microfluidic logic has demonstrated significant promise in this area, with various control components shown to duplicate the functionality of their electronic counterparts [17]. These systems have been shown to drastically reduce required control interfaces, with complex addressing schemes such as fluidic shift registers, allowing a degree of serial device interface. While these systems have achieved this outcome using various pathways, they generally share the common problem of exceedingly complex fabrication methods. This suggests a clear pathway for future research. If it is possible to fabricate these systems without their significant fabrication overheads, it may be possible to realise the full potential of complex multilayer microfluidic systems. This could make commonplace the kind of exponentially complex on-chip systems, with minimised interfaces, as was a primary factor in advancing the electronics industry.

Future work is planned to explore application of the simplified fabrication techniques outlined in this thesis, to practically realise microfluidic logic circuitry. While microfluidic logic systems are

generally fabricated with fairly complex fabrication methods, it should be possible to realise most of the required geometries with the technique, with one key exception. Reliable formation of viaduct pathways between top and bottom layer features remains a challenge with the PDMS injection moulding fabrication technique. There are various pathways that can be taken toward including reliable viaduct fabrication in the list of multilayer components that can be included in devices fabricated with this technique, and as further work beyond the scope of this thesis, I would suggest this as a vital component enabling the next step toward simplified integration of complex microfluidic logic circuitry.

References

1.	Whitesides, G.M., *The origins and the future of microfluidics.* Nature, 2006. **442**(7101): p. 368.

2.	Mark, D., et al., *Microfluidic lab-on-a-chip platforms: requirements, characteristics and applications*, in *Microfluidics Based Microsystems*. 2010, Springer. p. 305-376.

3.	Nge, P.N., C.I. Rogers, and A.T. Woolley, *Advances in microfluidic materials, functions, integration, and applications.* Chemical reviews, 2013. **113**(4): p. 2550-2583.

4.	Hitt, D.L., C.M. Zakrzwski, and M.A. Thomas, *MEMS-based satellite micropropulsion via catalyzed hydrogen peroxide decomposition.* Smart Materials and Structures, 2001. **10**(6): p. 1163.

5.	Elvira, K.S., X.C. i Solvas, and R.C. Wootton, *The past, present and potential for microfluidic reactor technology in chemical synthesis.* Nature chemistry, 2013. **5**(11): p. 905.

6.	Jokerst, J.C., J.M. Emory, and C.S. Henry, *Advances in microfluidics for environmental analysis.* Analyst, 2012. **137**(1): p. 24-34.

7.	Atalay, Y.T., et al., *Microfluidic analytical systems for food analysis.* Trends in food science & technology, 2011. **22**(7): p. 386-404.

8.	Sackmann, E.K., A.L. Fulton, and D.J. Beebe, *The present and future role of microfluidics in biomedical research.* Nature, 2014. **507**(7491): p. 181.

9.	Gravesen, P., J. Branebjerg, and O.S. Jensen, *Microfluidics-a review.* Journal of micromechanics and microengineering, 1993. **3**(4): p. 168.

10.	Ng, J.M., et al., *Components for integrated poly (dimethylsiloxane) microfluidic systems.* Electrophoresis, 2002. **23**(20): p. 3461-3473.

11.	Mosadegh, B., et al., *Next-generation integrated microfluidic circuits.* Lab on a Chip, 2011. **11**(17): p. 2813-2818.

12.	Melin, J. and S.R. Quake, *Microfluidic large-scale integration: the evolution of design rules for biological automation.* Annu. Rev. Biophys. Biomol. Struct., 2007. **36**: p. 213-231.

13.	Huh, D., G.A. Hamilton, and D.E. Ingber, *From 3D cell culture to organs-on-chips.* Trends in cell biology, 2011. **21**(12): p. 745-754.

14.	Rhee, M. and M.A. Burns, *Microfluidic pneumatic logic circuits and digital pneumatic microprocessors for integrated microfluidic systems.* Lab on a chip, 2009. **9**(21): p. 3131-3143.

15.	Weaver, J.A., et al., *Static control logic for microfluidic devices using pressure-gain valves.* Nature Physics, 2010. **6**(3): p. 218.

16.	Devaraju, N.S.G.K. and M.A. Unger, *Pressure driven digital logic in PDMS based microfluidic devices fabricated by multilayer soft lithography.* Lab on a Chip, 2012. **12**(22): p. 4809-4815.

17.   Zhang, Q., et al., *Logic digital fluidic in miniaturized functional devices: Perspective to the next generation of microfluidic lab - on - chips.* Electrophoresis, 2017. **38**(7): p. 953-976.

18.   Cai, H., et al., *Optofluidic analysis system for amplification-free, direct detection of Ebola infection.* Scientific reports, 2015. **5**: p. 14494.

19.   Kim, J., et al., *Pneumatically actuated microvalve circuits for programmable automation of chemical and biochemical analysis.* Lab on a Chip, 2016. **16**(5): p. 812-819.

20.   Schudel, B.R., et al., *Microfluidic chip for combinatorial mixing and screening of assays.* Lab on a Chip, 2009. **9**(12): p. 1676-1680.

21.   Esch, E.W., A. Bahinski, and D. Huh, *Organs-on-chips at the frontiers of drug discovery.* Nature reviews Drug discovery, 2015. **14**(4): p. 248.

22.   Thorsen, T., S.J. Maerkl, and S.R. Quake, *Microfluidic large-scale integration.* Science, 2002. **298**(5593): p. 580-584.

23.   Araci, I.E. and S.R. Quake, *Microfluidic very large scale integration (mVLSI) with integrated micromechanical valves.* Lab on a Chip, 2012. **12**(16): p. 2803-2806.

24.   Mohammed, M.I., S. Haswell, and I. Gibson, *Lab-on-a-chip or Chip-in-a-lab: Challenges of Commercialization Lost in Translation.* Procedia Technology, 2015. **20**: p. 54-59.

25.   Lee, C.-C., T.M. Snyder, and S.R. Quake, *A microfluidic oligonucleotide synthesizer.* Nucleic acids research, 2010. **38**(8): p. 2514-2521.

26.   Moraes, C., Y. Sun, and C.A. Simmons, *Solving the shrinkage-induced PDMS alignment registration issue in multilayer soft lithography.* Journal of micromechanics and microengineering, 2009. **19**(6): p. 065015.

27.   Eddings, M.A., M.A. Johnson, and B.K. Gale, *Determining the optimal PDMS–PDMS bonding technique for microfluidic devices.* Journal of Micromechanics and Microengineering, 2008. **18**(6): p. 067001.

28.   Booth, R. and H. Kim, *Characterization of a microfluidic in vitro model of the blood-brain barrier (μBBB).* Lab on a Chip, 2012. **12**(10): p. 1784-1792.

29.   Szydzik, C., et al., *Fabrication of complex PDMS microfluidic structures and embedded functional substrates by one-step injection moulding.* RSC Advances, 2016. **6**(91): p. 87988-87994.

30.   Szydzik, C., et al., *An automated optofluidic biosensor platform combining interferometric sensors and injection moulded microfluidics.* Lab on a Chip, 2017. **17**(16): p. 2793-2804.

31.   Li, X., et al., *Label - Free Optofluidic Nanobiosensor Enables Real - Time Analysis of Single - Cell Cytokine Secretion.* Small, 2018: p. 1800698.

32.   Szydzik, C., et al., *Elastomeric microvalve geometry affects haemocompatibility.* Lab on a Chip, 2018. **18**(12): p. 1778-1792.

33.   Szydzik, C., et al., *Microfluidic platform for separation and extraction of plasma from whole blood using dielectrophoresis.* Biomicrofluidics, 2015. **9**(6): p. 064120.

34. Thurgood, P., et al., *Porous PDMS structures for the storage and release of aqueous solutions into fluidic environments.* Lab on a Chip, 2017. **17**(14): p. 2517-2527.

35. Knoerzer, M., et al., *Dynamic drag force based on iterative density mapping: A new numerical tool for three - dimensional analysis of particle trajectories in a dielectrophoretic system.* Electrophoresis, 2016. **37**(4): p. 645-657.

36. Thurgood, P., et al., *A self-sufficient micro-droplet generation system using highly porous elastomeric sponges: A versatile tool for conducting cellular assays.* Sensors and Actuators B: Chemical, 2018. **274**: p. 645-653.

37. Szydzik, C., et al. *Towards an integrated optofluidic system for highly sensitive detection of antibiotics in seawater incorporating bimodal waveguide photonic biosensors and complex, active microfluidics.* in *SPIE BioPhotonics Australasia.* 2016. International Society for Optics and Photonics.

38. Kern, P., J. Janson, and C. Szydzik, *Container for the at least substantially separate storage and release of substances, in particular for storage and release in outer space.* 2016, Google Patents.

39. Kern, P., J. Janson, and C. Szydzik, *Device for performing a biochemical analysis, especially in outer space.* 2014, Google Patents.

40. Unger, M.A., et al., *Monolithic microfabricated valves and pumps by multilayer soft lithography.* Science, 2000. **288**(5463): p. 113-116.

41. Kim, J., et al., *Lifting gate polydimethylsiloxane microvalves and pumps for microfluidic control.* Analytical chemistry, 2012. **84**(4): p. 2067-2071.

42. Gelber, M.K. and R. Bhargava, *Monolithic multilayer microfluidics via sacrificial molding of 3D-printed isomalt.* Lab on a Chip, 2015. **15**(7): p. 1736-1741.

43. Au, A.K., et al., *Microvalves and micropumps for BioMEMS.* Micromachines, 2011. **2**(2): p. 179-220.

44. Mukhopadhyay, R., *When PDMS isn't the best.* 2007, ACS Publications.

45. Domansky, K., et al., *SEBS elastomers for fabrication of microfluidic devices with reduced drug absorption by injection molding and extrusion.* Microfluidics and Nanofluidics, 2017. **21**(6): p. 107.

46. Estevez, M.C., M. Alvarez, and L.M. Lechuga, *Integrated optical devices for lab - on - a - chip biosensing applications.* Laser & Photonics Reviews, 2012. **6**(4): p. 463-487.

47. Heath, J.R., A. Ribas, and P.S. Mischel, *Single-cell analysis tools for drug discovery and development.* Nature reviews Drug discovery, 2016. **15**(3): p. 204.

48. Brennan, M.D., et al., *Oxygen control with microfluidics.* Lab on a Chip, 2014. **14**(22): p. 4305-4318.

49. Li, X., et al., *Single Cell Analysis: Label - Free Optofluidic Nanobiosensor Enables Real - Time Analysis of Single - Cell Cytokine Secretion (Small 26/2018).* Small, 2018. **14**(26): p. 1870119.

77

50. Halldorsson, S., et al., *Advantages and challenges of microfluidic cell culture in polydimethylsiloxane devices.* Biosensors and Bioelectronics, 2015. **63**: p. 218-231.

51. Nahavandi, S., et al., *Microfluidic platforms for biomarker analysis.* Lab on a Chip, 2014. **14**(9): p. 1496-1514.

52. Nesbitt, W.S., et al., *A shear gradient–dependent platelet aggregation mechanism drives thrombus formation.* Nature medicine, 2009. **15**(6): p. 665.

53. Charitidis, C., et al., *Influence of accelerated aging on nanomechanical properties, creep behaviour and adhesive forces of PDMS.* Plastics, Rubber and Composites, 2012. **41**(2): p. 94-99.

54. Chang, P.J., et al., *Force measurements of a magnetic micro actuator proposed for a microvalve array.* Journal of Micromechanics and Microengineering, 2014. **24**(3): p. 034005.

55. Zhang, A.-L., et al., *A shape memory alloy microvalve switching off by surface acoustic wave.* Ferroelectrics, 2017. **506**(1): p. 1-9.

56. Richter, C., et al., *An individual addressable and latchable actuator array for microfluidic systems.* Microfluidics and Nanofluidics, 2016. **20**(9): p. 130.

Appendices

Chapter 2 Supplementary material

Fabrication of complex PDMS microfluidic structures and embedded functional substrates by one-step Injection moulding – Supplementary material

Fabrication of complex PDMS microfluidic structures and embedded functional substrates by one-step Injection moulding

C. Szydzik [a], B. Niego [b], G. Dalzell [a], M. Knoerzer [a], F. Ball [a,c], W.S. Nesbitt [a,b], R.L. Medcalf [b], K. Khoshmanesh [a], A. Mitchell [a].

a.   School of Electrical and Computer Engineering, RMIT University, Melbourne, VIC 3001, Australia
b.   Australian Centre for Blood Diseases, Monash University, Melbourne, Australia
c.   Institute for Optofluidics and Nanophotonics (IONAS), University of Applied Sciences Karlsruhe, 76133 Karlsruhe Germany.

Supplementary S1. Fabrication details

The following supplementary information outlines the process used to produce PDMS slab components using the PDMS Injection Moulding Technique. This process is similar for both photolithographically defined and 3D printed mould structures.

- Initially PDMS pre-polymer (Sylgard 184, Dow Corning USA) is mixed with the standard 1:10 ratio (curing agent: PDMS) and degassed. Following standard degassing procedure, the pre-polymer is further degassed for approximately 30 minutes under high vacuum (~ 0.2 millibar) with a vacuum pump such as those used in many plasma treatment units. This further degassing step reduces the risk of bubbles becoming trapped between the gas-impermeable mould structures. Small bubbles that may form on feature edges during PDMS injection can be absorbed into the highly degassed PDMS pre-polymer.

- In the case of functional structure integration, the structure intended for encapsulation within the PDMS slab must be placed on the bottom mould structure, and aligned as to interface with channel structures in the desired locations.

- The top mould half is placed in contact with the bottom mould half, and aligned, either manually in the case of photolithographically defined moulds, or automatically through use mechanical alignment features integrated into 3D printed mould structures.

- Mould halves are clamped in place using a mechanical clamp structure (2 pairs of aluminium bars clamped with bolts of appropriate length and fixed with wing-nuts). Sufficient pressure must be applied to ensure firm contact between mould structure and functional structure (or spacer structure in the case of valve fabrication).

- Highly degassed PDMS pre-polymer is loaded into a lubricant free syringe. This syringe is fitted to the 4 mm Luer interface hole in the top mould, and PDMS is smoothly injected to fill the mould. PDMS injection can be continued with excess PDMS flowing out of the mould structure, injection of roughly 2 times the mould volume ensures that any bubbles that are not adhered to the mould structure can flow out from between the moulds.

- Following PDMS injection, the clamped mould structure is placed in an oven at the desired curing temperature. For photolithographically defined moulds a curing temperature of 80°C is used to maximise effects of thermal contraction assisted mould release. In the case of 3D printed moulds, cure temperature must be kept below the heat distortion temperature of the material (<51°C for VisiJet® SL Clear 3DSystems Rock Hill, South Carolina).

- For photolithographically defined moulds, mould separation begins to occur spontaneously during cooling when the mould is removed from the oven. The passivated bottom mould half should be removed first, this can be achieved by gentle insertion of a soft tool such as plastic tweezers or a fingernail between the mould halves. 3D printed moulds are separated in the same manner, however this is more challenging due to the lack of a passivated surface and thermal contraction driven delamination.

- Following Release of one mould half, the PDMS slab can be cut to size and peeled from the remaining mould half, the slab can then be plasma treated and permanently bonded to sealing substrates.

Supplementary S2. Cell culture protocol

The following supplementary information outlines the cell culture protocol used to achieve a co-culture in contact configuration within microfluidic devices made using the injection moulding fabrication technique. This protocol is based on our method developed for static systems [1], adapted and modified from published protocols[2] for use in flow-based microfluidic systems. Cell types used are human brain microvascular endothelial cells (ACBRI 376, Cell-Systems Corporation) and human transformed foetal astrocytes (a cell-line termed SVG[3]). Please note: all reagents and media required for these cell cultures are specified in Niego and Medcalf, *JoVE* 2013 [1].

1. Channel cleaning protocol
This initial procedure sterilizes the channel and performs an initial bubble-free fluid priming of the channel, which can be challenging when using complex geometry.

- Perfuse 1 ml of 70 % ethanol at 300 µl/min
- Wait 10 min to sterilize
- Perfuse 1 ml sterile distilled water at 300 µl/min
- Wait 10 min to allow complete ethanol diffusion out of PDMS
- Perfuse 1 ml distilled water at 300 µl/min
- Perfuse 500 µl PBS at 300 µl/min

2. Fibronectin coating
This critical step prepares the channel surface for cell adhesion; from this point onwards fluids can be drawn backwards through the chip to minimize waste of valuable reagents, however care must be take to avoid bubble infiltration.

- Dilute fibronectin in PBS to make 100 µl at 10 µg/ml concentration approx. 50 µl or as required
- Draw minimum volume into the chip at 100-200 µl/min (accounting for tube length + channel volume + diffusion margin approx. 25 µl)
- Wait 45 min for adsorption
- Flush with equal volume to fibronectin treatment (approx. 25µl) of PBS or media at 200 µl/min

3. Endothelial cell seeding
Introduce cells suspended in culture media at concentration of 10 million per ml

- Prepare endothelial cell suspension at a concentration of 10 million cells per ml
- Draw cells into the chip in orientation which allows gravitational sedimentation of cells onto the desired face of the membrane / channel surface
  - Perfuse cell suspension at 100-200 µl/min (a minimum suspension volume needs to account for tube length + channel volume + diffusion margin)
- Clamp tubing to ensure static conditions (i.e. no movement of fluids) for optimal cell adhesion
- Place chip in incubator and allow cells to adhere in static conditions for 2-6 hours

4. Astrocyte Seeding
Astrocytes are cultured on the opposite face of the porous membrane, allowing the two cell types to form physical contact unique to this blood-brain barrier (BBB) model.

- Prepare astrocyte cell suspension at a concentration of 8 million cells per ml
- Flip the microfluidic device upside down
- Draw astrocytes into the second channel. Astrocytes will sink onto the opposite surface of the membrane (and the entire channel length)
- Perfuse astrocyte suspension at 100-200 µl/min (account for minimum volume as mentioned above)
- Clamp tubing to ensure static conditions for cell adhesion
- Place chip in incubator and initiate flow of media to endothelial channel only. Calculate flow to induce a shear rate of 1 dyn/cm^2.

6. Cell growth period
Cultivate the co-culture for 24-48 hours in low shear rates (1 dyn/cm^2; equivalent to physiological shear rates in venules). During this low shear period cells proliferate and form a confluent monolayer. When confluence is reached, the microfluidic BBB contact model is ready for experimentation.

3

Supplementary S3. Experimental verification of valve functionality

Functionality of valves fabricated using the injection moulding technique was qualitatively verified using a simple experimental setup involving merging of dye coloured water with a stream of clear water. Clear water was fed through a central micro channel using a syringe pump. Intersecting dye channels are maintained at a slight positive pressure by pressurising external fluid reservoirs, and interface to this primary channel via valve gates, which are actuated manually through compression or expansion of gas within a connected syringe [4]. Application of negative pressure lifts these valve gates, while application of slight positive pressure ensures sealing of the valve gate upon closing. Control of the valve gate position is used to modulate the fluidic resistance of the gated channel. Pressure applied to the actuation chambers of the valves is varied between ambient and a relative pressure, to actively close the valve, and between ambient and relative negative pressure to regulate flow rates of the auxiliary dye channels.

These valves are shown in operation in **supplementary Video 1**. This video shows operation of the valves to regulate flow rate of coloured dyes into primary flow of clear water, followed by application of valves in this configuration used to dose droplets with varying concentrations of dye.

4

References:

1. B. Niego and R. L. Medcalf, *JoVE (Journal of Visualized Experiments)*, 2013, e50934-e50934.
2. R. Booth and H. Kim, *Lab on a chip*, 2012, 12, 1784-1792.
3. E. O. Major, A. E. Miller, P. Mourrain, R. G. Traub, E. De Widt and J. Sever, *Proceedings of the National Academy of Sciences*, 1985, 82, 1257-1261.
4. D. Irimia and M. Toner, *Lab on a Chip*, 2006, 6, 345-352.

83

An automated optofluidic biosensor platform combining interferometric sensors and injection moulded microfluidics– Supplementary material

Supplementary Material:

An automated optofluidic biosensor platform combining interferometric sensors and injection moulded microfluidics

C. Szydzik[1], A.F. Gavela[2], S. Herranz[2], J. Roccisano[1], M. Knoerzer[1], P. Thurgood[1],
K. Khoshmanesh[1], A. Mitchell[1], L.M. Lechuga*[2]

[1] School of Engineering, RMIT University, Melbourne Australia

[2] Nanobiosensors and Bioanalytical Applications Group. Catalan Institute of Nanoscience and Nanotechnology (ICN2). CSIC, CIBER-BBN and The Barcelona Institute of Science and Technology, Campus UAB, Bellaterra, 08193 Barcelona, Spain.

* Corresponding authors:
Laura.lechuga@icn2.cat

Supplementary Material SM-1: Experimental setup

Operation of the Bimodal waveguide biosensor was conducted using an experimental setup similar to previously outlined [1]. A He-Ne laser (632.8nm, 10 mW) was end-fire coupled to the biosensor through a 40x microscope objective using TE polarization, the resultant interferometric signal was acquired with a duel segment photodiode (S5870, Hamamtsu) and data analysis was performed using LabVIEW software (National Instruments, USA). The microfluidic module was clamped to the BiMW sensor directly between a PMMA clamp and a thermal regulation stage, stabilising intrinsic signal drift due to environmental thermal influence

2

85

Supplementary Fig.S-1: On chip diaphragm pump geometry. **Fig.S-1 A** shows a dissected segment of the microfluidic module, showing the various critical components, and illustrating their relative size. A dashed line through the pump chamber shows a cut, with **Fig.S-1 B** showing a cross sectional image of this cut surface, illustrating the relative thickness of primary, membrane, and actuation chamber components of the valves used in this module.

3

86

Supplementary Fig.S-2: Raw sensor data
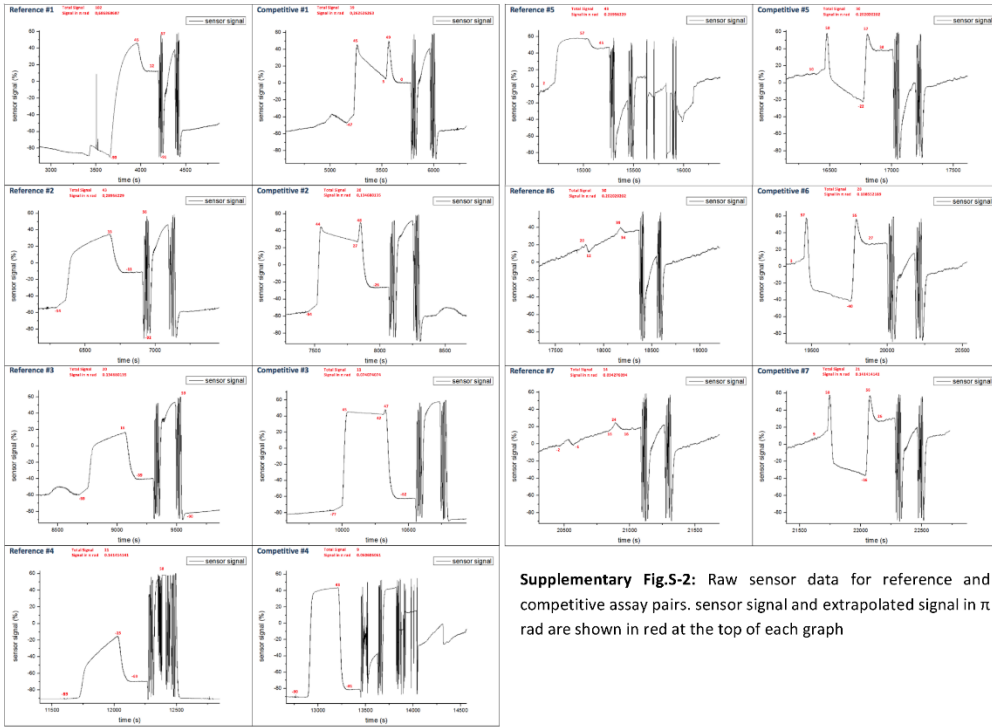
Supplementary Fig.S-2: Raw sensor data for reference and competitive assay pairs. sensor signal and extrapolated signal in π rad are shown in red at the top of each graph

4

87

REFERENCES

1.   K. E. Zinoviev, A. B. González-Guerrero, C. Domínguez and L. M. Lechuga, Journal of Lightwave Technology **29** (13), 1926-1930 (2011).

5

Label-Free Optofluidic Nanobiosensor Enables Real-Time Analysis of Single-Cell Cytokine Secretion– Supplementary material

Label-Free Optofluidic Nanobiosensor Enables Real-Time Analysis of Single-Cell Cytokine Secretion

Xiaokang Li, Maria Soler, Crispin Szydzik, Khashayar Khoshmanesh, Julien Schmidt, George Coukos, Arnan Mitchell, and Hatice Altug*

Supporting Information

Label-free optofluidic nanobiosensor enables real-time analysis of single-cell cytokine secretion

Xiaokang Li, Maria Soler, Crispin Szydzik, Khashayar Khoshmanesh, Julien Schmidt, George Coukos, Arnan Mitchell, Hatice Altug*

X. Li, Dr. M. Soler, Prof. H. Altug
Institute of Bioengineering
École Polytechnique Fédérale de Lausanne (EPFL)
CH-1015 Lausanne, Switzerland
E-mail: hatice.altug@epfl.ch

C. Szydzik, Dr. K. Khoshmanesh, Prof. A. Mitchell
School of Engineering
RMIT University
Melbourne, 3001 Australia

Dr. J. Schmidt, Prof. G. Coukos
Ludwig Institute for Cancer Research
University of Lausanne and Department of Oncology, University of Lausanne
CH-1007 Lausanne, Switzerland

1. Supplementary Methods

1.1. Chemicals and reagents

PEGylated alkanethiol compounds $HS-C_6EG_4OH$ (TH 001-m6.n4-0.2), and $HS-C_{11}EG_4OCH_2COOH$ (TH 003-m11.n4-0.2) were purchased from Prochimia Surfaces (Poland). Crosslinking reagents N-(3-dimethylaminopropyl)-N′-ethylcarbodiimide hydrochloride (EDC), sulfo-N-hydroxysulfosuccinimide (sulfo-NHS) as well as poly-L-lysine solution and streptavidin were purchased from Sigma-Aldrich (Switzerland). Phosphate saline buffer (PBS), RPMI 1640 medium, penicillin/streptomycin, fetal bovine serum (FBS), and eBioscience™ Cell Stimulation Cocktail for the EL4 cell culture were purchased from Thermo Fisher Scientific (Switzerland). Biotinylated IL-2 antibodies and standard proteins were purchased from MABTECH (Sweden). All the other chemicals were purchased from the EPFL chem shop unless otherwise indicated.

1.2. Cell culture

EL4 cells were cultivated in RPMI 1640 medium supplemented with 10% fetal bovine serum, 100 units mL^{-1} penicillin and 100 µg mL^{-1} streptomycin at 37 °C in a humidified 5% CO_2 incubator. The cells were subcultured routinely and counted based on a general protocol. Before cell seeding in the primary microfluidic channel, the cells were harvested by gentle washing off the culture flask and centrifuged at 1000 rpm for 5 min. The cell density was adjusted to 3×10^4 cells mL^{-1}, and the suspension was subsequently injected into the primary channel by actuating the pneumatic valves. Once the injection was finished, the pneumatic control was dismissed and the cells were enclosed in the isolated valve-gated microchamber. Finally, we achieved 4-5 cells in the isolated valve-gated region, with each cell separated as a single entity for the measurement. The seeded microfluidic assembly was incubated for at least 20 min at 37°C before the measurement.

1.3. Evaluation of water evaporation through thin PDMS membrane

Our system can be considered as three distinct PDMS membranes. These include the bulk PDMS which can be considered as a thick membrane, the pneumatic valve actuation membranes which are considered as a dry membrane (ambient humidity) and the regulation channel which can be considered as the wet membrane, as schematically shown in Figure S3. Therefore, the total vapor loss can be expressed as below:

$$\dot{V}_{vapor\ total} = \dot{V}_{PDMS} + \dot{V}_{dry\ membrane} + \dot{V}_{wet\ membrane}$$

$$(1)$$

The evaporation rate across each of these membranes can be described as below[1]:

$$\dot{V}_{vapor} = \lambda_{water-PDMS} \left(P_{saturation} - P_{vapor}\right)\frac{A_{membrane}}{t_{membrane}} \qquad (2)$$

Where, $\lambda_{water-PDMS}$ is the permeability of water vapour through PDMS which is reported as 2.7×10^{-13} $m^3(STP).m/s.$ $m^2.Pa.$[2] $P_{saturation}$ and P_{vapor} are the vapor saturation pressure, and

2

the vapor pressure, respectively. $A_{membrane}$ **and** $t_{membrane}$ are the surface area and thickness of the PDMS membrane, respectively, which vary for the three components of our system. Since P_{vapor} depends on the relative humidity (RH) of the surroundings, it can further be described as:[3]

$$P_{vapor} = \varphi \, P_{saturation} \tag{3}$$

Meanwhile, $P_{saturation}$ depends on the ambient temperature,[3] and varies as below for temperatures ranging from 20 to 70 °C:

$$P_{saturation} = 0.1348 \, T_{amb}^3 - 6.6754 \, T_{amb}^2 + 274.28 \, T_{amb} - 1570.7 \tag{4}$$

Once combining the above equations, the volume evaporation rate of water vapor through PDMS membranes can be calculated as below:

$$\tag{5}$$

3

2. Supplementary Figures

UV Radiation

Photomask

Ion beam etching

Photoresist
Au
Ti
SiO$_2$

Photoresist
Au
Ti
SiO$_2$

Au
Ti
SiO$_2$

I. Deep-UV lithography   II. Dry etching   III. Resist removal
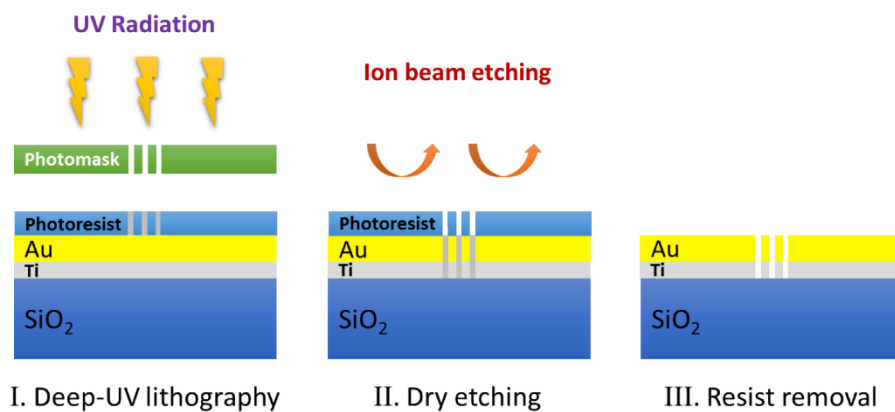
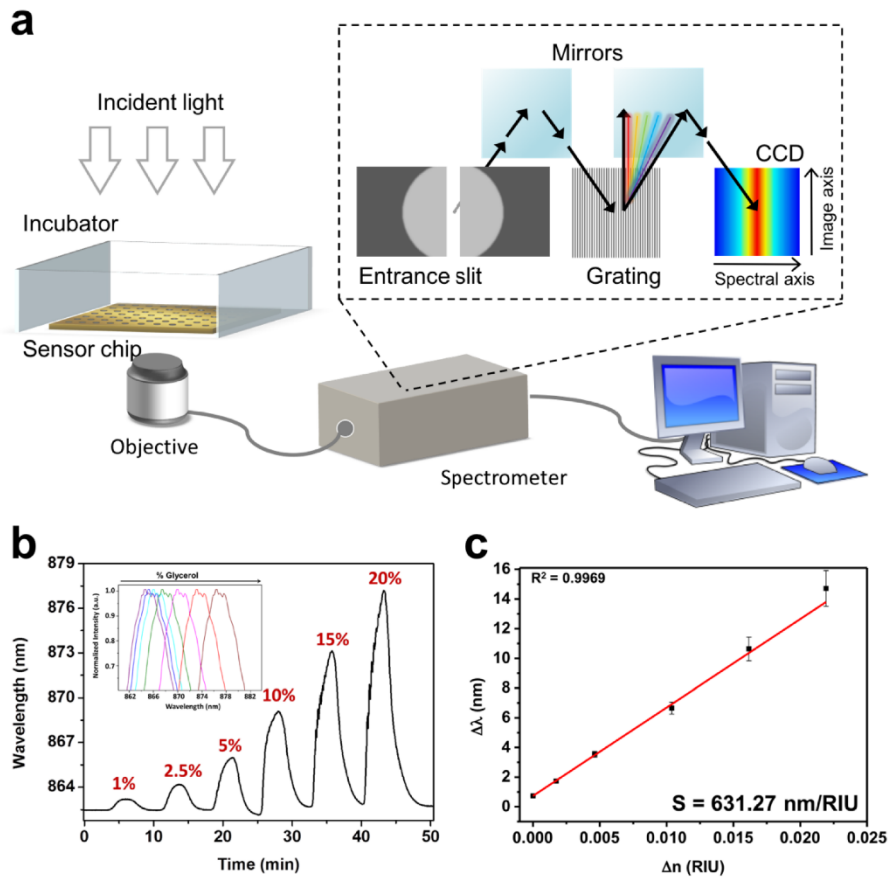**Fig. S1. The schematic wafer-scale fabrication procedure for plasmonic nanohole arrays**.

4

93

Fig. S2. Optical setup configuration and bulk sensitivity characterization for the plasmonic NHA biosensor. (a) Schematics of the optical configuration of the measurement setup. (b) Real-time sensorgram of bulk refractive index changes (i.e., different concentrations of glycerol), with the inset graph highlighting the spectral shifts of the resonance peak. (c) Bulk sensitivity calibration of the plasmonic NHA chips, where the sensitivity (S) is determined by the slope of the linear regression equation.
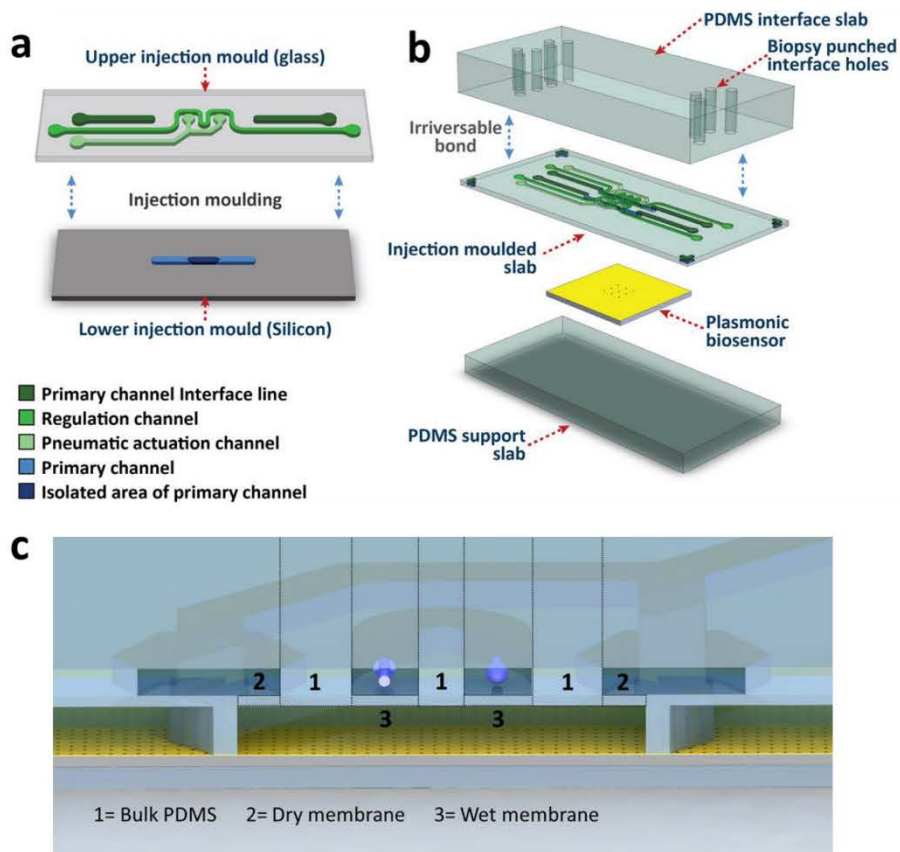
5

Fig. S3. Fabrication and illustration of the multifunctional microfluidics system. (**A**) The pair of complementary molds for the injection molding process. (**B**) Assembly of the PDMS microfluidic slabs with the nanohole array chip as the optofluidic biosensor. (**C**) Schematic cross-sectional view of the microfluidic device, where numbers label the different membrane areas of the device.
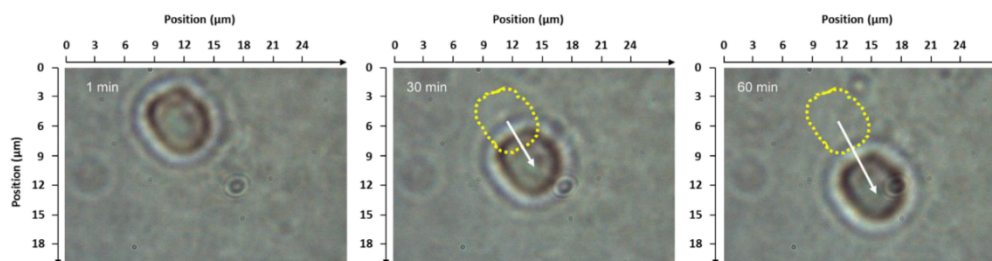
6

Fig. S4. Time-lapse images of cell movements. The movement of an individual EL4 cell during the first 60 min of one measurement for IL-2 secretion analysis. The overall movement distance is within 10 μm, which is less than the size of cell spot ROI.

References
[1] S. C. George, S. Thomas, Prog. Polym. Sci. 2001, 26, 985.
[2] W. L. Robb, Ann. N. Y. Acad. Sci. 1968, 146, 119.
[3] C. Borgnakke, R. E. Sonntag, Fundamentals of Thermodynamics, Wiley, 2013.

Chapter 4 Supplementary material

**Elastomeric microvalve geometry effects hemocompatibility - Supplementary material**
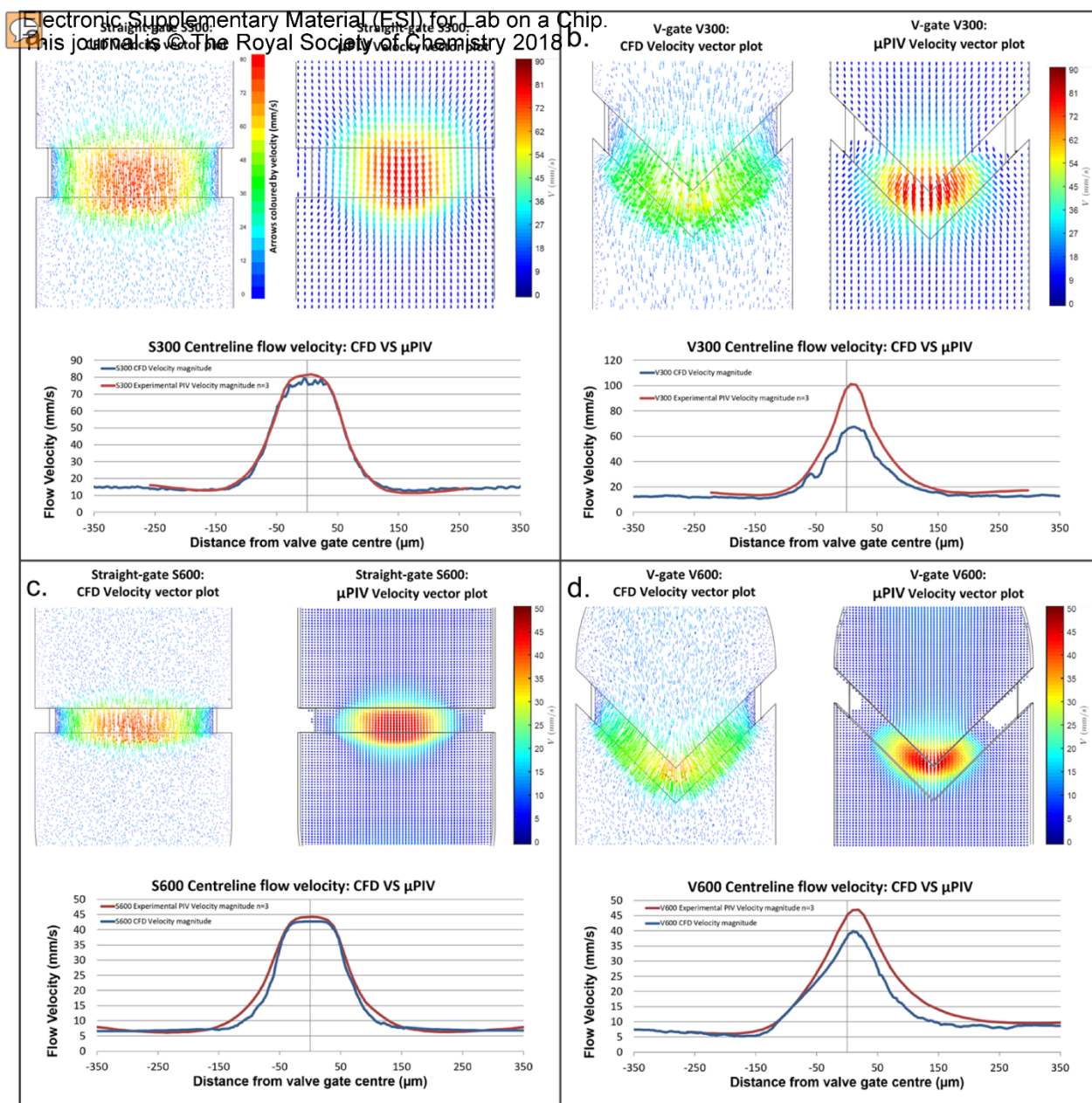
Supp fig 1 a. Direct comparison between velocity fields derived through computational fluid dynamic simulations (CFD), and corresponding experimental micro particle image velocimetry (µPIV) results, shown for 300µm straight **(a)** and v-shaped **(b)** valve gates and 600µm straight **(c)** and v-shaped **(d)**. This data is shown as velocity vectors with arrows scaled in size and coloured by magnitude, as well as centreline velocity plots superimposing longitudinal velocity along the centreline of the channel for both CFD and µPIV data. All data presented is representative of valves open to a height of 40µm at the centre of the valve gate, at Q=24 µl/min, with data shown for a central plane taken at 20µm, halfway between the valve gate and channel floor. All CFD results shown in this figure are simulated for water, in order to match µPIV conditions. CFD data is shown to match well to experimental results, with slight discrepancies most likely due to variances in individual valve actuation heights, potentially due to differing levels of delamination at the valve gate at low actuation pressures. Note the significant lateral component to fluid passing under V-shaped gates in b and d, as opposed to the relatively straight flow in a and c.
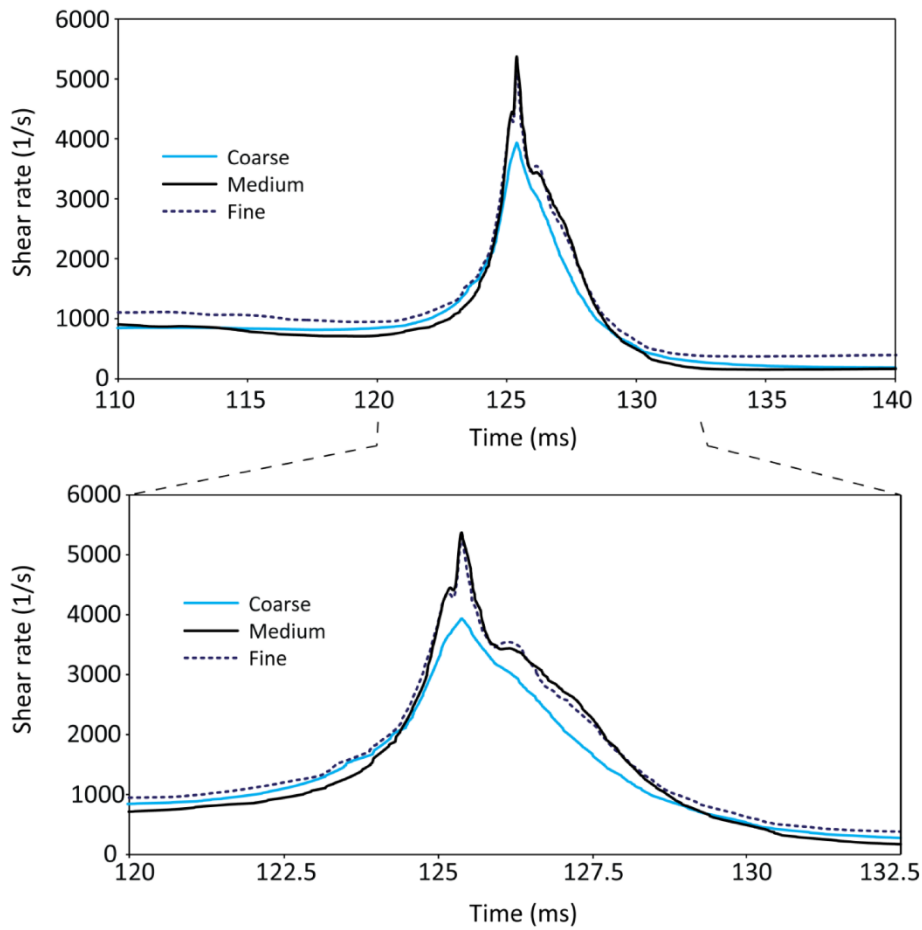
Supp fig 2. Grid convergence analysis of V-shaped gate, shear rate *v* time for a particle released 3 μm from the upstream of the V-300 gate and travelling along the middle of the gate. Simulations were conducted using three mesh densities, which are referred to as 'coarse', 'medium' and 'fine'. These mesh densities correspond to 90×15, 150×25, and 200×35 elements across the gate, respectively. A maximum shear rate of 3960 1/s was obtained using the 'coarse' mesh. Using the 'medium' mesh, the maximum shear rate increased to 5294 1/s. Applying the 'fine' mesh, the maximum shear rate only reduced to 5278 1/s with similar profiles observed before and after the gate, indicating grid convergence. Similar trends were obtained for the S300, S600 and V600 gates.
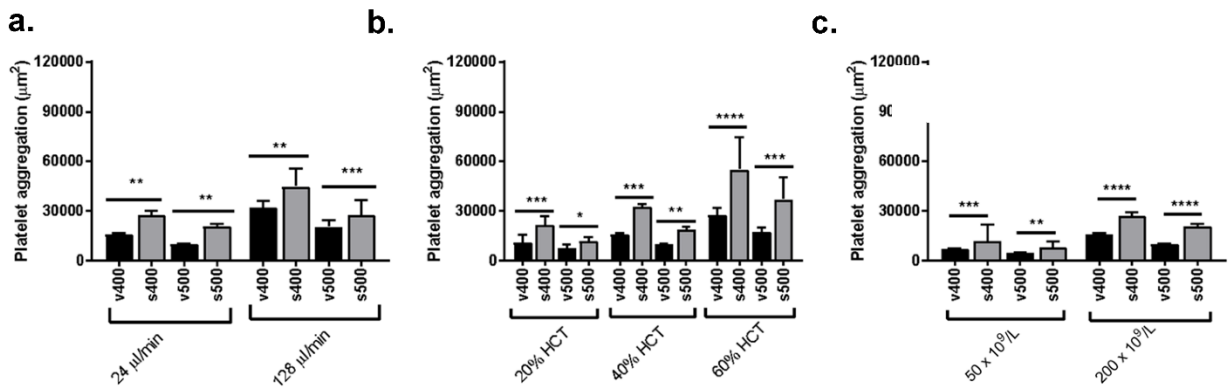
Supp fig 3 a. Platelet aggregation at straight versus v-gates at Q = 24 µl/min and 128 µl/min. **b.** Platelet aggregation at straight versus v-gates (Q = 24 µl/min) as a function of hematocrit. **c.** Platelet aggregation at straight versus v-gates (Q = 24 µl/min) as a function of platelet count. All data shows n=3 independent experiments normalized to valve surface area (µm²). Error bars standard deviation. Black horizontal bars indicate comparative valve shapes and sizes (e.g. V300 and S300) for which a significance significant difference was tested for using a paired t-tests. * P ≤ 0.05, ** P ≤ 0.01, *** P ≤ 0.001, **** P ≤ 0.0001. * P ≤ 0.05, ** P ≤ 0.01, *** P ≤ 0.001, **** P ≤ 0.0001.
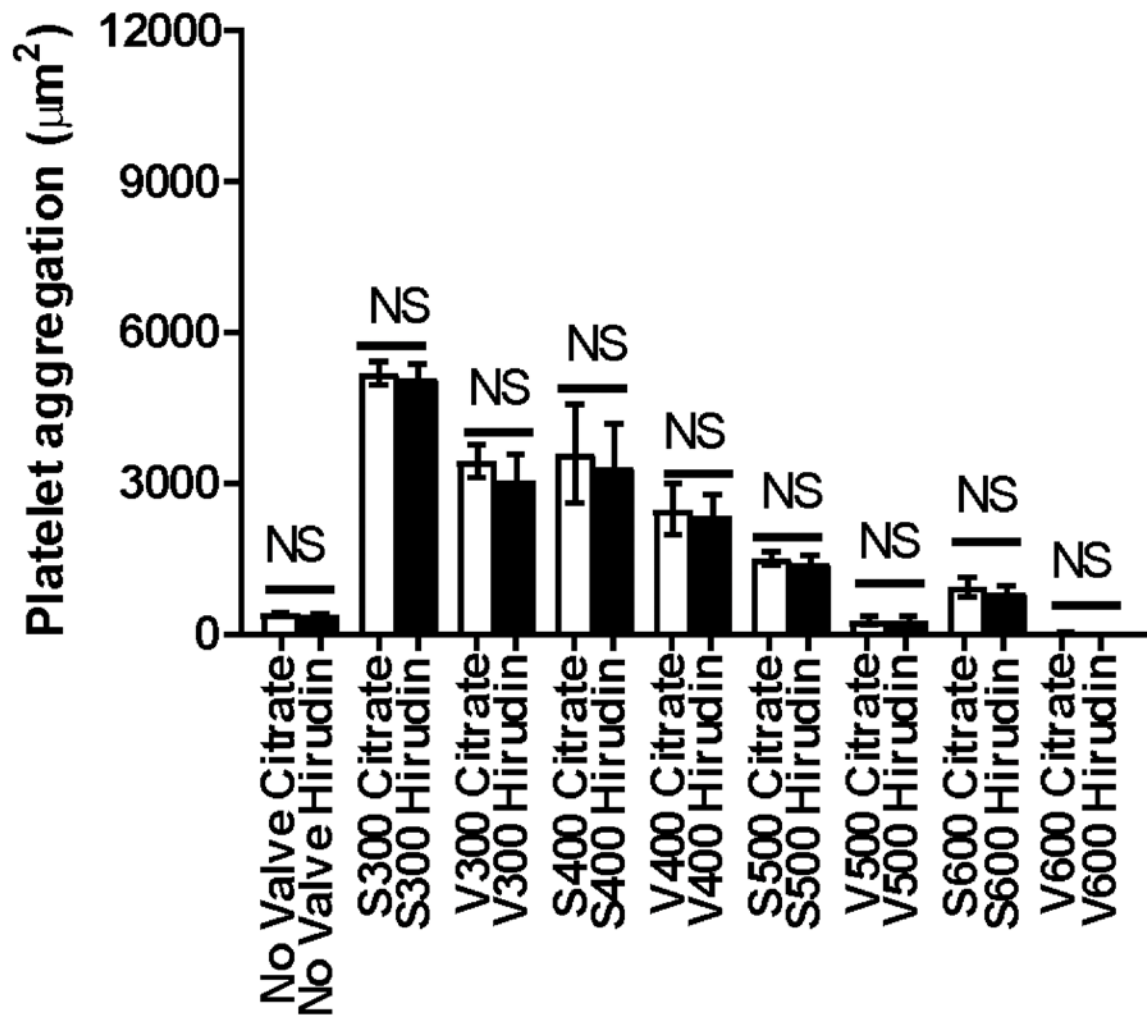
Supp fig 4 Comparison of aggregate sizes with blood collection into Hirudin (0.02% w/v) and Citrate (2% w/v) anticoagulants. Platelet aggregation was measured at Q = 24 µl/min and all valves were fully actuated. Data shows n=3 independent experiments normalized to valve surface area (μm^2). Error bars indicate standard deviation. Black horizontal bars indicate comparative valve shapes and sizes (e.g. V300 and S300) for which a significance significant difference was tested for using a paired t-tests. NS = no statistically significant difference, * P ≤ 0.05, ** P ≤ 0.01, *** P ≤ 0.001, **** P ≤ 0.0001.
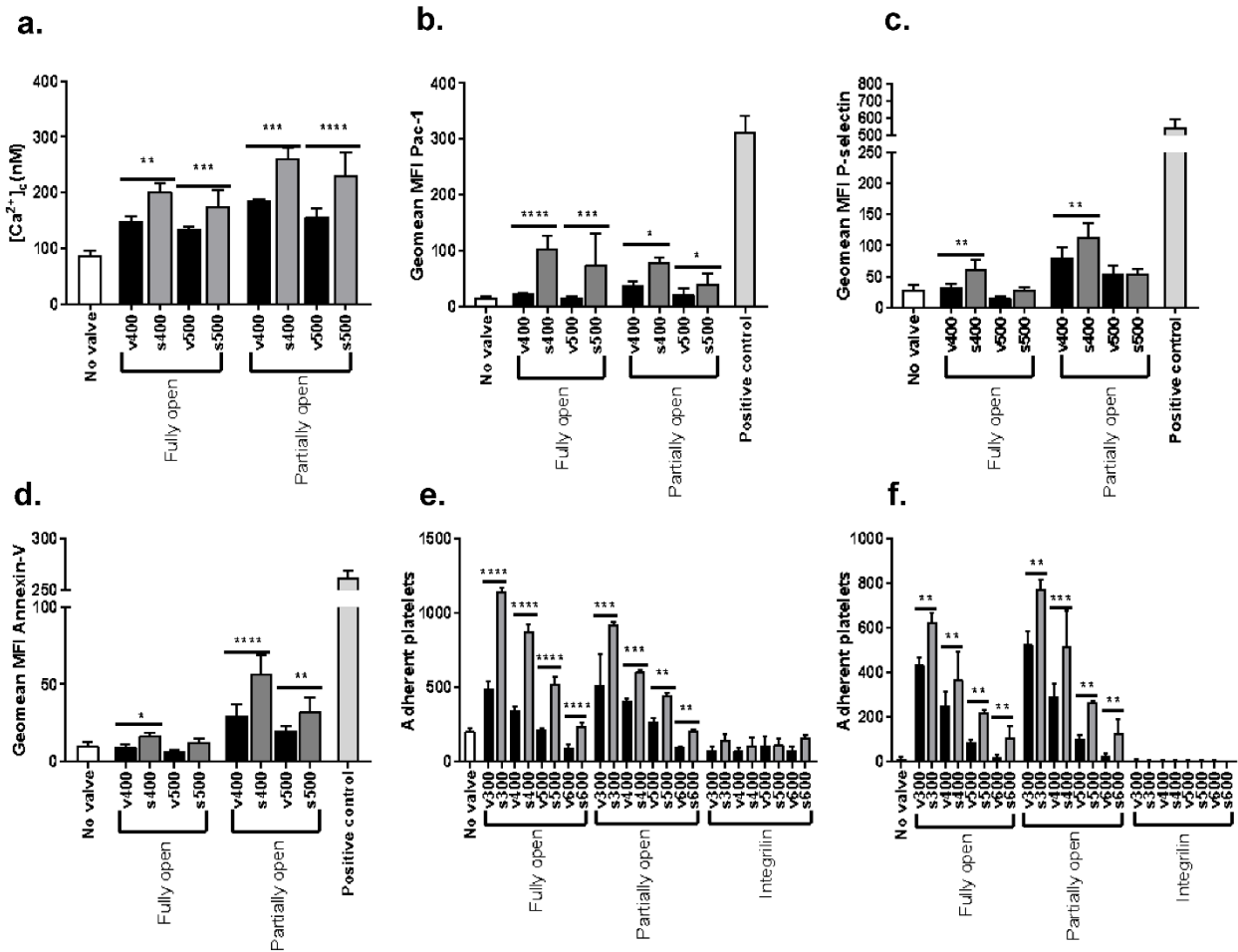
Supp fig 5 a. Maximal platelet cytosolic calcium flux $[Ca^{2+}]_c$ (nM) under perfusion at Q = 24 μl/min in the fully open and partially open (40 μm) states. (n=3 independent experiments). **b.** Fluorescence Activated Cell Sorting (FACS) analysis showing Mean Fluorescence Intensity (MFI) GeoMean distribution of FIT-C PAC-1 antibody binding (integrin $\alpha_{IIb}\beta_3$ activation) to platelets in human whole blood following perfusion through S400, S500, V400 and V500 gates (Q = 24 μl/min) in the fully open and partially open (40 μm) states. **c.** FACS analysis showing MFI GeoMean distribution of expression of P-selectin antibody binding to platelets in human whole blood following perfusion through S400, S500, V400 and V500 gates (Q = 24 μl/min) in the fully open and partially open (40 μm) states. **d.** FACS analysis showing MFI GeoMean distribution of FITC- Annexin-V binding to platelets in human whole blood following perfusion through S400, S500, V400 and V500 gates (Q = 24 μl/min) in the fully open and partially open (40 μm) states. **e.** Total number of adherent (captured) platelets in a vWF-coated (10 μg/ml) microchannel 1,000 μm post valve passage at t=130 seconds following perfusion at a straight channel shear rate of $1,800.s^{-1}$. **f.** Total number of adherent (captured) platelets in a fibrinogen-coated (13 μg/ml) microchannel 1,000 μm post valve passage at t=130 seconds following perfusion at a straight channel shear rate of $300.s^{-1}$. All data indicates n=3 independent experiments normalized to valve surface area. Error bars indicate standard deviation. Black horizontal bars indicate comparative valve shapes and sizes (e.g. V300 and S300) for which a significance significant difference was tested for using a paired t-tests. * P ≤ 0.05, ** P ≤ 0.01, *** P ≤ 0.001, **** P ≤ 0.0001. * P ≤ 0.05, ** P ≤ 0.01, *** P ≤ 0.001, **** P ≤ 0.0001.
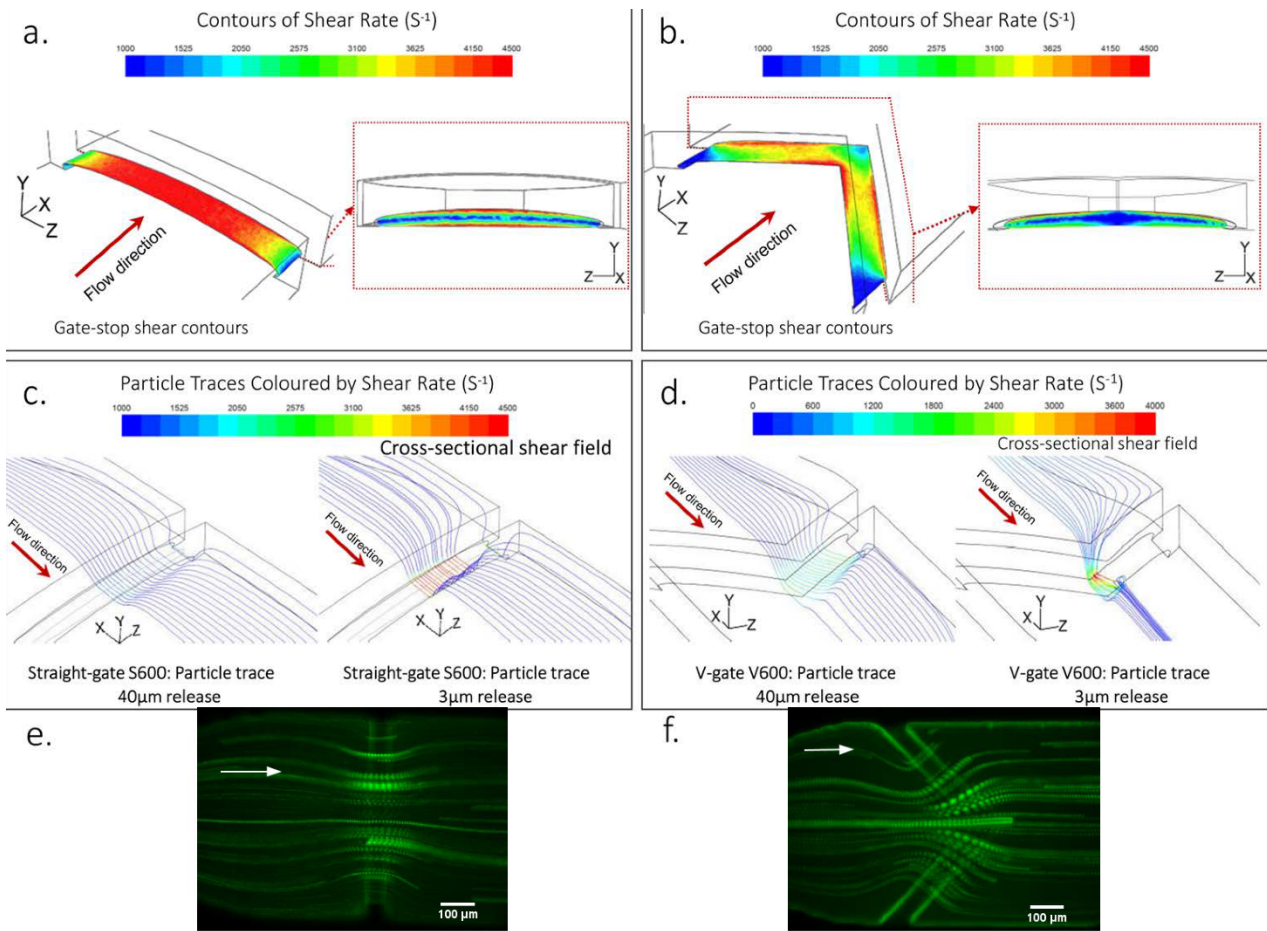
Supp fig 6. a. 3-dimensional shear contour profiles of S600 gate geometry at Q=24 ml/min and opening height of 40mm. Note the peaks in shear rate at the upstream and downstream edges of the straight gate and the overall elevation in shear rate across the straight gate surface. b. 3-dimensional shear contour profiles of V600 gate geometry at Q=24 ml/min and opening height of 40mm. Note the initial peak in shear rate at the midline upstream face of the gate surface and overall reduced shear rates. Note the generation of a low shear rate pocket that extends across the microchannel cross-section. c. Particle shear rate streamlines for fifteen 2mm particles released 40mm and 3mm from the microchannel ceiling for the straight gate case. Note the parallel particle trajectories across the gate surface. d. Particle shear rate streamlines for fifteen 2mm particles released 40mm and 3mm from the microchannel ceiling for the v-gate case. Note the streamline "funneling" for particles released at 3mm towards the valve gate midline. Note the loss of funneling at 40mm from the microchannel ceiling and divergent particle trajectories across the v-gate surface. e. Superimposed imaged of particle streamline flows taken from 16 seconds of flow in partially open S600 valves f. Superimposed imaged of particle streamline flows taken from 16 seconds of flow in partially open V600 valves.

Straight geometry

V-Gate geometry
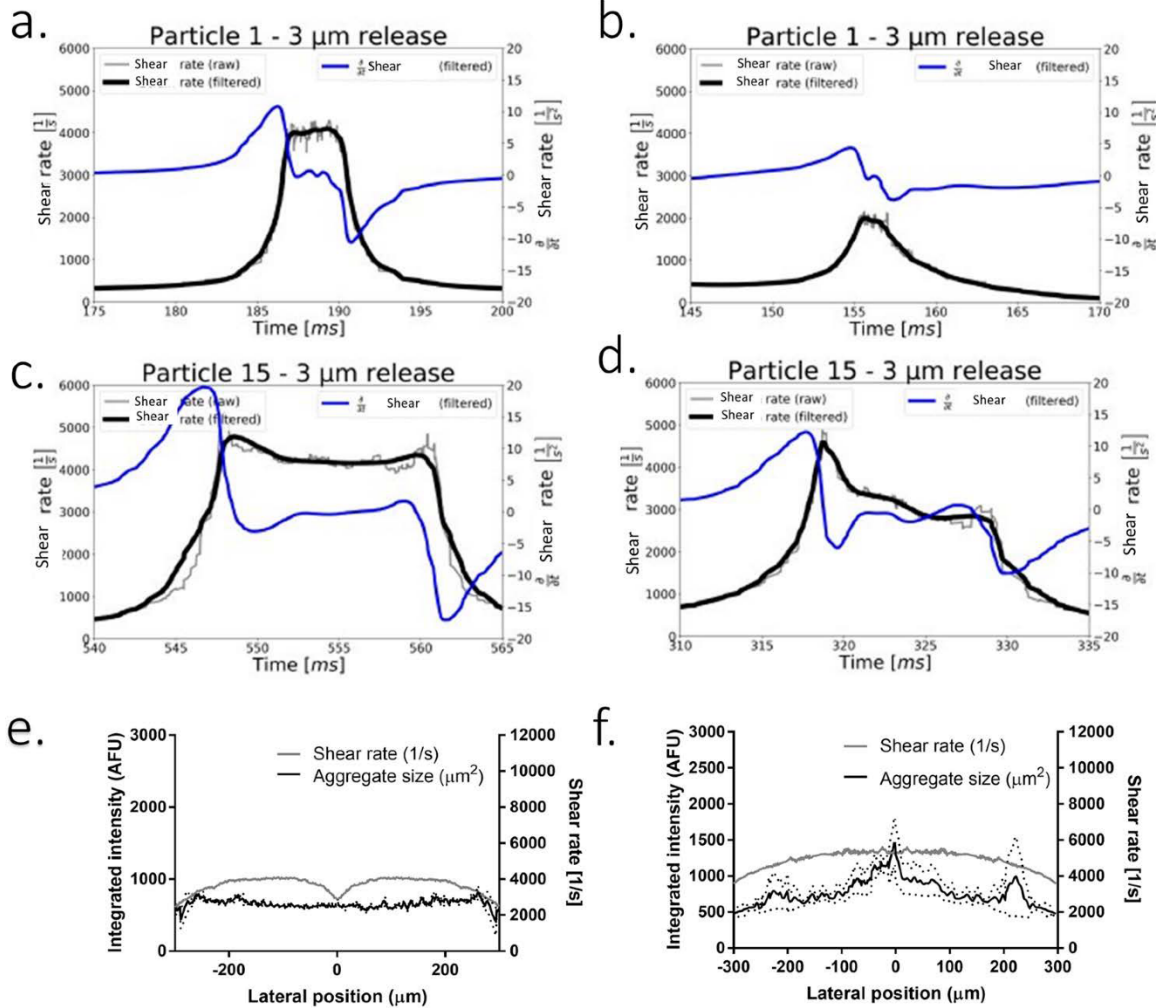
Supp fig 7 a-d. Particle shear rate (s⁻¹) v time (black line) and shear rate gradient (s⁻¹/s) (blue line) plots for particles released 3µm from the microchannel ceiling. Particle 1, released at the channel midlines is shown in the straight geometry (a) and v-gate (b), while particle 15, released at the lateral margin, close to the channel sidewall, is shown for the straight geometry in (c) and the v-gate in (d). Note the symmetric shear rate and shear rate gradient profiles for the straight case versus the asymmetric distribution and the overall reduction in peak shear rate for the v-gate. Particle 15 in both cases displayed extended shear profiles due to sidewall effects and the overall upward deformation of the valves in the open state. e-f. Points of maximal platelet aggregation and shear across the V600 partially open (40 µm) (e) and S600 partially open (f) as a function of distance from the valve midpoint. All data shows n=3 independent experiments. Error bars indicate standard deviation.

Valve Dimensions: V-600 Example case
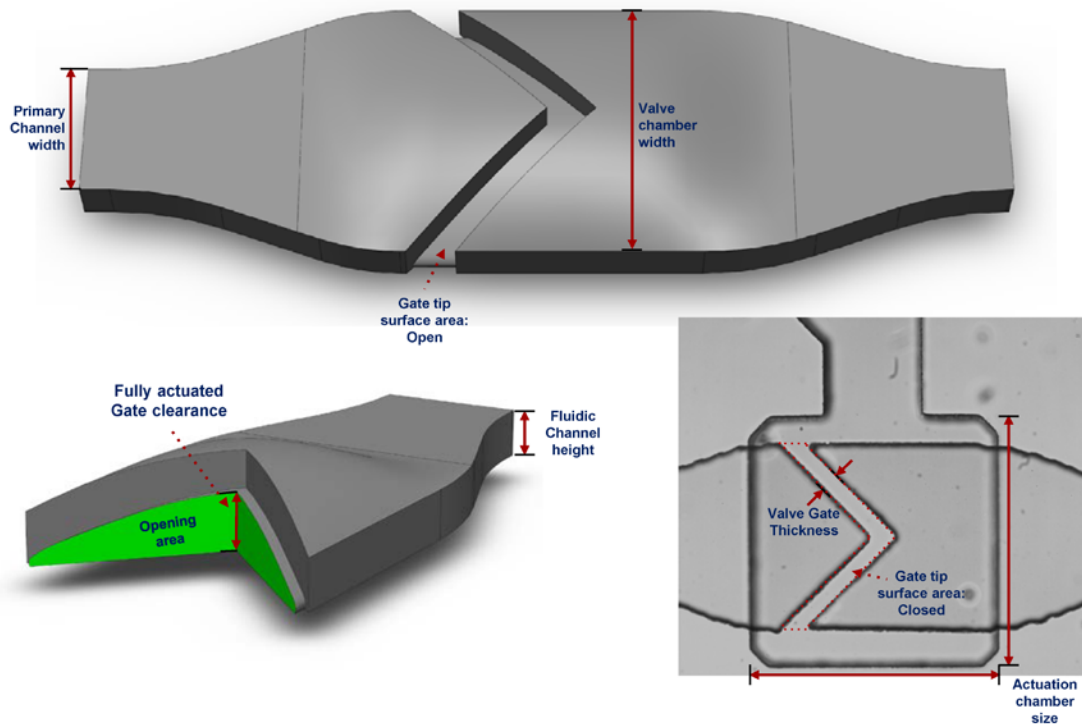
Valve name	Valve gate geometry	Fluidic Channel height	Primary Channel width	Valve chamber width	Actuation chamber size	Actuation chamber Depth	Actuation membrane thickness	Valve Gate Thickness	Fully actuated Gate clearance	Opening area	Gate tip surface area: Closed	Gate tip surface area: Open
S 300	Straight	100 µm	300 µm	300 µm	500 X 500 µm	150 µm	30-50 µm	50 µm	44 µm	0.01184 mm^2	0.0135 mm^2	0.01599 mm^2
S 400	Straight	100 µm	300 µm	400 µm	600 X 600 µm	150 µm	30-50 µm	75 µm	73 µm	0.01932 mm^2	0.02877 mm^2	0.03207 mm^2
S 500	Straight	100 µm	300 µm	500 µm	700 X 700 µm	150 µm	30-50 µm	75 µm	107 µm	0.0363 mm^2	0.03609 mm^2	0.04228 mm^2
S 600	Straight	100 µm	300 µm	600 µm	800 X 800 µm	150 µm	30-50 µm	75 µm	124 µm	0.05171 mm^2	0.04288 mm^2	0.05006 mm^2
V 300	V - Gate	100 µm	300 µm	300 µm	500 X 500 µm	150 µm	30-50 µm	50 µm	52 µm	0.01398 mm^2	0.01856 mm^2	0.02183 mm^2
V 400	V - Gate	100 µm	300 µm	400 µm	600 X 600 µm	150 µm	30-50 µm	75 µm	86 µm	0.02496 mm^2	0.0485 mm^2	0.05539 mm^2
V 500	V - Gate	100 µm	300 µm	500 µm	700 X 700 µm	150 µm	30-50 µm	75 µm	118 µm	0.04072 mm^2	0.04871 mm^2	0.05508 mm^2
V 600	V - Gate	100 µm	300 µm	600 µm	800 X 800 µm	150 µm	30-50 µm	75 µm	133 µm	0.0642 mm^2	0.06013 mm^2	0.06775 mm^2

Supp table 1 Valve dimensions

Dimensions of valve geometries used in this study. Valve name is the name each valve type is referred to throughout the manuscript, valve gate geometry classifies the two types of valve investigated. Fluidic channel height is the height of the fluidic channels, while primary width is the width of the primary channel leading to the individual gates. Valve chamber width refers to the width of the expanded channel area at the valve gate, or length of the valve, while actuation chamber size defines the size of the pneumatic actuation chamber situated above each valve, and actuation chamber depth is the depth of this chamber. Actuation membrane thickness is the thickness of the PDMS membrane separating the valve channel roof and actuation chamber, gate thickness is the thickness of the gate itself. Fully actuated gate clearance refers to the opening height at the centre of the valve gate under minimum pressure, or fully open conditions, while opening area is the cross sectional area of the gate when fully open. Gate tip surface area when closed refers to the area of the valve gate in contact with the channel floor in the closed configuration, while gate tip surface area open refers to the area of the valve gate tip when fully expanded in the open configuration

Coefficients

Model		Unstandardized Coefficients		Standardized Coefficients	t	Sig.
		B	Std. Error	Beta		
1	(Constant)	-22596.135	3484.757		-6.484	.000
	V_shaped_valve	28136.695	2530.866	.750	11.117	.000
	Straight_valve	39075.299	2530.866	1.041	15.439	.000
	Valve_size	-8202.348	542.401	-.563	-15.122	.000
	HCT	449.107	60.642	.229	7.406	.000
	Plt_count	11903.215	1855.466	.202	6.415	.000
	Flow_rate	13763.773	1855.466	.234	7.418	.000
	Open_state	31936.131	1961.298	.515	16.283	.000

a. Dependent Variable: Aggregate_size

Supp table 2 Multifactorial analysis

A multiple regression was run to predict aggregate size from valve geometry, size, patient Hct, platelet count, flow rate and open state. These variables statistically significantly predicted aggregate size, $F_{(7, 236)} = 116.218$, $p < 0.0005$, $R^2 = 0.780$. All six variables added statistically significantly to the prediction, $p < 0.0005$. The unstandardised coefficients demonstrate effect size.

Supplementary Materials & Methods

Micro particle image velocimetry (μPIV)

Micro-PIV was used to Verify and Support CFD models. Velocity field was assessed at measurement planes located halfway between the bottom surface of the channel and the tip of the valve stop. An inverted TI-U Eclipse Nikon microscope equipped with an air-immersion CFI S Plan Fluor ELWD 20× objective lens was coupled with a high-speed camera (2277 Hz at 2000 × 2000 pixels, 12 bits, PCO.dimax HS4) to record the particle images. One micron diameter red fluorescent polystyrene aqueous beads (ThermoFisher Scientific) were used to seed the flow. Polysorbate 20 (Tween 20) was added to flow to avoid particle-wall adhesion to and to prevent particle agglomeration. Illumination was provided by a 532 nm Nd:YAG double-pulsed laser (EverGreen - BigSky Laser Series) able to double-pulse at 15 Hz. A syringe pump (Harvard PHD ULTRA) and a gas-tight glass syringe (1000 μL, Hamilton) were used to deliver fluid into the microchannel via a silicon tube.

Measurements were taken at flow rates of 24 μL/hr in all channels with V-type and Straight-type valves at two different valve positions (fully opened and 40 μm open). In each set of measurements, 4000 images were captured. The common background noise in micro-PIV recordings were removed by subtracting the background image (acquired by averaging 100 images) from each recording. In micro- PIV usually low seeding density is used to reduce the background noise due to the out-of-focus particles, thereby reducing the signal to-noise ratio in correlation maps. Two averaging method ("Average Image Method" and "Average Velocity Methods") were employed to enhance the signal-to-noise. In the first method 20 images were overlaid to increase the number of particle per interrogation window (Average Image Method). Then a multigrid algorithm combined with window deformation algorithm with adaptive central difference interrogation (CDI) offsetting was implemented. Using a Fast Fourier Transform based cross-correlation algorithm, the local displacements correspond to each interrogation window (32×32) were acquired. The depth of correlation and the spatial resolution of the micro-PIV measurement were 7, 8 and 9 μm, respectively. The valid vectors of each realisation were identified using a median test and were then averaged over all realisation window (Average Velocity Method).

Assessment of platelet streamline flow

To image platelet streamlines across microvalve gate surfaces isolated platelet suspensions (200x10⁹/L) in platelet washing buffer (4.3 mM K_2HPO_4, 4.3 mM Na_2HPO_4, 24.3 mM NaH_2PO_4, 113 mM NaCl, 5.5 mMD-glucose, and 10 mM theophylline, pH 6.5) + Integrillin (20mg/mL) were labelled with the lipophilic membrane dye DiOC6 (1μg/mL) (Molecular Probes) and 0.02U/mL apyrase (to eliminate released ADP during blood collection) for 10 min at 37°C and subsequently perfused through the device at constant flow rate of 24 μL/min. Fluorescent platelet streamlines were acquired on an inverted Nikon TiU microscope (Nikon Plan Fluor 20x/0.50 objective) using an Andor Zyla sCMOS camera at 10msec exposure time, 15fps for 60sec. Time-lapse tiff imaging stacks were processed to remove background fluorescence and filtered using a median filter (2x2 kernel). Tiff stacks were subsequently processed via average z-projection to create average heat map distributions of platelet trajectories using a 16-color LUT.